Government of **Western Australia**
Department of **Mines and Petroleum**

**RECORD 2010/5**

# THE GLENBURGH OROGENY AS A RECORD OF PALEOPROTEROZOIC CONTINENT – CONTINENT COLLISION

**by SP Johnson, S Sheppard, B Rasmussen, MTD Wingate, CL Kirkland, JR Muhling, IR Fletcher, and E Belousova**

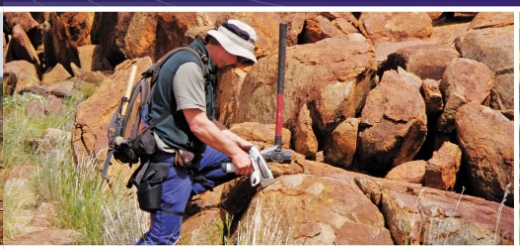

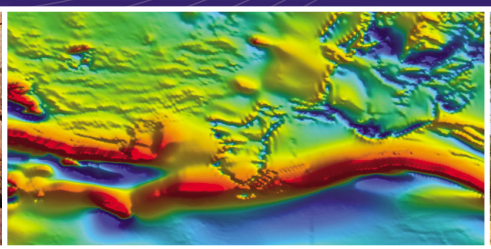

**Geological Survey of Western Australia**

Government of Western Australia
Department of Mines and Petroleum

Record 2010/5

# THE GLENBURGH OROGENY AS A RECORD OF PALEOPROTEROZOIC CONTINENT–CONTINENT COLLISION

by
SP Johnson, S Sheppard, B Rasmussen[1], MTD Wingate, CL Kirkland, JR Muhling[2], IR Fletcher[1], and E Belousova[3]

[1] Department of Applied Geology, Curtin University of Technology, GPO Box U1987, Perth, Western Australia 6845
[2] Centre for Microscopy, Characterisation and Analysis M010, The University of Western Australia, 35 Stirling Highway, Crawley, 6009, Western Australia
[3] Centre for Geochemical Evolution and Metallogeny of Continents (GEMOC), Department of Earth and Planetary Sciences, Macquarie University, Sydney, New South Wales, 2109

Geological Survey of Western Australia

**REFERENCE**
**The recommended reference for this publication is:**
Johnson, SP, Sheppard, S, Rasmussen, B, Wingate, MTD, Kirkland, CL, Muhling, JR, Fletcher, IR and Belousova, E 2010, The Glenburgh Orogeny as a record of Paleoproterozoic continent–continent collision: Geological Survey of Western Australia, Record 2010/5, 54p.

**National Library of Australia Card Number and ISBN 978-1-74168-276-2**

**Grid references in this publication refer to the Geocentric Datum of Australia 1994 (GDA94). Locations mentioned in the text are referenced using Map Grid Australia (MGA) coordinates, Zone 50. All locations are quoted to at least the nearest 100 m.**

**U–Pb measurements were conducted using the SHRIMP II ion microprobes at the John de Laeter Centre of Mass Spectrometry at Curtin University of Technology in Perth, Australia.**

John de Laeter Centre of Mass Spectrometry

**Geochemical analyses discussed in this publication are funded in part by the Western Australian State government Exploration Incentive Scheme (EIS).**

ROYALTIES FOR REGIONS
EXPLORATION INCENTIVE SCHEME

**Published 2010 by Geological Survey of Western Australia**
**This Record is published in digital format (PDF), as part of a digital dataset on CD, and is available online at www.dmp.wa.gov.au/GSWApublications. Laser-printed copies can be ordered from the Information Centre for the cost of printing and binding.**

**Further details of geological publications and maps produced by the Geological Survey of Western Australia are available from:**
Information Centre
Department of Mines and Petroleum
100 Plain Street
EAST PERTH, WESTERN AUSTRALIA 6004
Telephone: +61 8 9222 3459  Facsimile: +61 8 9222 3444
**www.dmp.wa.gov.au/GSWApublications**

# Contents



# Appendices

# Figures



# Tables

# The Glenburgh Orogeny as a record of Paleoproterozoic continent–continent collision

by
**SP Johnson, S Sheppard, B Rasmussen[1], MTD Wingate, CL Kirkland, JR Muhling[2], IR Fletcher[1], and E Belousova[3]**

## Abstract

The Gascoyne Province lies at the western end of the Capricorn Orogen, and includes a range of Paleoproterozoic gneisses and metasedimentary basins, known as the Glenburgh Terrane, that are exotic to both the Yilgarn and Pilbara Cratons. Here we present sensitive high-resolution ion microprobe (SHRIMP) U–Pb ages for a variety of detrital zircons and metamorphic zircon and monazite from several of these pre-collisional siliciclastic basins that were deformed and metamorphosed at high metamorphic grade during the Glenburgh Orogeny, when the Yilgarn Craton collided with a previously assembled Pilbara Craton – Glenburgh Terrane. The precursors to the Moogie Metamorphics were deposited sometime between 2240 and 2125 Ma in either a foreland basin to the Ophthalmian Orogeny, or a retro-arc that formed during the collision of the Glenburgh Terrane with the Pilbara Craton. The Quartpot Pelite of the Camel Hills Metamorphics was deposited between 2000 Ma and 1985 Ma as a fore-arc deposit to the Dalgaringa continental margin arc. The Petter Calc-silicate of the Camel Hills Metamorphics was deposited sometime between 2610 and 1965 Ma as part of the Yilgarn Craton passive margin. Metamorphic zircon and monazite ages indicate that continental collision and high-grade metamorphism during the Glenburgh Orogeny ($D_{2g}$) took place between 1965 Ma and 1950 Ma.

**KEYWORDS:** continental collision, Glenburgh Orogeny, Lu–Hf isotopes, monazite dating, zircon dating

## Introduction

The Capricorn Orogen lies between the Yilgarn and Pilbara Cratons, and records both the collision of these cratons to form the West Australian Craton, and the numerous intracratonic reworking events that affected the region from the Paleoproterozoic through to the latest Neoproterozoic (Fig. 1; Tyler and Thorne, 1990; Cawood and Tyler, 2004; Johnson et al., 2009). The orogen contains numerous basins filled with low-grade metasedimentary rocks and some mafic metavolcanic rocks, as well as the deformed craton margins, and the Gascoyne Province[†]. The Glenburgh Terrane, which forms the province basement, comprises 2660–2430 Ma granitic gneisses, middle Paleoproterozoic metasedimentary rocks, and a c. 2000 Ma arc-related granitic supersuite. The Glenburgh Terrane is exotic to both the Yilgarn and Pilbara Cratons and records nearly all of the deformation and metamorphism associated with the collision between the cratons. Following the collisional event, the Glenburgh Terrane and both craton margins were intruded by at least two middle to late Paleoproterozoic granitic supersuites. These medium- to high-grade rocks, along with variably deformed lower grade rocks of the latest Paleoproterozoic Pooranoo Metamorphics (including the Mount James Subgroup), are collectively termed the Gascoyne Province (Fig. 1), and were subsequently overlain by basins ranging in age from early Mesoproterozoic to Phanerozoic.

Early models for regional evolution emphasized vertical movements of the crust rather than plate tectonic processes (e.g. Daniels, 1975; Gee, 1979; Williams, 1986); however, these ideas were replaced in the late 1980s and 1990s by tectonic models invoking subduction and collision between the Pilbara and Yilgarn Cratons during the 1820–1770 Ma Capricon Orogeny (Muhling, 1988; Tyler and Thorne,

[1] Department of Applied Geology, Curtin University of Technology, GPO Box U1987, Perth, Western Australia, 6845
[2] Centre for Microscopy, Characterisation and Analysis M010, The University of Western Australia, 35 Stirling Highway, Crawley, Western Australia, 6009
[3] Centre for Geochemical Evolution and Metallogeny of Continents (GEMOC), Department of Earth and Planetary Sciences, Macquarie University, Sydney, New South Wales, 2109
[†] Use of the term 'Gascoyne Complex' is discontinued because 'complex' is a lithostratigraphic term, and the term 'Gascoyne Province' is reinstated. The following definition of a 'province' is taken from GSWA Memoir 2: 'An area of the earth's crust in which the rocks have some geological character, or combination of characters, in common; these are usually either age, metamorphic grade, structural style or type of mineralization' (Trendall, 1975, p. 30)

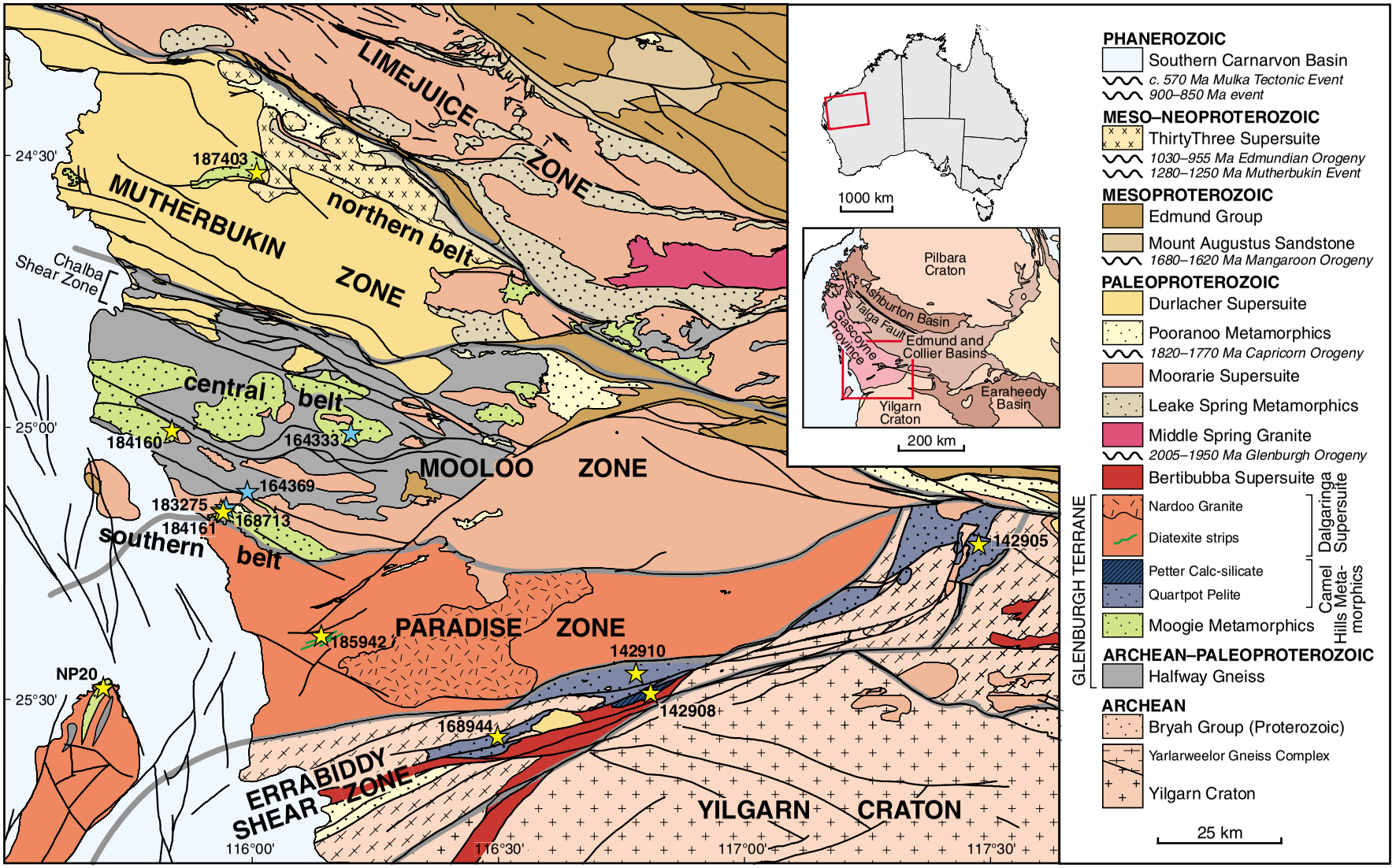


**Figure 1.** Simpli ed geological map of the southern Gascoyne Province, showing division of the region into various structural–metamorphic zones (after Sheppard et al., in prep. b). Location of dated samples are shown by yellow stars (zircon) and blue stars (monazite), and accompanied by their GSWA sample numbers.

1990). A program of regional mapping, geochemistry, and U–Pb secondary ion mass spectrometry (SIMS) geochronology — specifically sensitive high-resolution ion microprobe (SHRIMP; Geological Survey of Western Australia, 2008) — in the southern Gascoyne Province led to a greater understanding of the regional tectonics (Occhipinti et al., 2001; Occhipinti et al., 2004; Sheppard et al., 2004). These authors identified a 2005–1970 Ma suite of intermediate to felsic plutonic rocks (the Dalgaringa Supersuite) with Andean-type subduction zone geochemical and isotopic characteristics. This supersuite is thought to have developed along the southern margin of the Glenburgh Terrane prior to its collision with the passive margin of the northern Yilgarn Craton, along the Errabiddy Shear Zone, during the Glenburgh Orogeny (c. 1950 Ma). However, even after this research it remained unclear as to whether the Glenburgh Terrane was a continental fragment or part of a larger Pilbara Craton at c. 1950 Ma.

Subsequent regional mapping and geochronology by the Geological Survey of Western Australia (GSWA), as well as work by other organizations, suggests that the Glenburgh Terrane accreted to the Pilbara Craton at c. 2200 Ma (Occhipinti et al., 2004). A recent magnetotelluric (MT) survey across the western Capricorn Orogen indicated that the Glenburgh Terrane forms basement to the whole Gascoyne Province, and identified a suture between the Glenburgh Terrane and Pilbara Craton that coincides roughly with the Talga Fault (Fig. 1 inset; Selway, 2008; Selway et al., 2009). This suture is covered by the upper Wyloo Group (including the Ashburton Formation), which has a depositional age of c. 1830 Ma (Sircombe, 2003), indicating that the collision and suturing of the two cratonic entities must be older than this date. The only known tectonothermal event along the southern Pilbara Craton of appropriate age is the 2215–2145 Ma Ophthalmian Orogeny (Rasmussen et al., 2005); Blake and Barley (1992) attributed the cause of deformation during this orogeny to the collision of an unknown 'southern continent' along the southern margin of the Pilbara Craton. Therefore, following Occhipinti et al. (2004), we suggest that the Ophthalmian Orogeny marks the accretion of the Glenburgh Terrane to the Pilbara Craton.

In this revised history, the Capricorn Orogeny and several subsequent low- to medium-grade tectonothermal events spanning the interval 1820–570 Ma reflect intracontinental reworking (Johnson et al., 2009; Sheppard et al., in prep. a). These events involved the retrogression of peak metamorphic assemblages and structural overprinting of collision-related structures, and extensively modified the architecture of both the Glenburgh Terrane–Pilbara Craton and Glenburgh Terrane–Yilgarn Craton collision zones.

Although the tectonic framework for the Glenburgh Terrane and the timing of its c. 1950 Ma collision with the Yilgarn Craton is reasonably well constrained (Occhipinti et al., 2004), much of this work is based on the ages of apparently syn- or post-tectonic granites, and the regional-scale distribution of pre- or syn-collisional sedimentary basins, rather than by direct dating methods (e.g. U–Pb dating of metamorphic zircon or monazite). Furthermore, no U–Pb geochronology, either of detrital zircons, or of metamorphic zircon or monazite, was available for the Moogie Metamorphics, the package of siliciclastic metasedimentary rocks that forms a significant part of the Glenburgh Terrane. In this record we constrain key aspects of the timing of the Glenburgh Orogeny, and ultimately date the final assembly of the West Australian Craton using U–Pb dating (SIMS SHRIMP analysis) of metamorphic zircon and monazite from pre-collisional siliciclastic packages deformed and metamorphosed during the collision. Information is also presented on the ages of their detrital zircon components, and, in combination with hafnium isotopic data obtained from some of these detrital zircons by laser ablation inductively coupled plasma mass spectrometry (LA-ICP-MS), the aim is to provide constraints on the depositional ages, provenance, and tectonic settings of these siliciclastic packages.

Much of the U–Pb zircon geochronology presented here forms part of GSWA's extensive and freely available geochronological dataset (Geological Survey of Western Australia, 2009). However, some of these data cannot be considered robust as they were collected at a time when imaging the internal structures of zircon using scanning electron microscope (SEM) cathodoluminescence (CL) and back-scattered electron (BSE) was not routine. We have imaged the dated zircons via CL and re-interpreted the ages based on the location of analysis sites in relation to the internal zircon structures (e.g. Corfu et al., 2003). These results are complemented by data from more recent SHRIMP U–Pb studies, which include concurrent CL imaging of detrital and metamorphic zircon and in situ analyses of metamorphic monazite.

# Regional geology

Within the Capricorn Orogen, the oldest crust external to the Yilgarn and Pilbara Cratons is the Archean to Paleoproterozoic Glenburgh Terrane, which appears to underlie much or all of the Gascoyne Province based on the results of a recent MT survey (Selway, 2008; Selway et al., 2009). The Glenburgh Terrane consists of heterogeneously deformed granitic gneisses (the Halfway Gneiss) with igneous crystallization ages of 2660–2430 Ma (Sheppard et al., 2008a). Locally, much younger (c. 2005 Ma) leucocratic igneous material is interleaved with, and forms an integral part of, the gneiss (Occhipinti and Sheppard, 2001), indicating that at least some of the gneissic fabrics in the terrane formed during the Glenburgh Orogeny. The Halfway Gneiss is mainly in tectonic contact with, but locally unconformably overlain by, the Moogie Metamorphics, which comprises retrogressed pelitic diatexites and schists, psammitic schists with minor calc-silicate gneiss, dolomitic marble, and amphibolite. This metasedimentary package appears to have been deposited sometime after c. 2300 Ma (Sheppard et al., 2008a) but before the Halfway Gneiss and Moogie Metamorphics were intruded at 2005–1970 Ma by voluminous plutonic rocks of the Dalgaringa Supersuite (Sheppard et al., 2004; Occhipinti et al., 2004). The Dalgaringa Supersuite has Andean-type continental-margin-arc geochemical and isotopic signatures, and has been interpreted as forming above a north-dipping subduction zone (Sheppard et al., 2004; Occhipinti et al., 2004). Based on the ages of cross-cutting igneous intrusions, it appears that the older

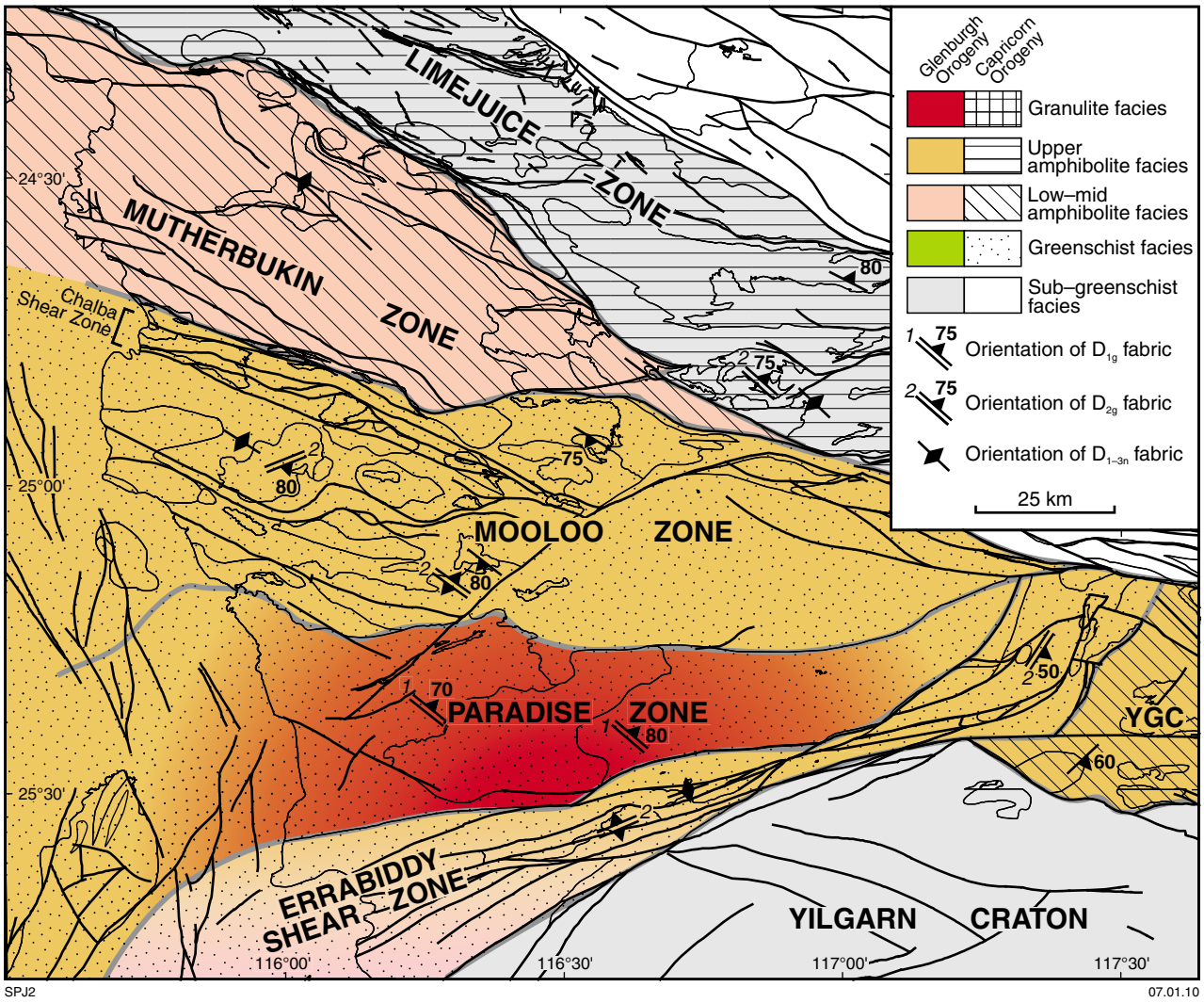


**Figure 2. Simpli ed map of the southern Gascoyne Province showing the grades of metamorphism during the Glenburgh and Capricorn orogenies. Gradient Ils for the Glenburgh Orogeny have been used where the metamorphic grade changes across (either parallel to, or normal to, structural grain) a structural–metamorphic zone. YGC = Yarlarweelor Gneiss Complex**

parts of the Dalgaringa Supersuite were metamorphosed and deformed by c. 1990 Ma, intruded by the mesocratic and leucocratic tonalite of the Nardoo Granite at c. 1975 Ma, and subsequently heterogeneously deformed and metamorphosed at c. 1950 Ma (Fig. 2; Occhipinti and Sheppard, 2001; Occhipinti et al., 2004).

The contact between the Glenburgh Terrane and the Pilbara Craton is buried by extensive Paleoproterozoic metasedimentary rocks of the upper Wyloo Group, and Mesoproterozoic sedimentary rocks of the Edmund and Collier Basins. The aforementioned MT survey showed a sharp electrical contrast between the Pilbara Craton and Glenburgh Terrane roughly coincident with the Talga Fault (Selway et al., 2009), a major structure that intermittently controlled the deposition of the Edmund Group (Martin and Thorne, 2004; Martin et al., 2008). The Glenburgh Terrane is interpreted to have collided, or at least amalgamated, with the Pilbara Craton during the 2215–2145 Ma Ophthalmian Orogeny (Occhipinti et al., 2004), with a combined Pilbara Craton – Glenburgh Terrane subsequently colliding with the Yilgarn Craton at c. 1950 Ma.

The contact between the Yilgarn Craton and Glenburgh Terrane is marked by the Errabiddy Shear Zone, which includes imbricate slices of both tectonic units. The northern part of the Yilgarn Craton comprises mainly early Archean (>3.3 Ga) gneisses (Narryer Terrane) that were intruded by widespread sheets of granite between 2750 Ma and 2620 Ma (see Occhipinti et al., 2001 for a summary). Locally, the Narryer Terrane was strongly reworked during the 1820–1770 Ma Capricorn Orogeny, and was intruded by numerous granites of the contemporaneous Moorarie Supersuite to form the Yarlarweelor Gneiss Complex (Figs 1 and 2; Occhipinti et al., 1998; Sheppard et al., 2003). Parts of the Narryer Terrane and Yarlarweelor Gneiss Complex are interleaved with rocks of the Glenburgh Terrane along the Errabiddy Shear Zone (Fig. 1).

The Errabiddy Shear Zone (Fig. 1) contains isolated, fault-bounded calc-silicate gneiss, pelitic schists, and gneisses of the Camel Hills Metamorphics (Fig. 1), which do not outcrop anywhere else in the Capricorn Orogen. These siliciclastic rocks are divided into the Petter Calc-silicate, which consists of calc-silicate schist and gneiss, and the Quartpot Pelite, which consists of retrogressed pelitic schist, pelitic gneiss, and pelitic diatexite (Sheppard and Occhipinti, 2000). Protoliths of the Petter Calc-silicate appear to have been deposited sometime after c. 2610 Ma and were derived from a Yilgarn Craton-like source, whereas the Quartpot Pelite was deposited sometime shortly before the Glenburgh Orogeny from a currently unexposed Paleoproterozoic terrane (Sheppard and Occhipinti, 2000). All lithologies within the Errabiddy Shear Zone were deformed and metamorphosed at medium to high grade during the Glenburgh Orogeny (Fig. 2; Sheppard and Occhipinti, 2000).

The northern margin of the Yilgarn Craton, the Yarlarweelor Gneiss Complex, Errabiddy Shear Zone, and Glenburgh Terrane were all intruded by granitic rocks of the 1965–1945 Ma Bertibubba Supersuite (Occhipinti et al., 2004). The supersuite includes plutons of tectonically foliated, variably porphyritic, biotite-bearing, and leucocratic metamonzogranite, and undeformed dykes of coarse-grained leucocratic tonalite and granodiorite (Sheppard and Occhipinti, 2000; Occhipinti and Sheppard, 2001). Deformed granites from the Bertibubba Supersuite have igneous crystallization ages of 1965–1955 Ma (GSWA 142909* and GSWA 142850), whereas one of the undeformed dykes has an igneous crystallization age of 1945 ± 14 Ma (GSWA 142929; Sheppard and Occhipinti, 2000), indicating that deformation had ceased prior to intrusion of the dykes at c. 1945 Ma. Older deformed granites have whole-rock Sm–Nd isotopic compositions intermediate between those for the northern Yilgarn Craton and the Dalgaringa Supersuite, suggesting derivation from melting of a mixed source comprising Dalgaringa Supersuite with minor amounts of Archean Narryer Terrane (Sheppard et al., 2004). The isotopic composition of the older deformed granites, and distribution of the Bertibubba Supersuite from the northern Yilgarn Craton through to the Glenburgh Terrane, indicates that juxtaposition and collision occurred prior to c. 1945 Ma and that the older, deformed parts of the Bertibubba Supersuite, apparently formed during the Glenburgh Orogeny, may represent a suite of syntectonic intrusions.

Following the Glenburgh Orogeny, the Gascoyne Province underwent numerous low- to medium-grade tectonothermal intracontinental reworking events, some of which were accompanied by the intrusion of voluminous granitic batholiths. Based on the temporal and geographic distribution of these events, the Gascoyne Province has been subdivided into several discrete structural–metamorphic zones (Fig. 1; Sheppard et al., 2008a; Sheppard et al., in prep. b). The main reworking events were the 1820–1770 Capricorn Orogeny (Fig. 2) and associated Moorarie Supersuite intrusions (Sheppard et al., in prep a); the 1680–1620 Ma Mangaroon Orogeny and associated Durlacher Supersuite intrusions (Sheppard et al., 2005); the medium-grade 1280–1250 Ma Mutherbukin Tectonic Event (Johnson et al., 2009); the 1030–955 Ma Edmundian Orogeny (Sheppard et al., 2007); a low-grade 900–850 Ma event (Johnson et al., 2009); and the c. 570 Ma Mulka Tectonic Event (Sheppard et al., 2008a).

# Metasedimentary packages

Supracrustal siliciclastic rocks deposited prior to the Glenburgh Orogeny are widely distributed throughout the southwestern Capricorn Orogen (Fig. 1). The Moogie Metamorphics outcrop as discrete packages, mainly within the Glenburgh Terrane's central Mooloo Zone, but also occur as small pods and strips interfolded and intercalated with the Halfway Gneiss in the Paradise Zone, and as thin, discrete tectonic slices interfolded with surrounding gneisses in the Chalba Shear Zone (Fig. 1). Rare, discontinuous high-grade strips of pelitic diatexite, tentatively correlated with the Moogie Metamorphics, occur within gneisses of the Dalgaringa Supersuite in the Paradise Zone; one aim of this paper is to test this correlation. The Camel Hills Metamorphics are present only in the southern part of the orogen as a string of small pods and strips outcropping within the Errabiddy Shear Zone over a strike length of more than 100 km. All contacts with surrounding rocks are tectonic and no original sedimentary structures are preserved.

## Moogie Metamorphics

The Moogie Metamorphics is dominated by a package of psammitic schists (the Mumba Psammite) that includes discontinuous layers of pelitic schist and quartzite, and discrete packages of pelite and quartzite. These units are intercalated with minor unnamed calc-silicate gneiss and marble, amphibolite, and actinolite–tremolite schist, although these minor lithologies also occur as discrete packages not spatially associated with the Mumba Psammite.

The Mumba Psammite forms three subparallel southeast-trending belts, each about 3–10 km wide and with strike lengths exceeding 50 km (Fig. 1). The distribution of the minor unnamed lithologies is less well defined, forming disharmonic, rootless infolds within the Mumba Psammite or, more commonly, as folded imbricate sheets within the Halfway Gneiss. Contacts with most other rock units are tectonic, although the Mumba Psammite rests unconformably on the Halfway Gneiss in rare, low-strain pockets on the southern part of Yinnetharra† (Sheppard et al., 2008b). Also within these low-strain zones, the presence of discontinuous, 20–50 cm thick quartzite horizons, and 1–3 cm thick coarser grained psammitic layers, commonly define relict bedding.

All lithologies within the Moogie Metamorphics have been metamorphosed in the upper amphibolite facies

* Full references for GSWA samples are provided in Appendix 1 for ease of reference.

† Capitalized names refer to GSWA 100k series maps unless otherwise stated.

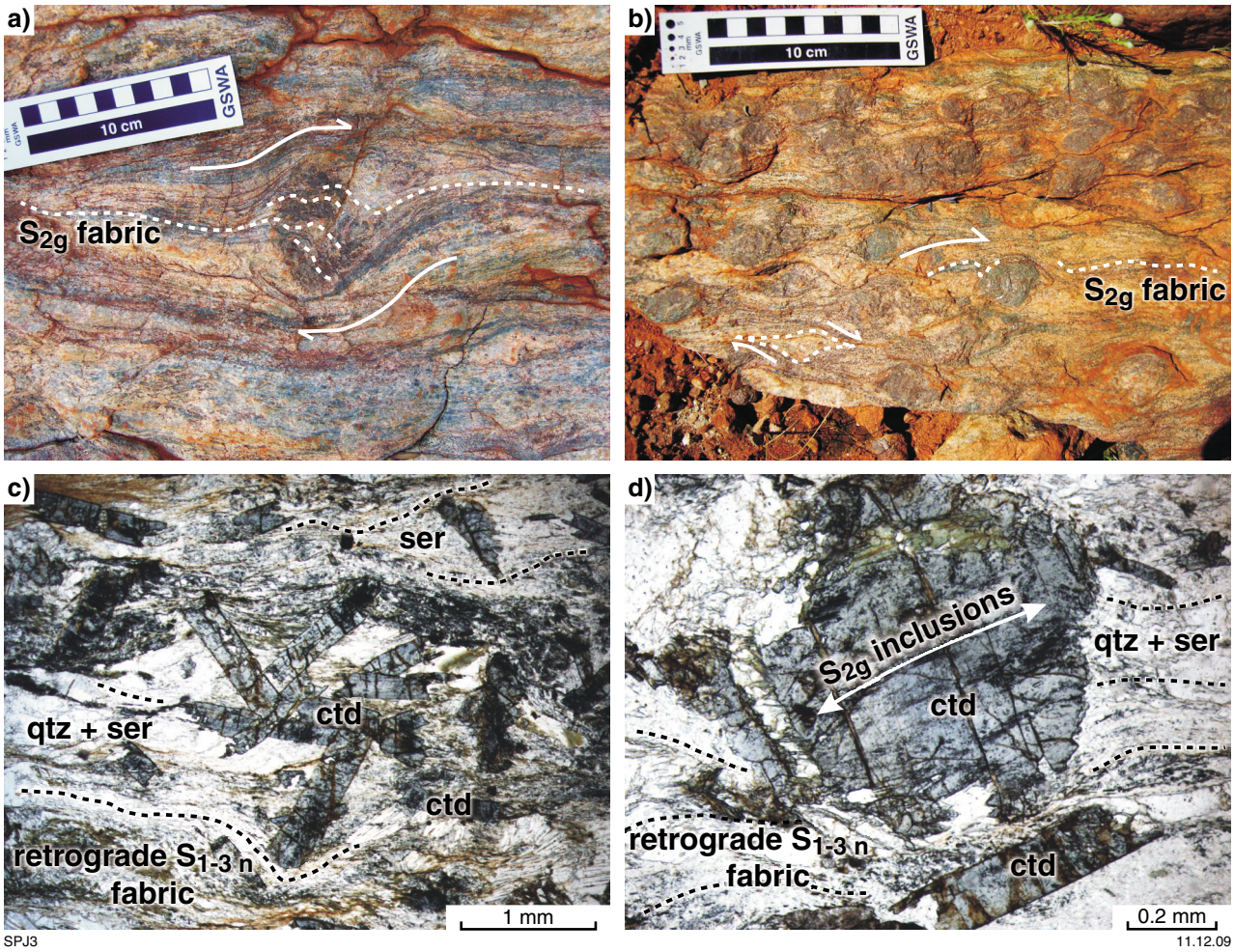


**Figure 3.** **$D_{2g}$ and post-Glenburgh Orogeny structures and metamorphic assemblages of variably retrogressed pelitic gneisses and schists of the Mumba Psammite: a) retrogressed pelitic diatexite from Mount Dalgety (sample GSWA 184161), with a 7 cm diameter garnet porphyroblast (now pseudomorphed by chloritoid) set within a compositionally banded, ner grained matrix of quartz–chloritoid–sericite–chlorite(–biotite). The garnet porphyroblast has undergone dextral rotation during growth synchronous with the $D_{2g}$ event; b) crenulated pelitic schist studded with 5–10 mm diameter garnet porphyroblasts. Again these porphyroblasts preserve evidence for dextral shear; c) photomicrograph (plain polarized light) of a retrogressed semipelitic Moogie Metamorphics schist with 0.5–1 mm long tabular chloritoid (ctd) porphyroblasts growing in random orientations within, and across, a retrograde $S_{1-3n}$ fabric comprised of quartz (qtz) and sericite (ser); d) photomicrograph (plain polarized light) of a retrogressed semipelitic Moogie Metamorphics schist with a mm-wide garnet porphyroblast texturally pseudomorphed by chloritoid (ctd).**

with the widespread production of garnet, ?staurolite, and sillimanite porphyroblasts and variably developed migmatitic textures in pelitic to semi-pelitic lithologies; garnet and diopside in calc-silicate lithologies; and the local growth of diopside porphyroblasts within amphibole- and plagioclase-bearing mafic rocks. The psammitic and pelitic lithologies have been subjected to intense retrograde metamorphism and shearing, with the replacement of peak metamorphic assemblages by greenschist facies assemblages. Garnet and ?staurolite porphyroblasts are invariably pseudomorphed by chloritoid, sillimanite is replaced by sericite, and biotite is replaced by chlorite.

## Mumba Psammite

The Mumba Psammite is the only named unit in the Moogie Metamorphics, and was formerly known as the Mumba Pelite (Occhipinti and Sheppard, 2001). The most southerly belt of schist attributed to this unit occurs on Daurie Creek (GSWA, unpublished data) and Glenburgh (Occhipinti and Sheppard, 2001), centred around Mount Dalgety (Fig. 1; MGA 396618E 7216486N) in the southern part of the Mooloo Zone. Quartz–sericite(–chlorite–biotite–garnet–magnetite) pelitic schist dominates the outcrop, with less abundant layers and lenses of psammitic quartz–sericite(–chlorite–biotite–garnet–magnetite) schist, and chloritoid-bearing schist (quartz–sericite–albite–chloritoid or chloritoid–chlorite–sericite–quartz–albite–garnet) (Occhipinti and Sheppard, 2001). Compositional layering (i.e. bedding), is preserved locally, even though the rocks contain a well-developed bedding-parallel foliation. The pelitic and psammitic schists commonly contain abundant mm- to cm-sized garnet porphyroblasts (Fig. 3a–b) that have been variably retrogressed to chlorite or more commonly pseudomorphed by radially

arranged chloritoid (Fig. 3c–d). An example of a partially retrogressed garnet-bearing pelite was collected for in situ monazite dating (GSWA 164369; MGA 398720E 7221230N), and a garnet-bearing psammitic schist was sampled for detrital zircon dating (GSWA 183275; MGA 393838E 7217124N).

Locally, the psammitic schists contain variable proportions of magnetite in layers that possibly represent bedding; large magnetite porphyroblasts up to 1 cm in diameter have been recorded in these layers (Occhipinti and Sheppard, 2001). A representative sample of these schists were collected for in situ monazite dating (GSWA 168713; MGA 394055E 7217881N).

A small, 20–50 m wide low-strain zone on the southwest slope of Mount Dalgety preserves textural evidence for medium- to high-temperature metamorphism. Relict pelitic diatexites contain euhedral 5–10 cm diameter porphyroblasts of chloritoid-pseudomorphed garnet (Fig. 3a,d). These porphyroblasts are concentrated within more restitic layers of the diatexite, which are now composed of radially arranged chloritoid set within a matrix of sericite–chlorite–quartz(–biotite; Fig. 3c). A sample of this retrogressed pelitic diatexite was collected for detrital zircon analysis (GSWA 184161; MGA 393370E 7217403N).

Within the Paradise Zone, around Paradise Well (Fig. 1; MGA 414390E 7216486N), numerous 10–15 m long discontinuous strips and lenses of pelitic diatexite and metamafic granulite occur within metagranitic gneisses of the Dalgaringa Supersuite. The pelitic diatexites contain leucosomes with a high-temperature, high-pressure assemblage of cordierite–sillimanite–hercynitic spinel–biotite–quartz–corundum (Fig. 4a–e). The alignment of the mesoscale leucosome veins with the earliest regional high-grade fabrics (see following section for definition) suggest that this event occurred during the first phase of the Glenburgh Orogeny. A sample of pelitic diatexite (GSWA 185942; MGA 413802E 7191863N) was sampled for detrital zircon analysis.

Metasedimentary lithologies also outcrop in the Carrandibby Inlier, in the southwestern part of the Paradise Zone (Fig. 1). Quartzites showing mostly granoblastic textures are dominant, but are associated with volumetrically minor quartz–mica(–garnet) schists, both of which are folded and interleaved with granitic gneisses of the Halfway Gneiss and Dalgaringa Supersuite. A sample of fine-grained quartzite from the prominent quartzite ridges at Koolyin Hills (NP20) was sampled for detrital zircon analysis by Kinny et al. (2004).

The central belt of schist in the Mumba Psammite spans Lockier (GSWA, unpublished data), Daurie Creek (GSWA, unpublished data), Yinnetharra (Sheppard et al., 2008b) Pink Hills (GSWA, unpublished data), and Glenburgh (Occhipinti and Sheppard, 2001) within the central part of the Mooloo Zone (Fig. 1). This belt is dominated by quartz–sericite(–chlorite–chloritoid–magnetite) psammitic schists with only minor discontinuous pelitic and quartzite layers. The schists are generally strongly deformed and isoclinally folded so that the preservation of primary sedimentary structures, such as lithological layering, is rare. Evidence for medium- to high-grade metamorphism is also sparse due to the intense greenschist facies metamorphic overprint (Fig. 2); nevertheless, rare migmatitic textures are moderately well preserved in the pelitic to semi-pelitic lithologies. Two samples of psammitic schist — GSWA 164333 (MGA 419800E 7233140N), a chloritoid-rich psammitic schist with abundant sericite, and GSWA 184160 (MGA 383444E 7233694N), a quartz–chlorite–sericite schist — were collected for monazite and detrital zircon geochronology, respectively.

The most northerly belt of schist spans Pink Hills (GSWA unpublished data), Yinnetharra (Sheppard et al., 2008b), and Lockier (GSWA, unpublished data), and transects the Mutherbukin and Limejuice Zones (Fig. 1). The schist is tectonically interleaved with both the Halfway Gneiss and post-1820 Ma meta-igneous rocks of the Moorarie and Durlacher Supersuites. Apart from abundant psammitic schists in the southeast corner of Pink Hills (GSWA, unpublished data), this belt is dominated by massive recrystallized quartzite that contains rare discontinuous layers of more psammitic composition. The quartzite locally contains well developed trough-cross bedding defined by mm-scale layers rich in heavy minerals. In the northwest corner of Yinnetharra (Sheppard et al., 2008b) and northern edge of Lockier (GSWA, unpublished data), steeply dipping 30–50 m thick tourmaline-bearing orthoquartzites form discontinuous, elongate ridges within the younger Durlacher Supersuite metagranites. These units are coarse grained, containing a granoblastic texture with cm-long tourmaline that is usually randomly oriented, but sometimes aligned parallel to joint sets. A sample of this tourmaline-bearing orthoquartzite was collected for detrital zircon analysis (GSWA 187403; MGA 400692E 7286139N).

## Camel Hills Metamorphics

The Camel Hills Metamorphics comprises the Quartpot Pelite and the Petter Calc-silicate, as well as undivided amphibolite and metamorphosed banded iron-formation. All units show evidence for metamorphism in the amphibolite to granulite facies, with the production of voluminous leucosomes and leucogranites within the pelitic lithologies.

There is an apparent decrease in peak metamorphic grade across the Errabiddy Shear Zone, with abundant diatexites present in the north, and medium-grade metasedimentary rocks of both the Quartpot Pelite and Petter Calc-silicate in the southeast and west-southwest (Fig. 2). However, extensive greenschist facies retrogression, and the replacement of peak metamorphic assemblages, took place across the entire Errabiddy Shear Zone during the Capricorn Orogeny (Fig. 2). These two pervasive deformation events have eradicated nearly all primary sedimentary structures.

### Quartpot Pelite

The Quartpot Pelite largely consists of biotite–plagioclase–quartz(–K-feldspar–garnet–sillimanite)

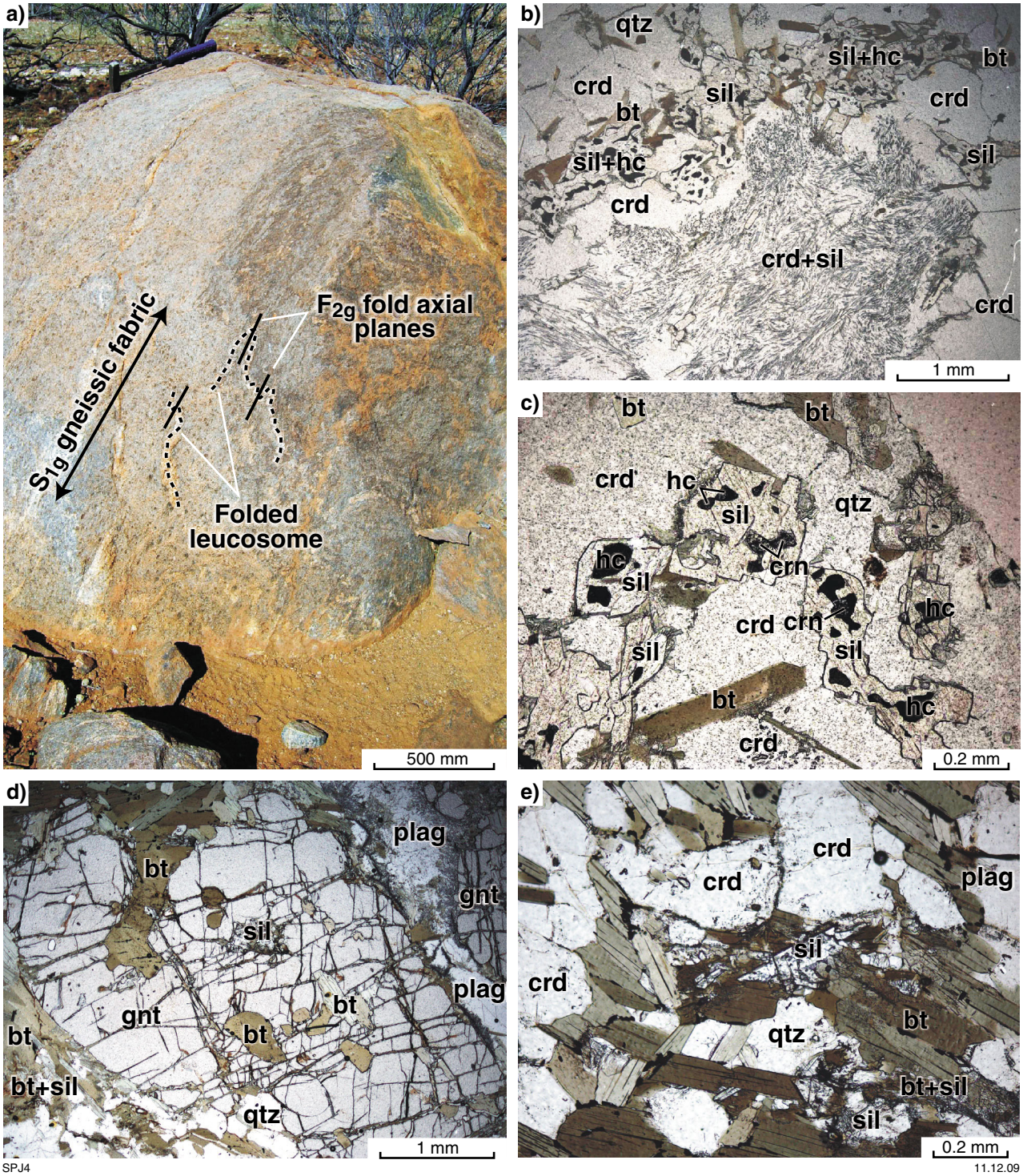


**Figure 4.** Features of pelitic diatexite from Paradise Well on Glenburgh: a) at outcrop scale, the pelitic diatexite (sample GSWA 168942) contains mm- to cm-scale diatexite melt veins that parallel the regional $S_{1g}$ gneissic fabrics, and which are openly folded by $F_{2g}$ folds; b) photomicrograph (plane polarized light) of leucosome from GSWA 168942 showing 5–10 mm diameter cordierite (crd) porphyroblasts with ne grained sillimanite (sil) inclusions, mantled by coarse intergrowths of biotite (bt), and sillimanite–hercynitic spinel (hc)–corundum (crn). Quartz (qtz) is also a major constituent of the mineral assemblage; c) photomicrograph (plane polarized light) of leucosome from GSWA 168942, showing a close-up of the hercynite–sillimanite intergrowths; d) photomicrograph (plane polarized light) of mesosome from pelitic diatextite (GSWA 144823) showing a ~5 mm diameter garnet (gnt) porphyroblast with biotite inclusions, surrounded by plagioclase (plag), biotite, and biotite–sillimanite intergrowths; e) close-up of the biotite–sillimanite intergrowths within GSWA 144823, showing the presence of anhedral cordierite.

pelitic gneiss, migmatitic pelitic gneiss, and psammitic schist, interlayered with minor quartzite, calc-silicate gneiss, and amphibolite. Many of the pelitic gneisses are migmatitic, particularly on northern Erong (GSWA, unpublished data), and extending east-northeast into the region northeast of Errabiddy Homestead (MGA 513577E 7183914N). The migmatites commonly show stromatic, schollen (raft), and nebulitic structures (nomenclature after Mehnert, 1968; Ashworth, 1985; Fig. 5a–c), with medium-grained, heterogeneous siliceous diatexite leucosome locally forming up to 70% of the rock (Occhipinti et al., 2001). Within the leucosomes, lenticular rafts of restite, consisting of refractory psammite and biotite-rich material, are preserved. In places, veins of more homogeneous, externally derived leucosome cut the in situ migmatite. The stromatic migmatites locally grade into nebulitic migmatite, indicating an increase in the amount of in situ partial melting (Occhipinti et al., 2001). At the northern end of the Quartpot Pelite outcrop on Errabiddy (Occhipinti et al., 2009), and on northern Erong (GSWA, unpublished data), medium-grade muscovite–biotite(–garnet) pelitic gneiss and schist contain small amounts of leucosome, but otherwise show no evidence of melting (Sheppard and Occhipinti, 2000).

Subsequent greenschist facies metamorphism during the Capricorn Orogeny is considered responsible for the retrogression and replacement of peak metamorphic assemblages (Fig. 2). Plagioclase is extensively replaced by fine-grained sericite–epidote–albite; garnet is pseudomorphed (in lower strain zones) by biotite–muscovite; and sillimanite is entirely replaced by mats of fine-grained sericite (Sheppard and Occhipinti, 2000). Deformation during the Capricorn Orogeny appears to be restricted to numerous metre-wide subvertical brittle–ductile shear zones (Sheppard and Occhipinti, 2000), allowing textural preservation of the medium- to high-grade metamorphic fabrics and assemblages (e.g. texturally preserved garnet porphyroblasts) in extensive low-strain zones. One unretrogressed medium-grade psammitic schist — GSWA 168944 (MGA 449690E 7171380N) — and two examples of retrogressed pelitic diatexite — GSWA 142905 (MGA 547712E 7210422N) and GSWA 142910 (MGA 477900E 7184200N) — were sampled for detrital zircon geochronology. All samples

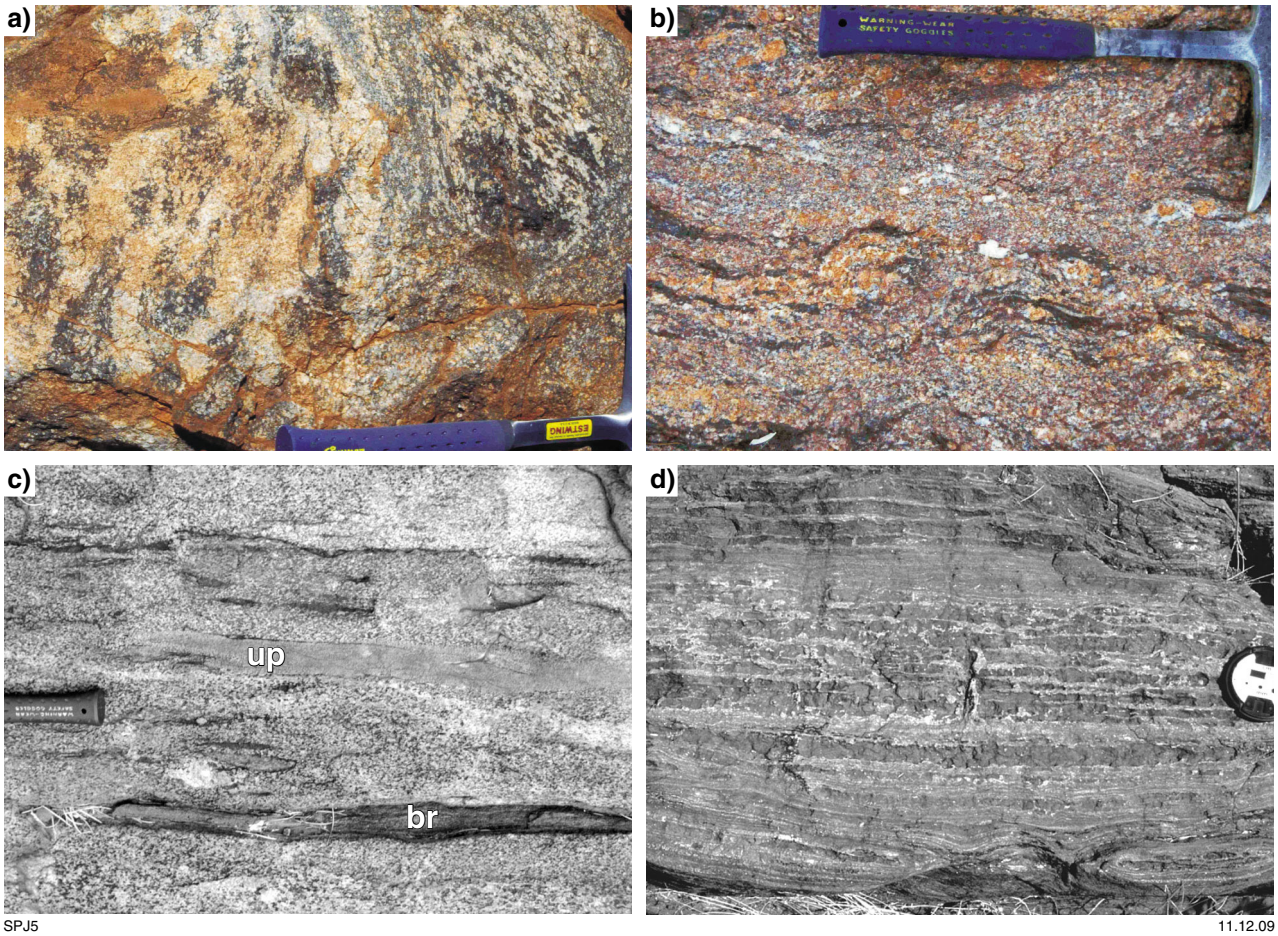


**Figure 5. Migmatitic gneisses of the Camel Hills Metamorphics: a) nebulitic pelitic migmatite of the Quartpot Pelite, showing diatexite melts with discontinuous biotite-rich restitic layers; b) stromatic pelitic migmatite of the Quartpot Pelite; c) schollen migmatite of the Quartpot Pelite, showing diatexite melt with inclusions of dark biotite-rich restite (br), and lumps of unmelted psammite (up). Modified from Sheppard and Occhipinti, 2000, g. 6a; d) Petter Calc-silicate, showing mm- to cm-scale gneissic banding; after Occhipinti et al., 2001, g. 16a. Hammer scale in a–c) 30cm long; lens cap in d) 5 cm in diameter.**

contain greenschist facies mineral assemblages, with the retrogressed pelitic diatexites containing minor, highly altered garnet relics.

### Petter Calc-silicate

The Petter Calc-silicate is composed of clinopyroxene–plagioclase(–epidote–quartz–hornblende–grossular) calc-silicate schist and gneiss, interlayered with quartzite and quartz–diopside rock, and minor pelitic schist or migmatitic pelitic gneiss and amphibolite (Sheppard and Occhipinti, 2000). The calc-silicate gneiss is compositionally layered, with alternations of tremolite- and clinopyroxene-rich layers, and quartz-rich layers up to several centimetres thick (Sheppard and Occhipinti, 2000). The calc-silicate rocks range from fine- to coarse-grained, with radiating bundles of pale-green tremolite–actinolite or clinopyroxene within the compositional layering (Fig. 5d). About 2.5 km north-northwest of Erong Homestead (locality 10a of Occhipinti et al., 2001; MGA 465651E 7174737N), a raft of Petter Calc-silicate within the Erong Granite consists of calc-silicate rock and a distinctive tremolite–diopside–talc rock, which was interpreted as a para-amphibolite. The calc-silicate and para-amphibolite contain a fine, 1–10 mm thick compositional layering, which is interpreted as original bedding. The magnesium-rich mineralogy may be indicative of an evaporite protolith (Occhipinti et al., 2001). Like the Quartpot Pelite, the peak mineral assemblages have been overprinted and retrogressed during the Capricorn Orogeny (Fig. 2). Most of the tremolite appears to be secondary in origin, having replaced former clinopyroxene, which now exists mostly as relict inclusions. Several samples were collected for detrital zircon geochronology but only one sample — GSWA 142908 (MGA 480870E 7180180N), a quartz-rich (~75%) clinopyroxene-bearing calc-silicate gneiss — yielded any zircon.

## Deformation and metamorphism

Two main deformation events are attributed to the Glenburgh Orogeny ($D_{1g}$ and $D_{2g}$), although the associated fabrics and mineral assemblages were pervasively modified during later deformation and retrograde metamorphism (i.e. during the 1820–1770 Ma Capricorn Orogeny). Occhipinti et al. (2004) provided an excellent summary of these structural and metamorphic elements; nevertheless, continued mapping in the region has led to further refinements of the structural–metamorphic evolution, which are summarized here.

### $D_{1g}$ deformation and metamorphism

The earliest foliation ($S_{1g}$) appears to be restricted to the Paradise Zone in the southern part of the Glenburgh Terrane. The dominant medium- to high-grade $S_{1g}$ foliation is developed in strongly layered 2005–1985 Ma-aged metatonalites, metagranodiorites, and metamonzogranites of the Dalgaringa Supersuite (Occhipinti and Sheppard, 2001; Occhipinti et al., 2004). Tight to isoclinal, moderately plunging folds are only locally developed, and pre-date the planar metadiorite and mesocratic metatonalite dykes that intruded across fabrics subparallel to the axial planes of the folds (Occhipinti et al., 2004). These dykes are dated at 1989 ± 3 Ma (GSWA 142933) and 1987 ± 4 Ma (GSWA 142923), respectively. Intercalated strips of amphibolite and the presence of abundant, relict garnet porphyroblasts within many of the Dalgaringa Supersuite metagranites indicate that $D_{1g}$ occurred in the upper amphibolite facies (Occhipiniti and Sheppard, 2001). However, in the centre of the Paradise Zone around Paradise Well, discontinuous lenses of metamafic granulite and pelitic diatexite indicate that some parts of the Dalgaringa Supersuite were metamorphosed in the granulite facies (Fig. 2). In general, the metamafic rocks comprise either hypersthene–clinopyroxene–plagioclase or plagioclase–clinopyroxene–hypersthene(–garnet; Occhipinti and Sheppard, 2001).

The pelitic diatexites are coarse-grained granoblastic rocks with mm- to cm-scale discontinuous leucosomes that parallel the regional $S_{1g}$ gneissic fabrics (Fig. 4a). The diatexite leucosomes (GSWA 185942) contain an ?equilibrium assemblage of cordierite–sillimanite–hercynitic spinel–biotite–quartz–corundum. Cordierite forms porphyroblasts 1–5 mm in diameter, the core regions of which are intergrown with abundant fibrolite mats (Fig. 4b). The outer 0.25–1 mm of the porphyroblasts are free of sillimanite, but are partially mantled by coarse-grained (0.5–2 mm diameter) euhedral sillimanite blades (Fig. 4b). The cores of these sillimanite grains host hercynitic spinel and corundum (Fig. 4c). Tabular biotite blades are intergrown within the cordierite–sillimanite coronas and appear to be in textural equilibrium with these phases; however, in the quartz–cordierite–biotite matrix, the biotite blades are mantled by fringes of fibrolite and cordierite and therefore not in textural equilibrium. The mesosomes (GSWA 144823) contain an assemblage of garnet–sillimanite–gahnitic spinel–plagioclase–biotite–quartz. Garnet occurs within 10–20 mm thick biotite-rich seams, and forms porphyroblasts, 5–10 mm in diameter, that contain inclusions of both biotite and sillimanite (Fig. 4d). Outside of these seams, quartz and plagioclase are more prevalent, and tabular biotite blades exsolve small pockets of ilmenite, being mantled themselves by fringes of fibrolite and cordierite (Fig. 4e). Also present are discontinuous sillimanite-rich seams up to 10–15 mm wide, composed of euhedral sillimanite blades with minor biotite–quartz–plagioclase; in these seams, sillimanite cores are replaced by anhedral gahnitic spinel.

The assemblages documented above, along with mesoscale leucosome veins, imply moderate- to high-temperature conditions conducive to incipient melting. The replacement of hercynitic spinel with corundum in almandine-bearing lithologies is interpreted by Schulters and Bohlen (1988) to indicate high-temperature and moderate- to high-pressure conditions in the range ~800–1000°C and 7–10 kbar. The alignment of the mesoscale melt fabrics with the regional $S_{1g}$ foliation suggest that this melting event was synchronous with $D_{1g}$. The structural relationships

between these granulite facies rocks and the surrounding amphibolite facies rocks are unclear, but it is suggested that the two became juxtaposed after the $D_{1g}/M_{1g}$ event (Occhipinti et al., 2004).

No unequivocal $D_{1g}$ fabrics are evident outside the Paradise Zone. In the Mooloo Zone, Occhipinti et al. (2004) suggested that an early, openly folded gneissosity in the Halfway Gneiss could be correlated with $S_{1g}$ fabrics in the Paradise Zone, since the gentle subhorizontal axial planes are parallel to $D_{2g}$ faults and shears. However, considering the pervasive nature, and heterogeneous style of deformation and overprinting relationships of the $D_{2g}$ event (see next section), this gneissic fabric is more likely an early $S_{2g}$ fabric, comparable in age with the high-grade $S_{2g}$ migmatitic fabrics preserved in the Moogie Metamorphics.

# $D_{2g}$ deformation and metamorphism

$D_{2g}$ fabrics, folds and metamorphic assemblages are prevalent throughout the Paradise and Mooloo Zones of the Glenburgh Terrane, and within the Errabiddy Shear Zone (Fig. 1).

## Paradise Zone

In the Paradise Zone, $D_{2g}$ is characterized mainly by mesoscopic tight to isoclinal upright folds, accompanied by a penetrative $S_{2g}$ axial planar foliation (Fig. 4a; Occhipinti and Sheppard, 2001), especially well developed in the c. 1975 Ma Nardoo Granite. Rare, $F_{2g}$ fold hinges in the older parts (2005–1985 Ma) of the Dalgaringa Supersuite and in the pelitic diatexite (Fig. 4a) indicate that the $S_{2g}$ fabric is developed subparallel to both the gneissic banding and $S_{1g}$ foliation. The grade of metamorphism during $D_{2g}$ deformation is difficult to establish as there appears to be no significant retrogression or overprinting of the higher grade granulite facies rocks; however, this is probably due to the anhydrous nature of the $M_{1g}$ assemblages (Occhipinti et al., 2004). In the amphibolite facies gneisses, garnet appears to be replaced by clots of fine-grained biotite; in the calc-silicates, pargasite and diopside are rimmed or replaced along fractures by tremolite (Occhipinti et al., 2004), while the gneissic fabric in the Nardoo Granite is defined by biotite–quartz–oligoclase to andesine–epidote (Occhipinti and Sheppard, 2001), suggesting that $M_{2g}$ metamorphism occurred in the lower amphibolite facies.

## Mooloo Zone

In the Mooloo Zone, heterogeneous $D_{2g}$ fabrics and folds are developed pervasively throughout the Moogie Metamorphics and Halfway Gneiss. The earliest structure preserved in the Moogie Metamorphics is a subhorizontal mm- to cm-scale gneissic banding that reflects discontinuous leucocratic melt segregations, formed during migmatization. In the unmelted psammitic lithologies, this $S_{2g}$ fabric is represented as an intense bedding-parallel composite foliation. Although the medium- to high-grade $M_{2g}$ metamorphic diatexite assemblages have been completely retrogressed to a much lower grade (during the Capricorn Orogeny; Fig. 2), many localities still show particularly well-preserved diatexite textures (Fig. 3a). At one locality in particular, on the southwestern slopes of Mount Dalgety on Daurie Creek (GSWA unpublished data), the retrogressed pelitic diatexite (sample GSWA 184161) contains euhedral 5–10 cm porphyroblasts of garnet (pseudomorphed by chloritoid) that sit within 1–10 cm thick, biotite-rich restitic layers (Fig. 3a), which are wrapped by discontinuous leucosomes of quartz–feldspar–sillimanite (now sericite). The pseudomorphed garnet porphyroblasts contain coarse quartz and biotite inclusion trails, continuous with the external $S_{2g}$ fabric, some of which have undergone dextral shear rotation (Fig. 3a). This suggests that garnet grew as a synkinematic porphyroblast during $D_{2g}$ deformation and dextral shearing. Similar relationships can be also observed further north on Yinnetharra (Sheppard et al., 2008b; Fig. 3b). Within the more psammitic parts of the Moogie Metamorphics, the local preservation of bedding (graded bedding and compositional layering) alongside diatexite textures in the pelites demonstrate that melting, migmatization, and porphyroblast growth during $D_{2g}$ was a function of composition, rather than of varying metamorphic grade. Due to the intense retrogression of the $M_{2g}$ metamorphic assemblages, it is difficult to determine the peak conditions attained during $D_{2g}$; however, the presence of both garnet and sillimanite as an equilibrium assemblage within the pelitic diatexites, and the abundance of leucosome suggest the dominance of biotite dehydration-melting reactions, placing a lower temperature limit of ~750°C, with pressure conditions somewhere between 2 kbar and 8 kbar (Spear, 1993).

At most localities the Halfway Gneiss contains a mm- to cm-scale gneissic banding defined by alternating leucocratic (quartz–feldspar) and mesocratic (biotite–quartz–feldspar–hornblende) layers with abundant discontinuous 1–25 cm thick pegmatites (Fig. 6a). On northern Daurie Creek (GSWA, unpublished data), the gneissic fabric in the Halfway Gneiss contains abundant leucocratic material dated at c. 2005 Ma (Occhipinti et al., 2001), providing a maximum age for its development. On the northern part of Glenburgh (Occhipinti and Sheppard, 2001) and Daurie Creek (GSWA, unpublished data), the Halfway Gneiss is intercalated with pelitic diatexites and psammitic schists of the Moogie Metamorphics, but itself contains only a simple, openly folded gneissic fabric. This tentatively suggests that the Halfway Gneiss was not affected by both Glenburgh events, and that the main gneissic fabric is contemporaneous with the medium- to high-grade $S_{2g}$ fabrics within the schists of the Moogie Metamorphics. Further north, on southern Yinnetharra (Sheppard et al., 2008b), these gneissic fabrics are commonly complexly folded showing both type 2 and 3 interference folds (Ramsey and Huber, 1987), most of which show no consistency in orientation, and no new fabric development (Fig. 6b). The age of this refolding event(s) is unclear but may either be related to a locally prolonged $D_{2g}$ deformation, or Paleoproterozoic to Neoproterozoic reworking events (Johnson et al., 2009).

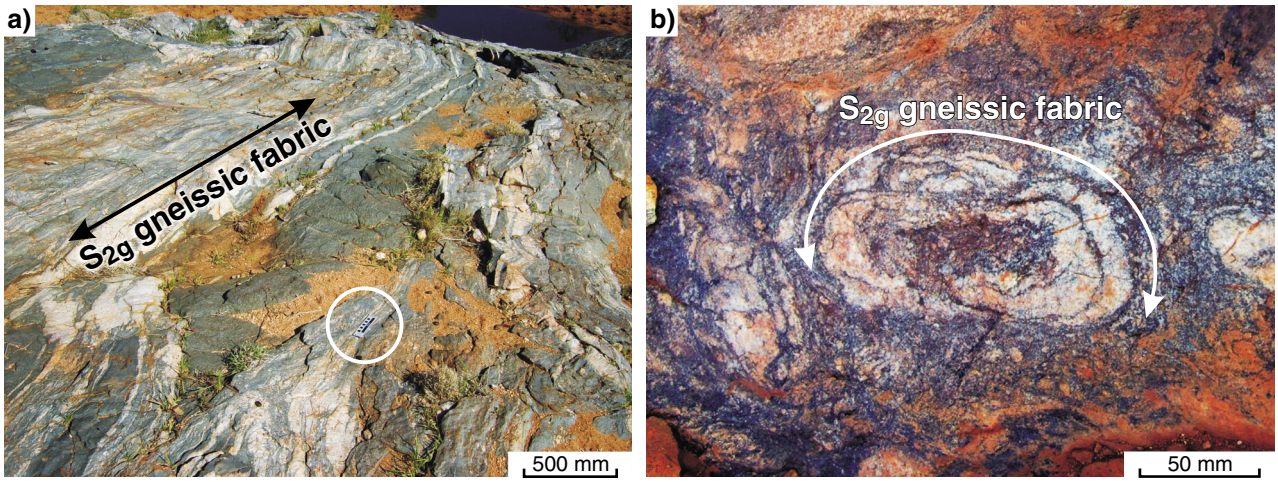


**Figure 6.** **$D_{2g}$ structures within the Halfway Gneiss: a) pegmatite banded gneiss typical of the mesocratic Halfway Gneiss. The main gneissic fabric formed during the $D_{2g}$ event of the Glenburgh Orogeny. 10 cm scale bar circled; b) the main $S_{2g}$ gneissic fabric of the Halfway Gneiss is locally folded into sheath folds where the fold hinges are parallel to the stretching lineation. This would have occurred during a single constrictional-type deformation event.**

The continuity of medium- to high-grade $S_{2g}$ fabrics in the Moogie Metamorphics with those in the Halfway Gneiss suggests that $M_{2g}$ was at similar metamorphic grade in both units.

## Errabiddy Shear Zone

All lithologies in the Errabiddy Shear Zone are in fault-bounded contact with each other and contain a single, pervasive fabric (S–L) associated with $D_{2g}$ deformation and metamorphism. Archean granitic rocks, such as the Warrigal Gneiss (Sheppard and Occhipinti, 2000), contain a gneissic fabric defined by alternating mesocratic and leucocratic layers. Rocks of the Camel Hills Metamorphics contain either a strong migmatitic or gneissic fabric, depending on their lithological composition and whether or not they were melted. The $S_{2g}$ fabric was originally flat-lying and parallel to lithological contacts, suggesting that it developed during tectonic imbrication. The $L_{2g}$ mineral stretching lineation is shallow plunging, suggesting low-angle transport directions (Occhipinti et al., 2004). In the pelitic to semipelitic rocks of the Quartpot Pelite, intense migmatization produced alternating mm- to cm-scale mesocratic and leucocratic layers (Fig. 5a–c) consisting of sillimanite–biotite and quartz–plagioclase–K-feldspar, respectively. The growth of abundant garnet over this composite $S_{2g}$ foliation–layering suggests that garnet growth occurred synchronously with, or slightly after, $D_{2g}$ deformation (Occhipinti et al., 2004). Similar gneissic structures are observed in the Petter Calc-silicate.

The retrogression of these $M_{2g}$ assemblages during the Capricorn Orogeny (Fig. 2) preclude the calculation of precise peak pressure and temperature conditions for $M_{2g}$; however, the similarity of the metamorphic assemblages to those of the Moogie Metamorphic diatexites suggests that similar conditions prevailed in the two areas (Fig. 2). In the southwestern part of the Errabiddy Shear Zone, the pelitic and semipelitic lithologies of the Quartpot Pelite lack any features indicative of melting and migmatization (Fig. 2). They contain an assemblage of quartz–muscovite–biotite with minor garnet and plagioclase, consistent with metamorphism in the mid-amphibolite facies (Sheppard and Occhipinti, 2000), suggesting that there was a decrease in the grade of $M_{2g}$ from northeast to southwest across the Errabiddy Shear Zone (Occhipiniti et al., 2004).

# Post-Glenburgh Orogeny deformation and metamorphism

The Glenburgh Terrane, Errabiddy Shear Zone, and Yarlarweelor Gneiss Complex have all been pervasively deformed and metamorphosed after the Glenburgh Orogeny, resulting in the refolding and reorientation of the $D_{1g}$ and $D_{2g}$ structures, and the replacement of peak $M_{1g}$ and $M_{2g}$ metamorphic assemblages with much lower grade assemblages. Much of the reworking appears to be related to the 1820–1770 Ma Capricorn Orogeny (Fig. 2), although this event had little effect in the Paradise Zone, being represented only by a weak, but penetrative, upright fabric (Occhipinti and Sheppard, 2001).

In the Mooloo Zone, an intense upright axial planar schistosity trending roughly southeast was developed throughout both the Halfway Gneiss and Moogie Metamorphics. This was accompanied by the development of regional- to local-scale upright isoclinal folds, shallow-plunging mineral lineations developed alongside local sinistral S–C fabrics, and the intense retrogression of peak $M_{2g}$ metamorphic assemblages to lower greenschist facies assemblages (Fig. 2). In many cases, garnet and what is inferred to have been staurolite (due to their relict tabular shape) are perfectly pseudomorphed by radially arranged chloritoid crystals (Fig. 3c–d) within the Moogie Metamorphics. Locally, the presence of schists containing strongly oriented chloritoid suggests either that low-grade metamorphism outlasted deformation at the regional scale,

or that shear-dominated deformation was partitioned into discrete shear zones. The age of this event is well constrained in the southern Mooloo Zone as it appears to post-date the intrusion of the c. 1810 Ma Dumbie Granodiorite, and pre-date the intrusion of the c. 1800 Ma Scrubber Granite. These relationships indicate that the main upright schistose fabric, at least in the southern Mooloo Zone, is related to the early-Capricorn structures present elsewhere in the region, i.e. they are $D_{1n}$ structures (Occhipinti and Sheppard, 2001).

In the Errabiddy Shear Zone and Yarlarweelor Gneiss Complex, $D_{1n}$ structures similar to those in the Mooloo Zone are developed. These are represented by tight, upright, shallow-plunging folds with a strongly developed $S_{1n}$ axial planar schistosity, which formed synchronously with the retrogression of $M_{2g}$ metamorphic assemblages (Sheppard and Occhipinti, 2000). Throughout the Errabiddy Shear Zone, a shallow-plunging mineral stretching lineation(s) defined by biotite and white mica is prevalent (Occhipinti et al., 2004). Some of these lineations appear to be associated with dextral strike-slip movement and, in the east, appear to post-date the c. 1800 Ma Kerba Fault (Reddy and Occhipinti, 2004). Irrespective of age, the consistent dextral strike-slip kinematics (Reddy and Occhipinti, 2004) imply significant syn- and post-$D_{2g}$ dextral movements on the Errabiddy Shear Zone.

The precise effects of much later Meso- to Neoproterozoic deformation on the region are currently unknown. In the Mutherbukin Zone on northern Yinnetharra (Sheppard et al., 2008b) and southern Mount Phillips (Sheppard et al., 2008c), sedimentary protoliths to the c. 1680 Ma Pooranoo Metamorphics were metamorphosed and deformed at medium grade during the 1030–955 Ma Edmundian Orogeny (Sheppard et al., 2007; Johnson et al., 2009). Further south in the same zone, the Pooranoo Metamorphics and the Edmund Group on southern Yinnetharra (Sheppard et al., 2008b) and Pink Hills (GSWA, unpublished data), and northern and central Landor, Glenburgh (Sheppard and Occhipinti, 2000; Occhipinti and Sheppard, 2001) and Daurie Creek (GSWA, unpublished data), show a similar deformation history. These metasedimentary packages were folded into several regional-scale upright, tight to isoclinal folds with the development of a pervasive, coarsely spaced cleavage/schistosity.

An $^{40}Ar/^{39}Ar$ thermochronology study of muscovite and biotite from rocks within and around the Errabiddy Shear Zone (Occhipinti, 2007) has revealed that numerous units have Ar cooling ages (mostly through temperatures of about 300–350°C) in the range 960–820 Ma. Although no ductile planar fabrics appear to have been developed at this time — it is possible that some of the mineral stretching lineations are of this age — there must have been considerable brittle–ductile reactivation of older structures, possibly resulting in the tectonic uplift of parts of the region (Occhipinti, 2007).

The western end of the Capricorn Orogen is dissected by a network of metre-scale, brittle–ductile, dextral strike-slip faults. These faults offset dykes of the c. 755 Ma Mundine Well Dolerite Suite, and have been dated at c. 570 Ma by in situ $^{40}Ar/^{39}Ar$ dating of newly grown, fine-grained muscovite that forms the S-planes within a dextral S–C fabric (Bodorkos and Wingate, 2007). This event is known as the Mulka Tectonic Event (Sheppard et al., 2008a), and was responsible for regional-scale dextral movements of up to 35 km across the Chalba Shear Zone (Sheppard et al., in prep. b).

# Ion microprobe U–Pb zircon geochronology

U–Pb dating of both detrital and metamorphic zircon using SIMS was conducted by GSWA using the SHRIMP II at the John de Laeter Centre of Excellence in Mass Spectrometry at Curtin University of Technology. These data were collected over a number of years (1998 to present); details of sample analytical conditions are available from published GSWA Geochronology Records, hyperlinked references to which are provided in Appendix 1. Descriptions of the dated rocks and their geological settings are provided in the previous section, while the following sections describe the characteristics of the dated zircons, including features visible in CL images, and summarize the analyses and interpretation for each sample. Weighted mean ages are calculated from $^{204}Pb$-corrected $^{207}Pb/^{206}Pb$ ratios, and quoted with 95% confidence intervals, unless otherwise specified, and with values of mean square of weighted deviates (MSWD).

## Moogie Metamorphics

### *GSWA 184161: retrogressed pelitic diatexite (Mumba Psammite)*

Zircon crystals from this sample range from pale brown to black, are rounded, and 50–100 μm long with aspect ratios up to 5:1. Surface pitting and a high degree of rounding are consistent with mechanical abrasion during sedimentary transport. Some grains display concentric growth zoning typical of zircons formed during igneous crystallization (Corfu et al., 2003). Zircon cores range from dark to bright in CL images, and all grains are overgrown by zircon rims that are dark under CL (Fig. 7a).

Fifty-four analyses were obtained from 53 zircons; results are referenced in Appendix 1. The analyses obtained from detrital cores and rims range from concordant to discordant. Fourteen analyses that are >5% discordant and have undergone variable amounts of radiogenic Pb loss, and two analyses interpreted as mixtures between core and rim, are not considered geologically significant. The remaining 23 analyses of 23 detrital zircon cores yield $^{207}Pb/^{206}Pb$ dates of 2743–2369 Ma (Fig. 8a), and include several age components (Fig. 8b). The youngest detrital zircon grain analysed has a $^{207}Pb/^{206}Pb$ date of 2369 ± 8 Ma, providing an estimate for the maximum age of deposition for the metasediment's protolith (Table 1). A more conservative estimate is given by the next two youngest analyses, which indicate a weighted mean $^{207}Pb/^{206}Pb$ date of 2485 ± 12 Ma (MSWD = 0.094). Fifteen analyses of homogeneous CL-dark rims have consistently low Th/U ratios (<0.09) and moderate uranium content (~ 600 ppm). They yield a weighted mean $^{207}Pb/^{206}Pb$ date

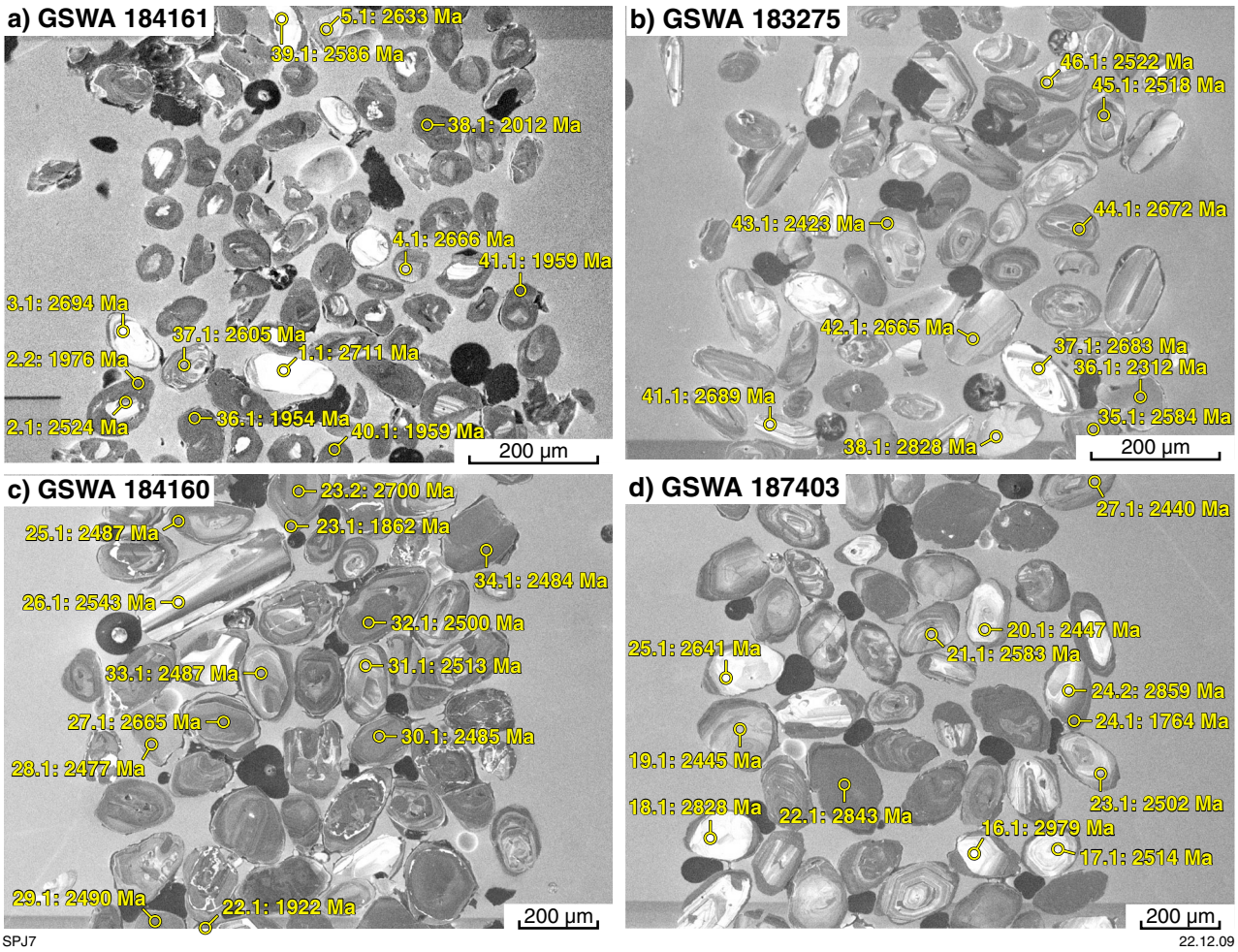


**Figure 7.** **Cathodoluminescence (CL) images of representative zircon dated from the Mumba Psammite. The location of SHRIMP analysis sites are shown along with the analysis number and $^{207}Pb/^{206}Pb$ age. SHRIMP U–Pb data for these samples are tabulated in Appendix 1.**

of 1952 ± 4 Ma (MSWD = 1.4; Fig. 8a inset), interpreted to date the timing of high-grade metamorphism.

### *GSWA 183275: psammitic schist (Mumba Psammite)*

Zircons from this sample range from colourless to pale brown, and many grains have abraded terminations. The zircons are 50–200 µm long and rounded to elongate, with aspect ratios up to 5:1. Surface pitting and the high degree of rounding on many grains are consistent with mechanical abrasion during sedimentary transport. Most grains exhibit concentric growth zoning, which in many cases is truncated at grain edges (Fig. 7b). No metamorphic zircons or overgrowths were identified in this sample.

Fifty-one analyses were obtained from 51 zircons; results are referenced in Appendix 1. Most analyses are concordant or only slightly discordant. Five analyses are >5% discordant, and have undergone radiogenic Pb loss. The dates from these five analyses are unreliable, and are not considered geologically significant. The remaining 46 analyses yield $^{207}Pb/^{206}Pb$ dates of 3007–2300 Ma (Fig. 8c), and indicate several age components (Fig. 8d). The four youngest analyses (Fig. 8c, inset) yield a weighted mean $^{207}Pb/^{206}Pb$ date of 2306 ± 12 Ma (MSWD = 1.4), interpreted as the maximum depositional age of the protolith of this metasedimentary rock (Table 1).

### *GSWA 184160: psammitic schist (Mumba Psammite)*

Zircons from this sample range from pale pink to pale brown, are 50–300 µm long, and are rounded to elongate, with aspect ratios up to 5:1. Some crystals exhibit pitted surfaces and abraded terminations, consistent with mechanical abrasion during sedimentary transport. In CL images, most grains display concentric growth zoning, which in many cases is truncated at grain edges by rims which are dark and structureless in CL images (Fig. 7c).

Sixty-four analyses were obtained from 60 zircons; results are referenced in Appendix 1. Most analyses from both detrital cores and rims are concordant or only slightly discordant. Four analyses are >5% discordant, and have undergone radiogenic Pb loss. The dates from

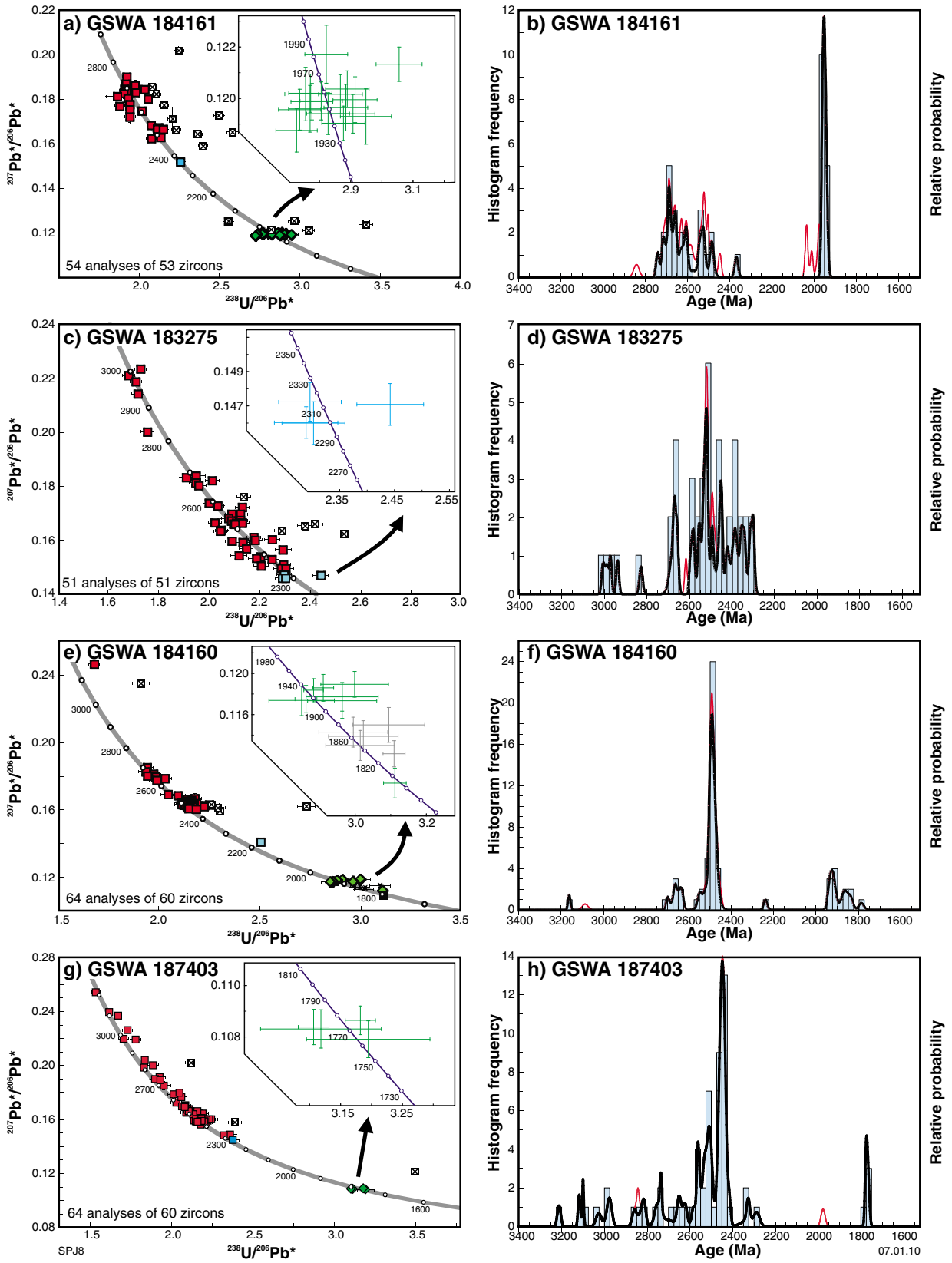


**Figure 8.** U–Pb concordia diagrams and probability density distribution plots for detrital and metamorphic zircons from the Mumba Psammite southern (a–d), central (e–f), and northern (g–h) belts. Red squares are for detrital zircon, blue squares and blue crosses (inset) are for the youngest detrital zircon in the metasediment, green diamonds and crosses (inset) are for metamorphic zircon. Analyses shown with an 'x' or as a grey cross (inset) are mixed ages, whilst zircon >5% discordant are shown in the main plots as squares with crosses. U–Pb SHRIMP data for these samples are tabulated in Appendix 1.The black curve in the probability density distribution plots represents data that is <5% discordant, whereas the red curve is for all data regardless of discordance. Histogram boxes binned at 25 m.y.

**Table 1. Table summarizing the maximum depositional age and metamorphic ages of dated samples and packages**

| *Sample number* | *Maximum deposition age (Ma)* | *Metamorphic age (Ma)* |
|---|---|---|
| **Camel Hills Metamorphics** | | |
| ***Quartpot Pelite — depositional age range 2000–1955 Ma*** | | |
| 142910 | 2031 ± 6 | 1955 ± 7 |
| 142905 | 2001 ± 26 | 1952 ± 14 |
| 168944 | 2027 ± 4 | |
| ***Petter Calc-silicate — depositional age range 2600–1945 Ma*** | | |
| 142908 | 2608 ± 4 | 1944 ± 5 |
| ***Moogie Metamorphics — depositional age range 2240–2125 Ma*** | | |
| 184161 | 2369 ± 8 | 1952 ± 4 |
| 183275 | 2306 ± 12 | |
| 184160 | 2240 ± 8 | 1928 ± 8, 1788 ± 12 |
| 187403 | 2286 ± 13 | 1772 ± 6 |
| NP20 (Kinny et al., 2004) | 2290–2270 | 1934 ± 43 |
| 164369 | | 2125 ± 9 (m), 2126 ± 10 (z), 1958 ± 6 (m), 1959 ± 8 (z) |
| 168713 | | 1966 ± 7 (m) |
| 164333 | | 1947 ± 11 (m) |
| ***Pelitic diatexite — depositional age range 2080–2000 Ma*** | | |
| 185942 | 2083 ± 7 Ma | 1997 ± 10 Ma |

**NOTE:** Letters following metamorphic age dates indicate mineral from which analysis was obtained. (m) = monazite, (z) = zircon

these six analyses are unreliable, and are not considered geologically significant. The remaining 60 analyses of 57 zircons yield $^{207}Pb/^{206}Pb$ dates of 3165–1795 Ma (Fig. 8e), and define several age components (Fig. 8f). Of these, 45 analyses of concentrically-zoned detrital cores indicate dates of 3165–2239 Ma. The youngest detrital zircon grain analysed indicated a date of 2239 ± 8 Ma, which represents a maximum age for deposition of the protolith for this metasedimentary rock (Table 1). However, a more conservative estimate of the maximum depositional age can be based on the the next 30 youngest analyses, which agree to within analytical precision and yield a weighted mean date of 2488 ± 3 Ma (MSWD = 1.3).

Thirteen analyses of 13 zircon rims indicate $^{207}Pb/^{206}Pb$ dates of 1940–1795 Ma. Seven analyses of seven rims yield a weighted mean $^{207}Pb/^{206}Pb$ date of 1928 ± 7 Ma (MSWD = 1.1; Fig. 8e inset), interpreted as the age of high-grade metamorphism and also a minimum age of deposition for the sedimentary precursor. Five analyses of five rims yield a weighted mean $^{207}Pb/^{206}Pb$ date of 1857 ± 22 Ma (MSWD = 2.3; Fig. 8e inset), and the remaining rim analysis yielded a concordant $^{207}Pb/^{206}Pb$ date of 1788 ± 12 Ma (Fig. 8e inset). CL images suggest that the five analyses at c. 1860 Ma represent parts of grains or rims that show relict 'ghost' concentric zonation patterns, or that were moderately metamict. These analyses probably record partially reset ages, and are thus regarded as geologically meaningless. The single concordant rim dated at c. 1790 Ma may represent the true age of the metamorphic overprint, either as a rare, newly grown metamorphic zircon rim, or, most likely, as a completely reset c. 1930 Ma rim or igneous detrital grain margin.

### GSWA 187403: tourmaline-bearing orthoquartzite

This sample yielded abundant anhedral to subhedral zircons, which are clear and colourless to dark brown and turbid. The crystals are up to 350 μm long, and equant to elongate, with aspect ratios up to 3:1. Their abraided and pitted surfaces and the high degree of rounding are consistent with mechanical abrasion during sedimentary transport. Concentric zoning in most zircon cores is truncated by zircon rims that are dark and structureless in CL (Fig. 7d).

Sixty-four analyses were obtained from 60 zircons; results are referenced in Appendix 1. Most analyses are concordant or only slightly discordant. Three analyses are >5% discordant, and have undergone radiogenic Pb loss. The dates from these three analyses are unreliable, and are not considered geologically significant.

Fifty-seven analyses of 54 concentrically-zoned detrital zircon cores yield $^{207}Pb/^{206}Pb$ dates of 3212–2286 Ma (Fig. 8g), and define several age components (Fig. 8h). The youngest core analysed indicates a date of 2286 ± 13 Ma, interpreted as a maximum age for deposition of the protolith of this metasedimentary rock (Table 1). However, a more conservative estimate of the maximum depositional age can be based on the weighted mean date of 2327 ± 14 Ma (MSWD = 0.05) for the next two youngest analyses.

Four analyses of zircon rims yield a weighted mean $^{207}Pb/^{206}Pb$ date of 1772 ± 6 Ma (MSWD = 0.89; Fig. 8g inset). These analyses indicate high uranium content (1070–1530 ppm) and low Th/U ratios (0.004 – 0.007), characteristics typical of zircon grown during a

metamorphic event. The date of 1772 Ma for the zircon rims is therefore interpreted as the age of metamorphism, and also provides a minimum age for deposition of the precursor sediment.

### GSWA 185942: pelitic diatexite

This sample yielded abundant subhedral to euhedral zircon, generally 100–300 µm long, and rounded to elongate with aspect ratios commonly 3:1 and in some cases up to 6:1. Most grains display concentric growth zoning which, in many crystals, is truncated at grain edges by homogeneous rims that are dark in CL images (Fig. 9). A small number of grains are completely dark in CL images, with little indication of internal structure (Fig. 9).

Eighty-two analyses were obtained from 76 zircons; results are referenced in Appendix 1. Most analyses are concordant, although four analyses >5% discordant indicate loss of radiogenic Pb, and 11 analyses are interpreted as mixtures between core and rim material. The dates from these 15 analyses are unreliable, and are not considered geologically significant.

The remaining 67 analyses indicate $^{207}Pb/^{206}Pb$ dates of 3222–1982 Ma (Fig. 10a), and include several age components (Fig. 10b). The two youngest detrital core analyses yield a weighted mean date of 2083 ± 7 Ma (MSWD = 0.02; Fig. 10a, inset), interpreted as a maximum age of deposition for the pelitic protolith (Table 1). A more conservative estimate is given by the weighted mean $^{207}Pb/^{206}Pb$ date of 2121 ± 5 Ma (MSWD = 0.67) for the next three youngest analyses. Seven analyses of zircon rims yield a weighted mean date of 1997 ± 10 Ma (MSWD = 3.3; Fig. 10a inset). These analyses indicate moderate to low Th/U ratios (0.01 – 0.27), and are interpreted to represent metamorphic zircon. The date of 1997 Ma is interpreted as the age of high-grade metamorphism and migmatization.

### NP20: fine-grained quartzite (Kinny et al., 2004)

Quartzite sample NP20 (Kinny et al., 2004) yielded a diverse population of subrounded detrital zircon grains, several of which are overgrown by thin metamorphic rims. Some grains showed a high degree of abrasion, indicative of mechanical transport (see Fig. 2 in Kinny et al., 2004).

Thirty-five analyses were obtained from 35 grains, including three analyses of two zircon rims. Four analyses are >5% discordant, indicating radiogenic Pb loss. The remaining 361 analyses indicate $^{207}Pb/^{206}Pb$ dates of 2954–1921 Ma (Fig. 10a). Detrital cores yielded $^{207}Pb/^{206}Pb$ dates of 2590–2450 Ma (Fig. 10c; fig. 3a in Kinny et al., 2004), and define several age components (Fig. 10d). The two youngest analyses indicate dates of 2290–2270 Ma (Table 1), interpreted as the maximum age of deposition for the sandstone protolith. Three analyses of zircon rims indicate low Th/U (0.02 – 0.06) and yield a

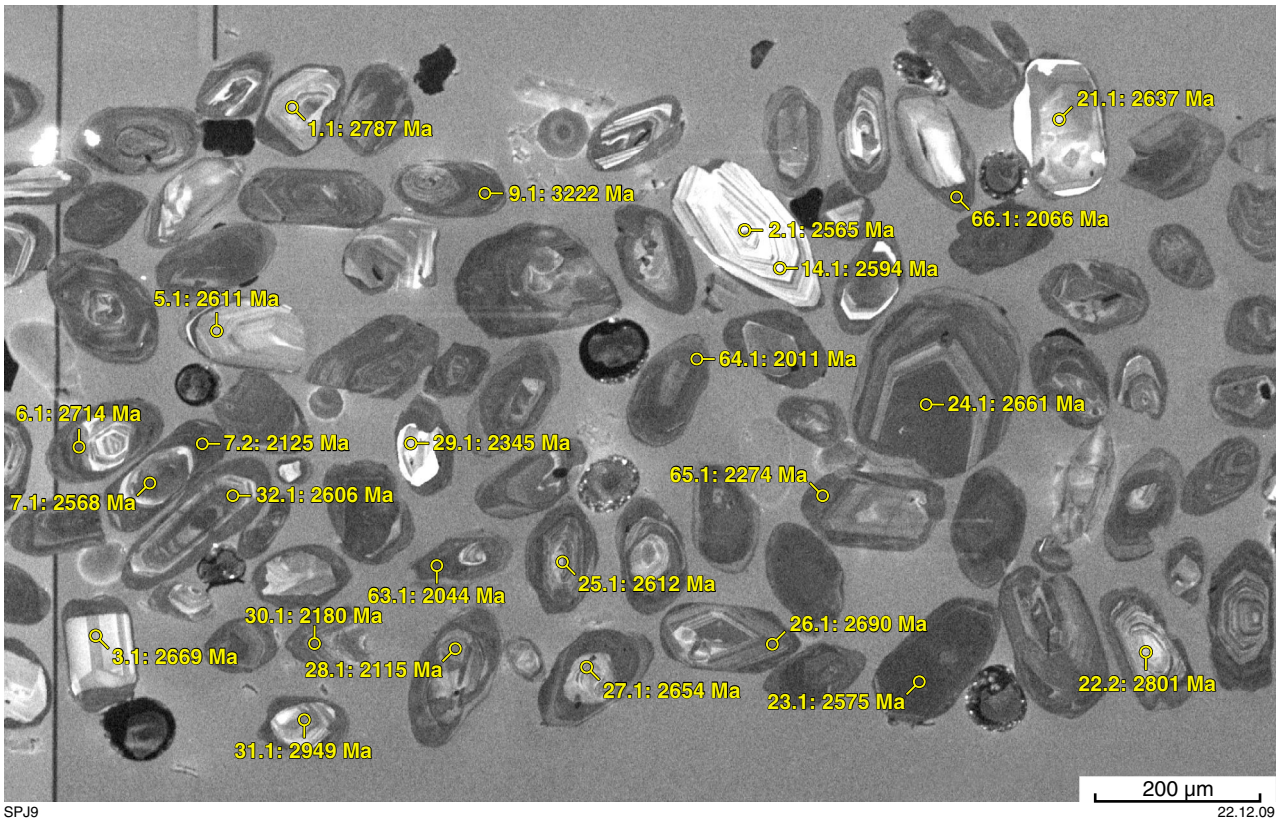


**Figure 9. Cathodoluminescence (CL) images of representative zircon dated from the pelitic diatexite sample (GSWA 185942) from Paradise Well on Glenburgh. The location of SHRIMP analysis sites are shown along with the analysis number and $^{207}Pb/^{206}Pb$ age. SHRIMP U–Pb data for these samples are tabulated in Appendix 1.**

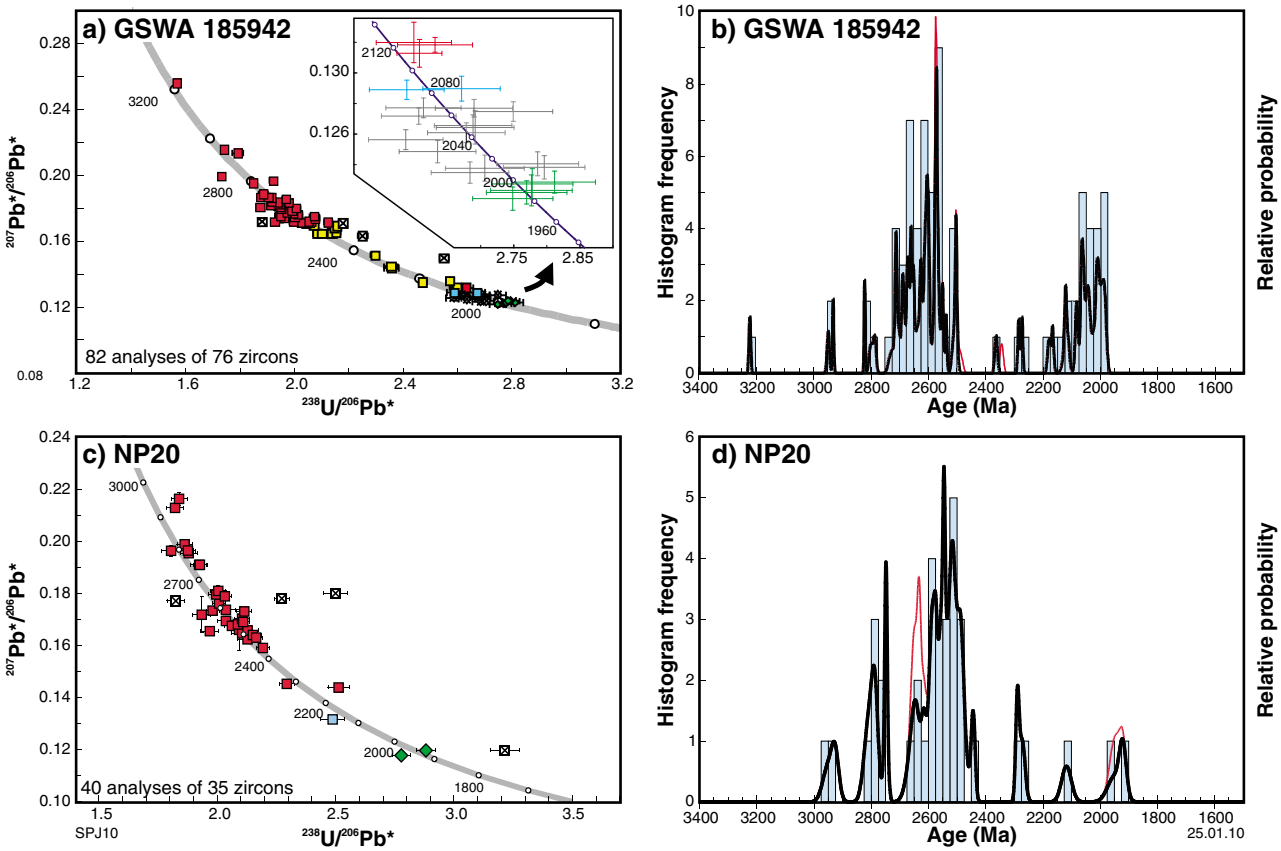


**Figure 10. U–Pb concordia diagrams and probability density distribution plots for detrital and metamorphic zircon from the pelitic diatexite sample GSWA 185942 from Paradise Well on Glenburgh (a–b) and the Mumba Psammite pelitic schist sample NP20 (c–d) dated by Kinny et al. (2004). Red squares and crosses (inset) are for detrital zircon, blue squares and blue crosses (inset) are for the youngest detrital zircon in the metasediment, green diamonds and crosses (inset) are for metamorphic zircon. Analyses shown with an 'x' or as a grey cross (inset) are mixed ages, whilst zircon >5% discordant are shown in the main plots as squares with crosses. U–Pb SHRIMP data for these samples are tabulated in Appendix 1. The black curve in the probability density distribution plots represents the data <5% discordant, whereas the red curve is for all data regardless of discordance. Histogram boxes binned at 25 m.y.**

mean $^{207}Pb/^{206}Pb$ date of 1934 ± 43 Ma (MSWD = 1.2), interpreted as the age of metamorphism.

# Camel Hills Metamorphics

## Quartpot Pelite

### *GSWA 142910: retrogressed pelitic diatexite*

Zircons from this sample have a wide range of morphologies, but most are brown to dark brown, generally 150–600 µm long and euhedral, but with rounded terminations suggesting abrasion during sedimentary transport. Most grains possess concentric zoning (Fig. 11a–c) that are commonly truncated by thin (5–30 µm), overgrowths that are dark in CL images (Fig. 11a,b).

Thirty-four analyses were obtained from 31 zircons, including two analyses of zircon rims; results referenced in Appendix 1. In addition, 23 analyses of 15 zircons were reported by Occhipinti (2004; data tabulated in Appendix 1). In total, 57 analyses were obtained from 45 zircons, of which 13 analyses were performed on zircon rims. Most analyses are concordant, although 17 analyses are >5% discordant, indicating radiogenic Pb loss. One rim analysis (analysis S3.3; Occhipinti, 2004; Appendix 1) is interpreted as a mixture between core and rim. The dates from these 18 analyses are unreliable, and are not considered geologically significant.

Of the remaining 39 analyses, 28 are of detrital cores and 11 are of zircon rims. The 28 detrital cores yield $^{207}Pb/^{206}Pb$ dates of 2892–2020 Ma (Fig. 12a,b), including nine dates between 2260 and 2150 Ma, and 18 dates between 2095 and 2020 Ma (Fig. 13a).

Over 64% of the detrital cores have a narrow range of dates between 2095 and 2020 Ma. The individual analyses are dispersed beyond analytical precision, suggesting the presence of more than one age component or that this group represents detrital zircon grains that have lost radiogenic Pb during metamorphism (Fig. 13a). However, the absence of a significant correlation between calculated zircon density (reflecting degree of metamictization; Murakami et al., 1991; Appendix 2) and age (Fig. 13b), or uranium content and age (Fig. 13c) suggests that these

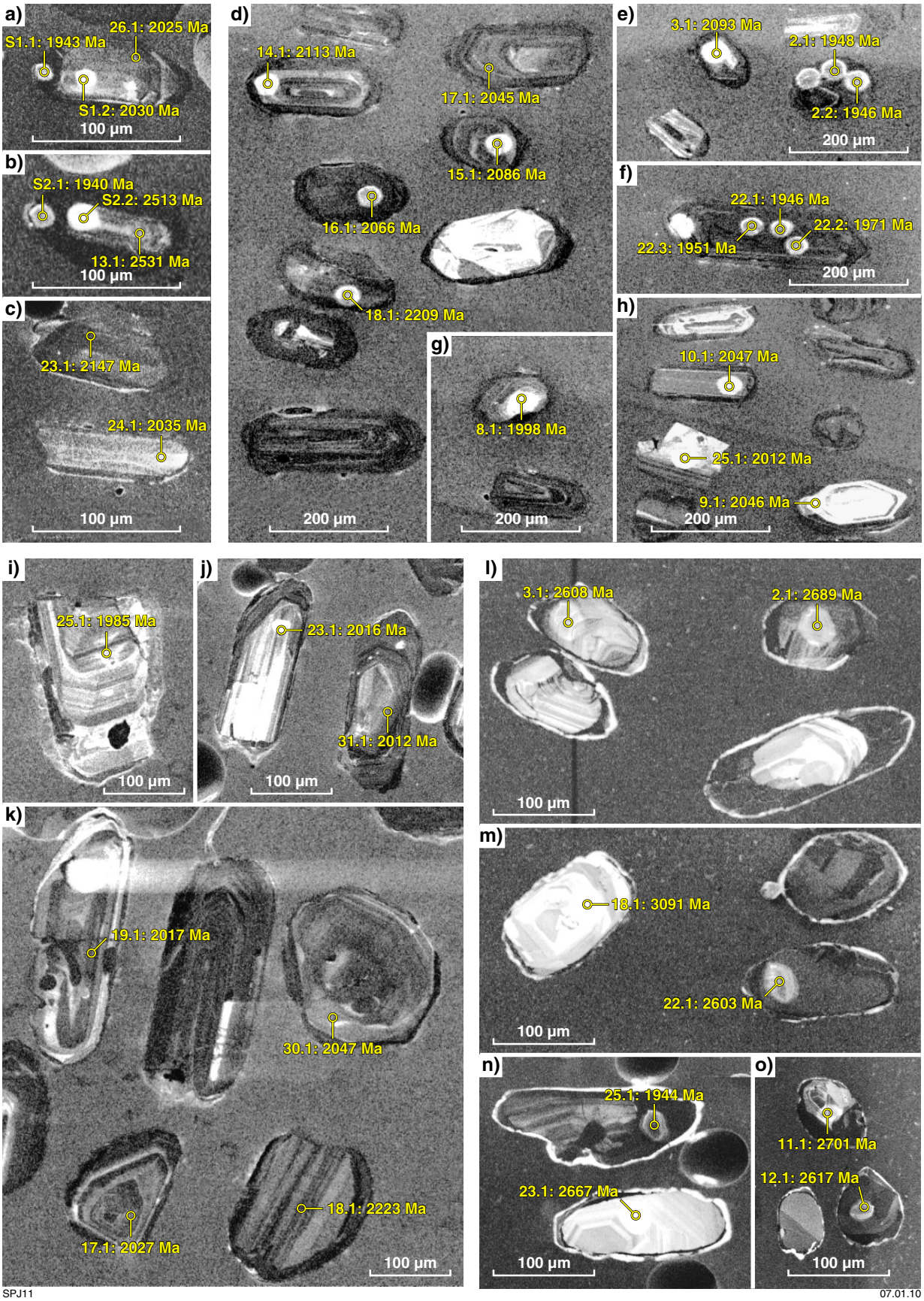


**Figure 11. Cathodoluminescence (CL) images of representative zircon dated from the Camel Hills Metamorphics: a–c) GSWA 143910; d–h) GSWA 142905; i–k) GSWA 168944; l–o) GSWA 142908. The location of SHRIMP analysis sites are shown along with the analysis number and $^{207}Pb/^{206}Pb$ age. SHRIMP U–Pb data for these samples are tabulated in Appendix 1.**

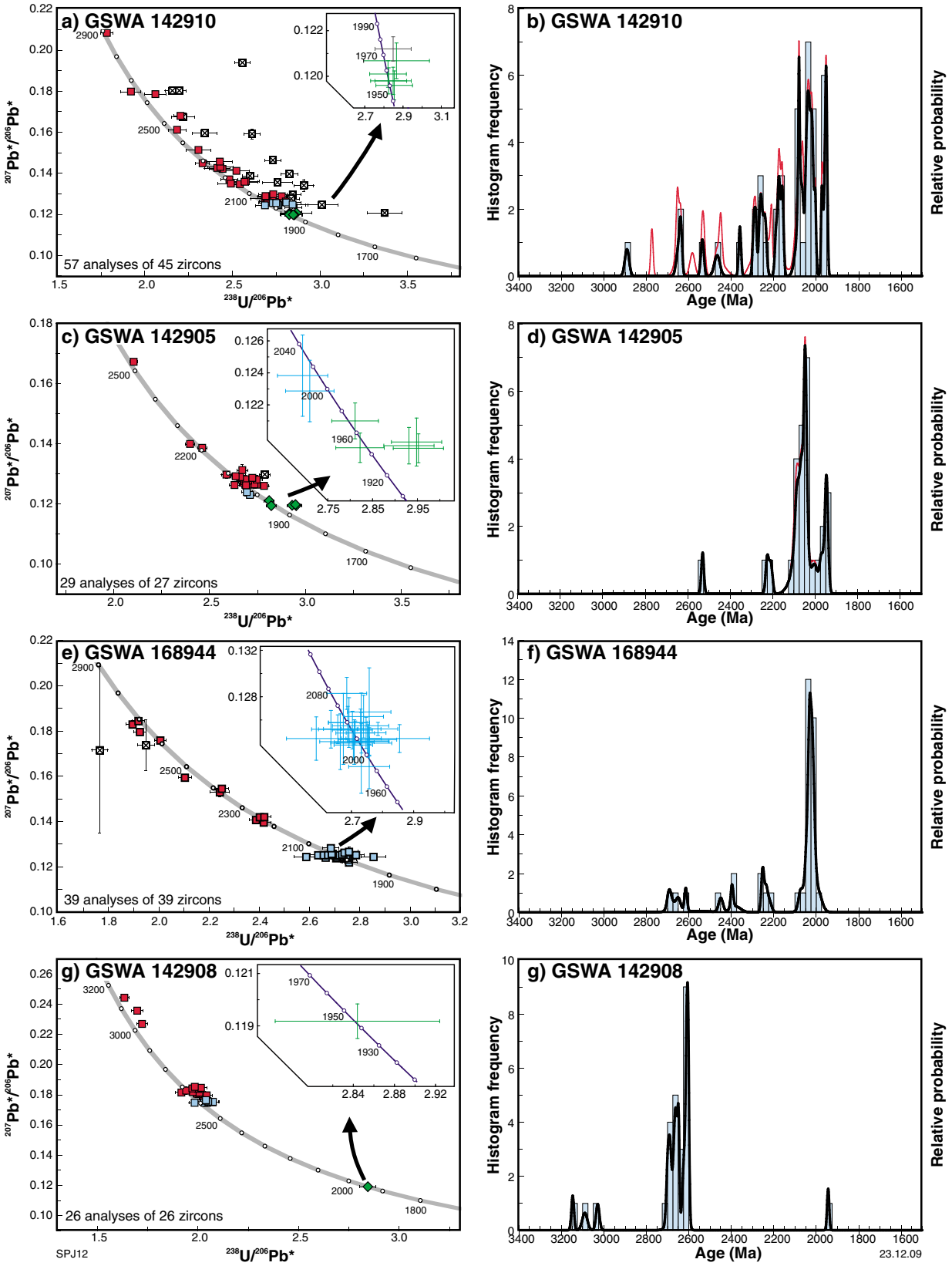


**Figure 12.** U–Pb concordia diagrams and probability density distribution plots for detrital and metamorphic zircon from the Quartpot Pelite (a–f) and Petter Calc-silicate (g–h). Red squares are for detrital zircon, blue squares and blue crosses (inset) are for the youngest detrital zircon in the metasediment and green diamonds and crosses (inset) are for metamorphic zircon. Zircon >5% discordant are shown as squares with crosses. U–Pb SHRIMP data for these samples are tabulated in Appendix 1. The black curve in the probability density distribution plots represents the data that is <5% discordant, whereas the red curve is for all data regardless of discordance. Histogram boxes binned at 25 m.y.

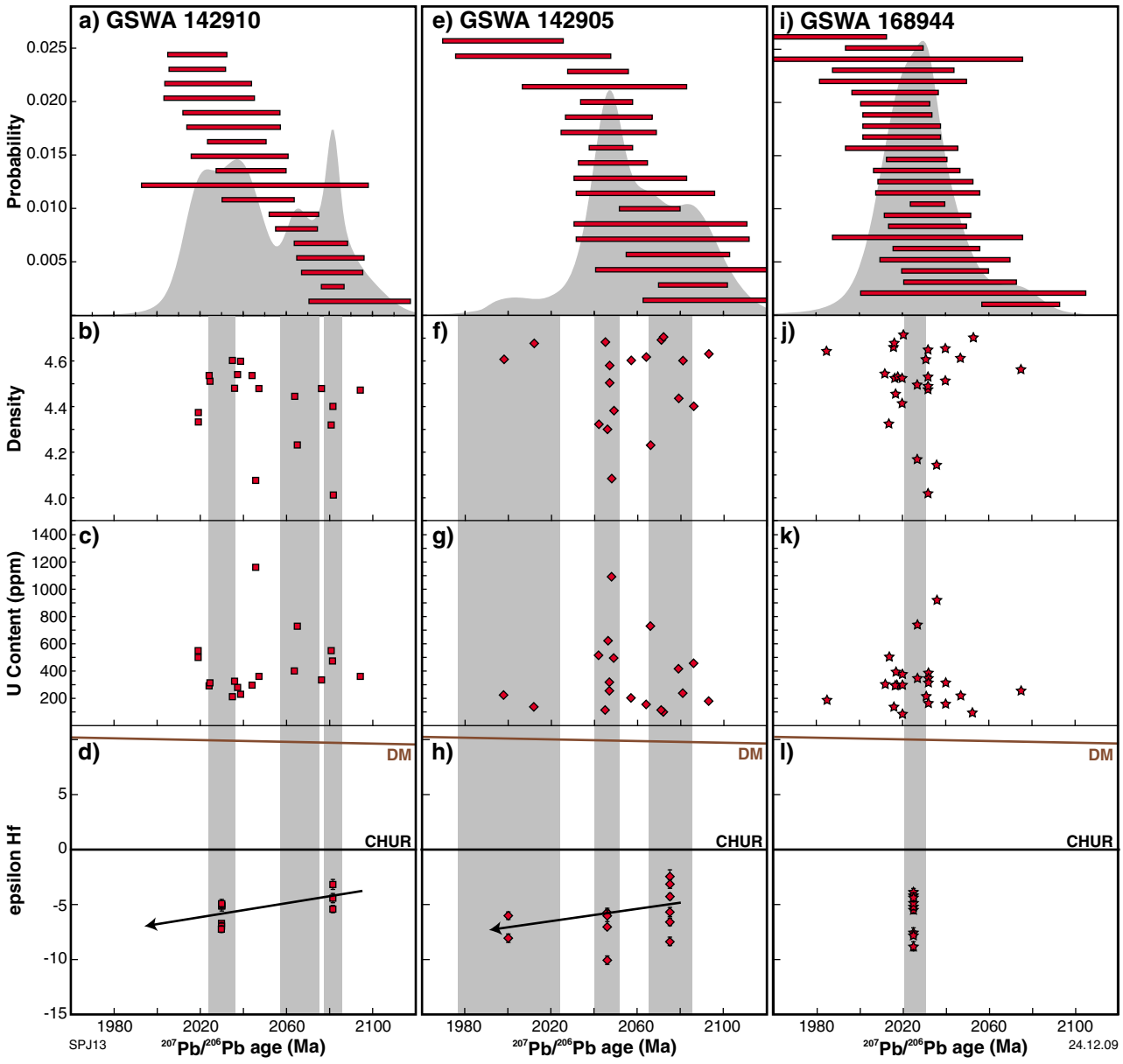


**Figure 13.** U–Pb age data, and in situ Lu–Hf isotopic data, for 2080–2000 Ma-aged zircon samples from the Quartpot Pelite: a–c) GSWA 142910; e–h) GSWA 142905; i–l) GSWA 168944. A series of age plots (a, e, i) show the age range of zircons from each sample within the 2080–2000 Ma population, with individual ages are shown at the 2ε level. A probability density distribution ( lled grey curve) is also shown to illustrate the possible age populations present within each sample. Graphs plotting the age of the zircon verses its density (Murakami et al., 1991; b, f and j), and zircon age verses uranium content (c, g and k), each show a lack of correlation between the two parameters, illustrating that these grains are not variably metamict. Finally, there are a series of graphs which show the εHf value for selected zircon grains from the 2080–2000 Ma-aged populations, with εHf values calculated from the pooled ages (d, h and l). Note for samples GSWA 142910 and GSWA 142905, these values become more evolved (i.e. they move toward increasingly negative values with decreasing age), re ecting increased contamination from older continental crust. The grey shaded elds in b–d, f–h, j–l) represent the individual age populations obtained for each sample using the 'unmix' algorithm in Isoplot/Ex v. 3.0 (Ludwig, 2001). The uranium content and density values for each zircon are tabulated in Appendix 2, and the Lu–Hf isotope analyses are tabulated in Appendix 4.

dates are unlikely to represent variable loss of radiogenic Pb during high-grade metamorphism. The mixture-modelling algorithm of Sambridge and Compston (1994), as implemented in Isoplot/Ex v. 3.0 (Ludwig, 2001), suggests the presence of three distinct age populations at 2082 ± 4 Ma, 2065 ± 9 Ma and 2031 ± 6 Ma, the youngest of which provides a maximum age for deposition of the sedimentary precursor (Table 1). These results suggest that the protolith to this metasediment was derived from a source region with a heterogeneous age distribution, possibly reflecting magmatism between c. 2080 Ma and 2030 Ma.

Five of the 11 zircon rims indicate $^{207}Pb/^{206}Pb$ dates of 2222–2046 Ma, whereas the remaining six yield dates of 1974–1950 Ma (Appendix 1). The older five analyses indicate Th/U ratios of 0.01 – 0.41 and the dates are dispersed beyond analytical precision, suggesting that these analyses represent detrital metamorphic components within the sample, or igneous zircon with variable Th/U contents that have grown around older inherited cores. Of the six younger analyses, the oldest (S12.1; Occhipinti, 2004) yielded an age of 1974 Ma and is significantly older than the other five. The location of the analysis within the grain is not known, so it is possible that this analysis represents a mixture between core and rim material. The remaining five analyses yield a weighted mean $^{207}Pb/^{206}Pb$ date of 1955 ± 7 Ma (MSWD = 1.4; Fig. 12a). These rims have low Th/U ratios of 0.01 – 0.10 and are interpreted to have grown during high-grade metamorphism. The date of 1955 Ma is therefore interpreted as the age of metamorphism.

### GSWA 142905: retrogressed pelitic diatexite

Zircons from this sample are generally subhedral to rounded, light pink-brown, straw-brown, dark brown, or black, and typically 150 μm long, with some grains up to 400 μm long. Surface pitting, indicative of sedimentary transport, is evident in many grains. The majority of crystals possess concentric zoning typical of igneous zircon (Fig. 11d–h), although one grain contains a small core truncated by a 10–30 μm thick, structureless, rim that is dark in CL (Fig. 11e).

Twenty-nine analyses were obtained from 26 zircons, including two analyses of a single structureless zircon rim (analyses 2.1 and 2.2); results are referenced in Appendix 1. Two analyses >5% discordant may have lost radiogenic Pb and are not discussed further. The 25 detrital cores yield dates of 2530–1946 Ma (Fig. 12c,d), including twenty analyses with dates of 2095–1998 Ma (Figs 12d, 13e).

Similar to sample GSWA 142910, the majority of detrital grains yield dates in a very narrow time frame and dispersed beyond analytical precision. The absence of a significant correlation between calculated zircon density (reflecting degree of metamictization; Appendix 2; Murakami et al., 1991) and age (Fig. 13f), or uranium content and age (Fig. 13g), suggests that the 2095–1998 Ma dates are unlikely to represent variable loss of radiogenic Pb during high-grade metamorphism. These analyses are therefore interpreted to represent detrital zircons as young as 1998 Ma. Using the mixture-modelling algorithm of Sambridge and Compston (1994), as implemented in Isoplot/Ex v. 3.0 (Ludwig, 2001), three distinct age components can be identified at 2076 ± 10 Ma, 2048 ± 6 Ma, and 2001 ± 26 Ma (Fig. 13e). Therefore, this metasedimentary rock was derived from a source region where there was active magmatism between c. 2080 Ma and 2000 Ma, with the maximum age for deposition of the sedimentary precursor provided by the youngest age component at 2001 ± 26 Ma (Table 1).

Two analyses of the single zircon rim yield dates of c. 1950 Ma and indicate low Th/U ratios of 0.02 and 0.03 (Appendix 1). Three analyses of the centre of a concentrically zoned grain (analyses 22.1, 22.2 and 22.3; Fig. 11f) yield similar dates with equally low Th/U ratios (0.01 – 0.07). An analysis of zircon crystallinity (Appendix 2; Murakami et al., 1991) indicates that the grain is not metamict. Considering morphology and internal zonation, it is difficult to interpret this grain as metamorphic in origin; however, considering the high uranium content, low Th/U ratio, non-metamict crystalline structure, and young apparent age, it is equally difficult to advocate that this is a detrital igneous grain that has lost all of its radiogenic lead during a metamorphic event at c. 1950 Ma. It is possible that this grain grew directly from the partial melt, as described for similar grains by Schaltegger et al. (1999) and Möller et al. (2002). Together, these five analyses provide a weighted mean $^{207}Pb/^{206}Pb$ date of 1952 ± 14 Ma (MSWD = 1.8; Fig. 12c), interpreted to record the timing of high-grade metamorphism and migmatization.

### GSWA 168944: psammitic schist

The zircons in this sample are colourless to yellow-brown and dark-brown, generally elongate and 60–350 μm long, and are subrounded or irregular in shape. Surface pitting, consistent with sedimentary transport, is evident on many grains. Most grains possess fine concentric zoning characteristic of igneous growth (Fig. 11i–k). In some of these grains, zoning is truncated or overgrown by 5–30 μm thick zircon rims that are either structureless or display very weak concentric zoning in Cl images (Fig. 11i–k). Some rims also show evidence of pitting and abrasion, suggesting that they grew prior to sedimentary deposition.

Thirty-one analyses were obtained from 31 detrital zircon cores, and Occhipinti (2004) reported eight additional analyses (Appendix 1), three of which were of structureless zircon rims. In total, 36 cores and 3 rims were analysed, with all analyses less than 5% discordant. Three analyses (Appendix 1) indicate high common Pb contents and are not considered geologically significant. The remaining 34 analyses of detrital cores yield $^{207}Pb/^{206}Pb$ dates of 2694–1985 Ma (Fig. 12e), including several age components (Fig. 12f). The three zircon rims analysed by Occhipinti (2004) yield similar dates (2594–2036 Ma), and indicate moderate Th/U ratios of 0.13–0.56 (Appendix 1), suggesting they could be of igneous origin.

The majority of zircon cores (23 analyses) yield dates of 2075–1985 Ma (Fig. 13i). The youngest analysis indicates

an age of 1985 ± 14 Ma, and is from a large, irregular grain fragment (analysis 25.1; Fig. 11i) that appears to be of detrital origin. Analysis of the crystallinity of this youngest grain (Appendix 2; Murakami et al., 1991) shows that it is highly ordered and unlikely to have undergone any significant Pb loss during high-grade metamorphism. The youngest 22 analyses yield a weighted mean $^{207}Pb/^{206}Pb$ age of 2027 ± 4 Ma (MSWD = 1.17; Fig. 13i), interpreted as a conservative maximum age for deposition of the sedimentary precursor (Table 1).

## Petter Calc-silicate

### *GSWA 142908: calc-silicate gneiss*

Zircons from this sample have a wide range of morphologies. Most crystals are light yellow-brown to dark-brown in colour, generally 300–600 μm in length, and subrounded or irregular in shape. Many grains are fractured, and most have pitted and abraded surfaces consistent with sedimentary transport. Most grains exhibit fine oscillatory zoning, although a few show coarse sector zoning (Fig. 11l–o). Both textures are common in igneous zircon (e.g. Corfu et al., 2003). In most grains, this zoning is truncated by structureless rims of variable thickness (5–50 μm) that are dark in Cl images.

Twenty-six analyses were obtained from 26 zircons, including 25 analyses of zircon cores and one analysis of a zircon rim; results are referenced in Appendix 1. All analyses are <5% discordant. The 25 core analyses yield $^{207}Pb/^{206}Pb$ dates of 3148–2603 Ma (Fig. 12g), and include several age components (Fig. 12h). The youngest analysis indicates a date of c. 2600 Ma, and forms part of a group of nine analyses that yield a weighted mean date of 2608 ± 4 Ma (MSWD = 1.2), interpreted as a maximum age of deposition of the sedimentary protolith (Table 1). Analysis of the zircon rim indicates a moderate Th/U ratio of 0.3, and a $^{207}Pb/^{206}Pb$ date of 1944 ± 5 Ma (1σ), interpreted to approximate the age of high-grade metamorphism.

# In situ U–Pb geochronology of monazite and zircon

Pelitic schists from the southern and central belts of the Mumba Psammite were collected to investigate the growth of accessory phases such as monazite and, where present, zircon (Fig. 1). To retain as much textural information as possible, the accessory phases were analysed in situ by SIMS using the SHRIMP II ion microprobe. Description of analytical techniques and U–Th–Pb isotope data tables are provided in Appendix 3. All three pelitic schist samples showed petrographic evidence of metamorphism in the amphibolite facies with the growth of medium- to high-grade metamorphic porphyroblasts such as garnet and sillimanite, although they have since been extensively retrogressed in the greenschist facies. The samples also contain minor amounts of accessory phosphate minerals (apatite, monazite, and xenotime), zircon, rutile, Fe–Ti oxide minerals, and barite.

### *GSWA 164369: garnet–sericite schist*

This sample is a sericite–chlorite–muscovite–quartz (–garnet) schist from the southern belt of the Mumba Psammite (Fig. 1). The sample was obtained from a similar part of the sedimentary package as GSWA 184161, 183275, and GSWA 168713, the latter also collected for monazite dating. The present sample is a fine-grained porphyroblastic schist that contained moderately abundant, mm-sized, partially retrogressed, garnet porphyroblasts. It probably comprised an original peak assemblage of muscovite–biotite–garnet–quartz(–sillimanite). Most monazite crystals in this sample have undergone intense alteration, although apparently unaltered monazite is preserved as minute inclusions (<15 μm) within some variably retrogressed garnet porphyroblasts (Fig. 14b). Monazite also occurs within the matrix as irregular grains (up to 400 μm in diameter) surrounded by areas of intense alteration (Fig. 14a–c). Alteration rims typically comprise an intergrowth of Fe-oxide minerals and REE-, yttrium- and thorium-rich minerals (Fig. 14a–c). Due to the extensive greenschist facies retrograde alteration, it is difficult to directly link monazite growth with any structural fabrics in this sample.

Five monazite grains were selected for analysis. A1 and D1 are large (100–200 μm long) grains existing within the matrix, which have undergone variable retrogression to Fe-oxide and REE-bearing mineral phases (Fig. 14c). D2 and D3 are small (15–20 μm diameter), relatively unaltered grains that occur within garnet porphyroblasts (Fig. 14b), and G1 is a very large (400 μm diameter) grain that occurs at the margin of a variably retrogressed garnet porphyroblast (Fig. 14a, d–e). Element mapping of all monazite grains reveals little variation in lanthanum, although there is a strong variable distribution of yttrium and thorium in the very large monazite grain G1 (Fig. 14d–e). This grain contains a central core region with a uniformly high yttrium content and vague sector zoning defined by variations in thorium content. The sector-zoned core region is truncated along cuspate surfaces by a thick, uniform, yttrium-poor and thorium-variable rim (Fig. 14d–e). The cuspate nature of the core–rim interface suggests that the rim represents recrystallization of the original monazite grain in situ, rather than overgrowth of new monazite on an older core. The four other monazite grains revealed no significant variation in lanthanum, thorium or yttrium content, and no zoning or core–rim relationships.

A total of 38 analyses were conducted (Appendix 3). Five analyses, including that from grain D2, were disregarded because of discordance (>5%), instrument instability, or elevated common Pb. The remaining 33 analyses yield $^{207}Pb/^{206}Pb$ ages of 2130–1950 Ma (Fig. 14f). The data appear to show two significant episodes of monazite growth (Fig. 14f), at 2130–2080 Ma and 2010–1950 Ma, with considerable age variation within each group.

Although the outer margin of grain D1 has been significantly altered to Fe-oxide and REE-bearing minerals, it yields consistent U–Pb results (Fig. 14c, h). Seven out of eight analyses yield a concordant weighted mean $^{207}Pb/^{206}Pb$ date of 2125 ± 9 Ma (MSWD = 2.6; Fig. 14g) with the youngest analysis at c. 1990 Ma

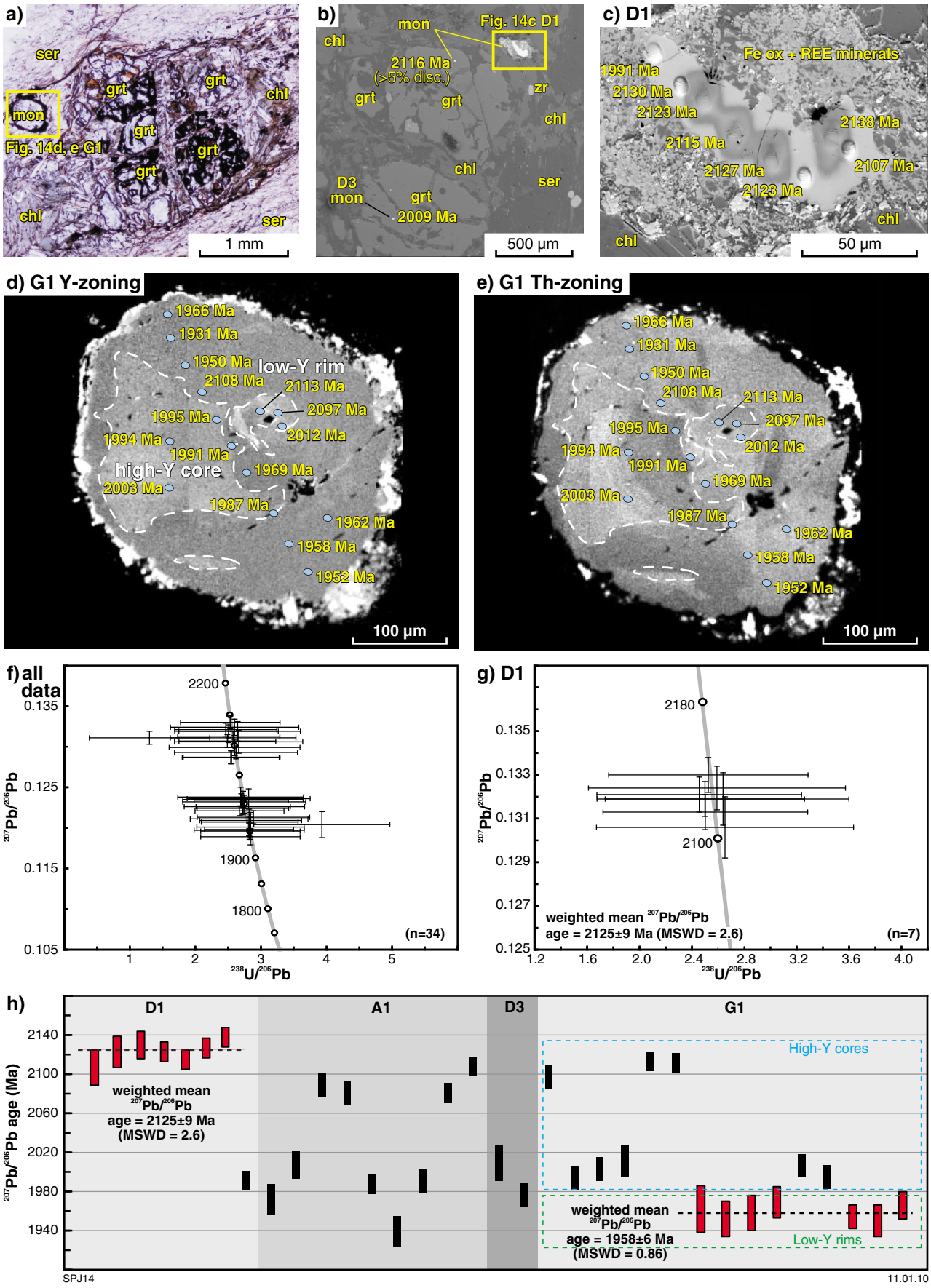
a)
ser
grt
grt
chl
mon
grt
Fig. 14d, e G1
grt
grt
chl
ser
1 mm
b)
mon
Fig. 14c D1
chl
2116 Ma
(>5% disc.)
grt
grt
zr
chl
chl
ser
D3
mon
grt
2009 Ma
500 µm
c) D1
Fe ox + REE minerals
1991 Ma
2130 Ma
2123 Ma
2138 Ma
2115 Ma
2127 Ma
2107 Ma
2123 Ma
chl
chl
50 µm
d) G1 Y-zoning
1966 Ma
1931 Ma
1950 Ma
low-Y rim
2108 Ma
2113 Ma
2097 Ma
1995 Ma
2012 Ma
1994 Ma
1991 Ma
high-Y core
1969 Ma
2003 Ma
1987 Ma
1962 Ma
1958 Ma
1952 Ma
100 µm
e) G1 Th-zoning
1966 Ma
1931 Ma
1950 Ma
2108 Ma
2113 Ma
2097 Ma
1995 Ma
2012 Ma
1994 Ma
1991 Ma
1969 Ma
2003 Ma
1987 Ma
1962 Ma
1958 Ma
1952 Ma
100 µm
f) all data
2200
1900
1800
(n=34)
207Pb/206Pb
238U/206Pb
g) D1
2180
2100
weighted mean 207Pb/206Pb
age = 2125±9 Ma (MSWD = 2.6)
(n=7)
207Pb/206Pb
238U/206Pb
h)
D1
A1
D3
G1
High-Y cores
weighted mean
207Pb/206Pb
age = 2125±9 Ma
(MSWD = 2.6)
weighted mean
207Pb/206Pb
age = 1958±6 Ma
(MSWD = 0.86)
Low-Y rims
207Pb/206Pb age (Ma)
SPJ14
11.01.10

most likely recording dissolution and reprecipitation of monazite at the grain margin during subsequent medium- to high-grade metamorphism or greenschist facies alteration. This c. 2125 Ma date is similar to the oldest dates obtained from the complexly zoned grain G1. The high-yttrium core regions of grain G1 yield dates between 2113 Ma and 1991 Ma, whereas the yttrium-poor rim has a much more uniform age distribution, with all seven analyses providing a concordant weighted mean $^{207}Pb/^{206}Pb$ date of 1958 ± 6 Ma (MSWD = 0.86; Fig. 14h). The heterogeneous distribution of $^{207}Pb/^{206}Pb$ dates in the monazite core is most likely due to variable Pb loss during the recrystallization event at c. 1960 Ma. Although highly altered, and therefore texturally similar to grain D1, grain A1 yields widely dispersed $^{207}Pb/^{206}Pb$ dates between 2110 and 1940 Ma, with no apparent correlation between individual dates and grain morphology. However, the oldest and youngest dates are within uncertainty (1σ) of those yielded by grains D1 and G1. The small unaltered monazite grains (D2 and D3) that occur within the garnet porphyroblasts have also been affected by variable dissolution and reprecipitation. Grain D2 yields two dates that are >5% discordant, while the two analyses of grain D3 yield dates of c. 2010 Ma and c. 1975 Ma.

In situ analysis of monazite was complemented by analyses of the abundant zircon crystals present in this sample. The zircons are subhedral to subrounded, and typically ~50 μm in size with aspect ratios of 1:1. All zircons are dark and featureless in CL images owing to their high uranium contents (Appendix 3).

Twenty-four analyses were obtained from eight grains, of which four analyses are >5% discordant and are considered unreliable (Appendix 3). The remaining 20 analyses yield $^{207}Pb/^{206}Pb$ dates of 2130–1860 Ma (Fig. 15a) and are variable within, as well as between, grains (Fig. 15c). Nearly all analyses indicate low Th/U ratios (0.01 – 0.32) which, along with their weak sector-zoned internal textures, is consistent with a metamorphic origin (Corfu et al., 2003). Eleven analyses of five grains yield a weighted mean $^{207}Pb/^{206}Pb$ date of 1959 ± 8 Ma (MSWD = 0.98; Fig. 15b, c), which is within error of the 1958 ± 6 Ma date obtained from the low-yttrium rim on monazite grain G1 (Fig. 14h). Two older results, with a weighted mean $^{207}Pb/^{206}Pb$ date of 2126 ± 10 Ma (MSWD = 0.16; Fig. 15c), are equivalent in age to monazite grain D1 and also to the older analyses within most other monazites in this sample. Several results intermediate to these two end members (Fig. 15c) are interpreted to represent parts of the older metamorphic zircon population that have either undergone variable Pb loss during the c. 1960 Ma metamorphic event, or represent mixed ages between different parts of the metamorphic zircon grains. Additionally, grain I1 yields three much younger $^{207}Pb/^{206}Pb$ dates, between 1900 Ma and 1850 Ma, which are interpreted as additional Pb loss subsequent to the c. 1960 Ma event, presumably during the low-grade greenschist facies overprint.

Although the monazites in this sample have been subjected to intense retrograde dissolution and reprecipitation, the presence of relict cores and recrystallized rims, and the preservation of uniform dates within some grains, allows an interpretation to be made. Furthermore, the monazite dates are consistent with those obtained from zircons in this sample. The oldest monazite dates within all grains are consistent and within error of the concordant weighted mean $^{207}Pb/^{206}Pb$ date provided by grain D1 at c. 2125 Ma. This result is indistinguishable from that obtained from two CL-dark, structureless, low Th/U metamorphic zircon grains within this sample, and from several detrital metamorphic zircon components within sample GSWA 185942. This consistency between zircon and monazite results make it unlikely that these minerals are inherited detrital components, but rather that they grew in situ during a metamorphic event, the grade of which is unknown. The date of c. 2125 Ma also provides a minimum age for deposition of the sedimentary precursor. Partial recrystallization of monazite, and variable Pb loss from zircon, possibly accompanied by new metamorphic zircon growth, occurred at c. 1960 Ma. Variable dissolution and reprecipitation of monazite, and partial Pb loss in zircon, also occurred during low-grade greenschist facies alteration sometime after c. 1860 Ma, the age of the youngest zircon analysis.

**Figure 14. (facing page) In situ monazite age data from a garnet-bearing schist of the Mumba Psammite (GSWA 164369): a) photomicrograph in plane polarized light of garnet–sericite schist, showing location of large monazite (mon) grain G1 next to a variably retrogressed garnet (grt) porphyroblast, set within a matrix of sericite (ser) and chlorite (chl); b) SEM image showing location of monazite grains D1 and D3 within or close to garnet porphyroblasts, and set within a matrix of sericite and chlorite (chl) with accessory zircon (zr); c) close-up SEM image of grain D1, showing location of SHRIMP analytical pits and corresponding $^{207}Pb/^{206}Pb$ ages. Note that the grain is variably altered to Fe oxide minerals (Fe ox) and rare earth element (REE)-bearing mineral phases; d and e) SEM element maps for yttrium and thorium of complexly zoned monazite grain G1. The element maps show variable concentrations of both yttrium and thorium, illustrating a concentrically zoned core that is variably recrystallized around the margin. Location of SHRIMP analytical pits and corresponding $^{207}Pb/^{206}Pb$ ages are also shown; f) Tera–Wasserburg U–Pb plot for all of the collected data; g) Tera–Wasserburg U–Pb plot for analyses within grain D1; h) summary diagram showing the age distribution ($^{207}Pb/^{206}Pb$ age at 2σ) within each monazite grain. U–Pb age data for all SHRIMP analytical spots are tabulated in Appendix 3.**

### *GSWA 168713: magnetite–sericite schist*

This quartz–sericite–magnetite schist from the southern belt of the Mumba Psammite (Fig. 1) is from a similar part of the package as GSWA 184161, 183275, and 164369. The sample is a fine-grained schist with magnetite porphyroblasts up to several mm in diameter. The schist contains a crenulation cleavage ($S_2$) associated with the retrogression of the relict prograde assemblages that form an earlier $S_1$ fabric. Although zircon forms a minor proportion of the accessory phases, no zircons were large enough to analyse. Monazite occurs within both the matrix and magnetite porphyroblasts as highly

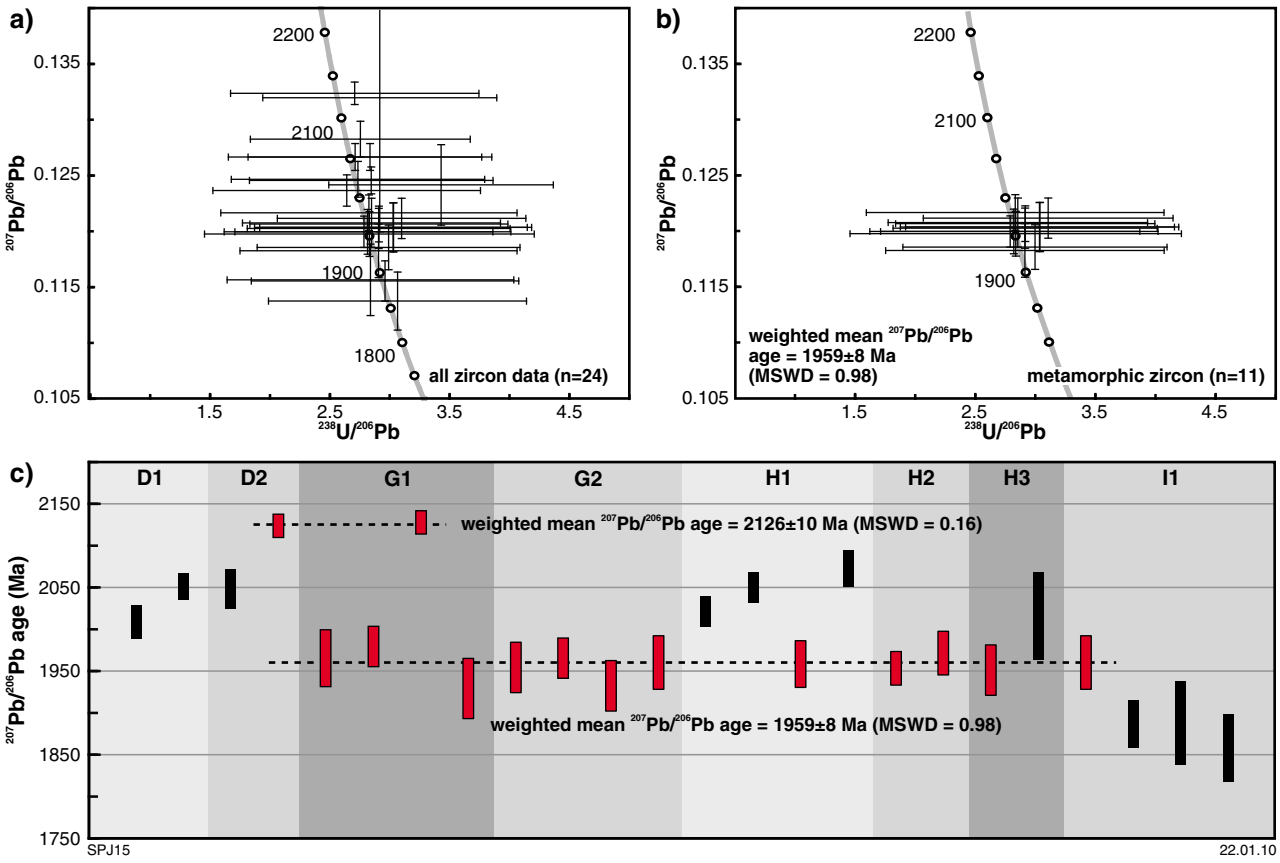


**Figure 15. In situ zircon age data from a garnet-bearing schist of the Mumba Psammite (GSWA 164369): a) Tera–Wasserburg U–Pb plot for all zircon analyses; b) Tera–Wasserburg U–Pb plot for the youngest concordant zircon analyses; c) summary diagram showing the $^{207}Pb/^{206}Pb$ age distribution (each analyses is at the 2σ level) for every analyses within each zircon grain. U–Pb age data for all SHRIMP analytical spots are tabulated in Appendix 3.**

**Figure 16. (facing page) In situ monazite age data from a magnetite schist of the Mumba Psammite (GSWA 168713): a) SEM image showing relict monazite (mon) intergrown with Fe-oxide minerals (Fe ox) that sit within a matrix dominated by metamorphic quartz (qtz); b) close-up SEM image of the intergrown alteration of monazite with Fe-oxide minerals; c) SEM image of partially altered monazite (to Fe-oxide minerals) that sits within a large magnetite (mag) crystal; d) small, subhedral monazite grains K1 and K2, set within metamorphic quartz. The position of the SHRIMP analytical pits and corresponding $^{207}Pb/^{206}Pb$ ages are also shown; e) SEM image of monazite grain I1 with the position of the SHRIMP analytical pits and corresponding $^{207}Pb/^{206}Pb$ ages; f and g) SEM element maps of grain I1 showing that the grain is concentrically zoned with respect to both thorium and yttrium; h) Tera–Wasserburg U–Pb plot for all monazite analyses; i) summary diagram showing the $^{207}Pb/^{206}Pb$ age distribution (each analyses is at the 2σ level) for all analyses within each monazite grain. U–Pb age data for all SHRIMP analytical spots are tabulated in Appendix 3.**

irregular, inclusion-rich residues intergrown with Fe-oxide minerals (Fig. 16a–c). Unaltered monazite, idioblastic to subidioblastic in morphology, is preserved within coarse metamorphic quartz grains (Fig. 16d–e). Owing to intense retrograde overprinting and the isolation of unaltered monazite within large quartz grains, it is difficult to relate prograde monazite growth to the structural fabrics within this sample.

Four unaltered monazite grains were selected for analysis, although one (F1) indicated extremely high levels of common Pb (Appendix 3), and was therefore disregarded. The three remaining grains occur within coarse metamorphic quartz. Grains K1 and K2 are small (20–30 µm diameter) and subidioblastic (Fig. 16d), whereas grain I1 is a much larger (50 µm) and idioblastic (Fig. 16e). Element mapping revealed little variation in lanthanum within any of the grains and no significant zoning in thorium and yttrium within grains K1 and K2. However, simple concentric zoning defined by both thorium and yttrium, with a thorium-poor and yttrium-rich core, was evident in grain I1 (Fig. 16f–g).

A total of 11 analyses were obtained from four monazite grains (Appendix 3). Excluding the two high common-Pb results for F1, the remaining nine analyses of three grains agree to within analytical precision and yield a concordant weighted mean $^{207}Pb/^{206}Pb$ date of 1966 ± 7 Ma (MSWD = 2.4; Fig. 16h–i). This is interpreted as the age of monazite growth during the medium- to high-grade metamorphism experienced by this sample. Retrogression and alteration of the matrix monazite to Fe-oxide minerals must have occurred during the extensive greenschist facies event that accompanied the production of the $S_2$ fabric.

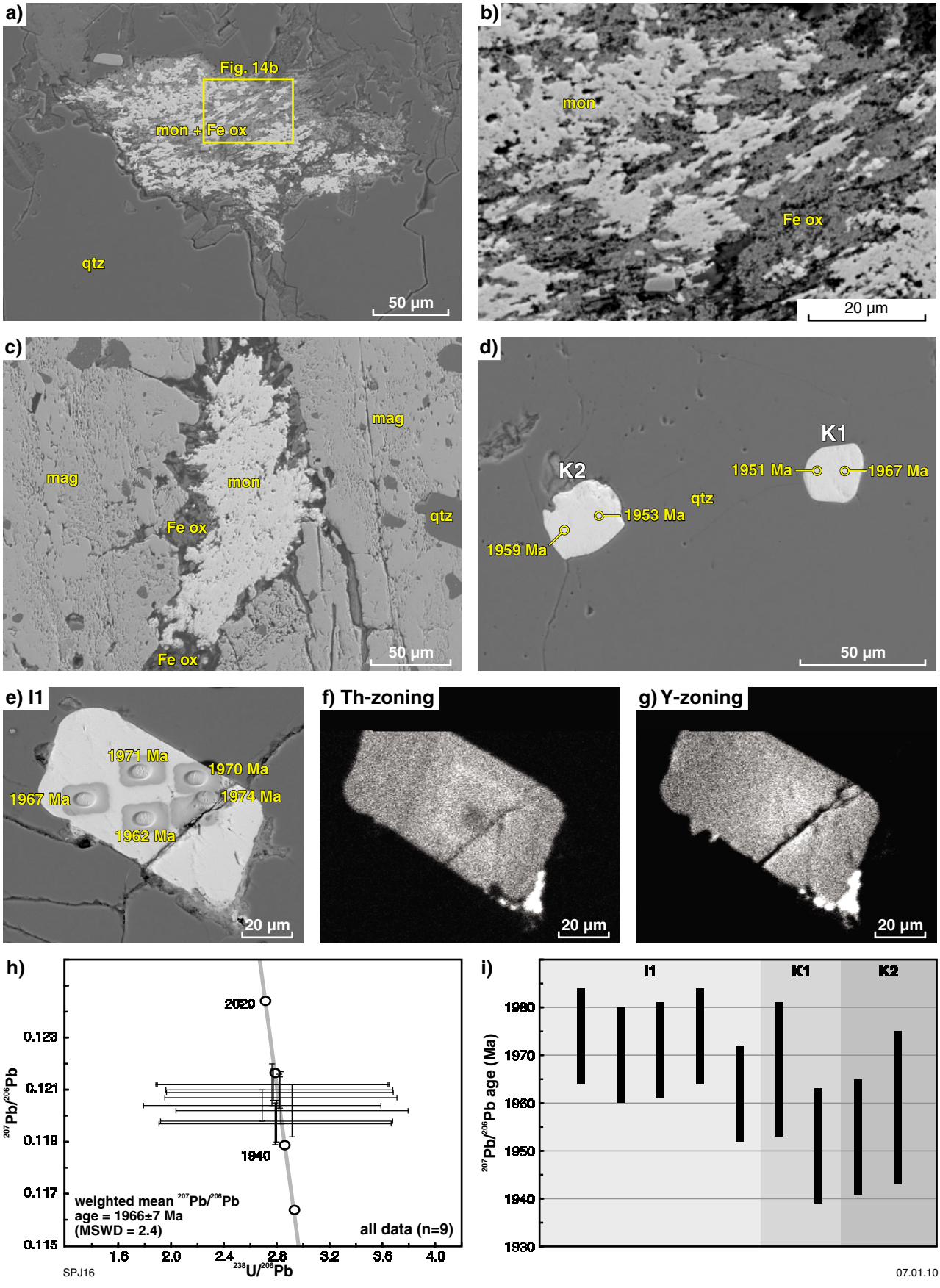
a)
Fig. 14b
mon + Fe ox
qtz
50 µm
b)
mon
Fe ox
20 µm
c)
mag
mag
mon
qtz
Fe ox
Fe ox
50 µm
d)
K1
K2
1951 Ma
1967 Ma
qtz
1953 Ma
1959 Ma
50 µm
e) I1
1971 Ma
1970 Ma
1967 Ma
1974 Ma
1962 Ma
20 µm
f) Th-zoning
20 µm
g) Y-zoning
20 µm
h)
2020
0.123
0.121
0.119
0.117
0.115
1940
weighted mean 207Pb/206Pb
age = 1966±7 Ma
(MSWD = 2.4)
all data (n=9)
1.6
2.0
2.4
2.8
3.2
3.6
4.0
SPJ16
238U/206Pb
i)
I1
K1
K2
1980
1970
1960
1950
1940
1930
207Pb/206Pb age (Ma)
07.01.10

### GSWA 164333: chloritoid schist

Sample 164333 is a coarse-grained chloritoid–sericite–quartz–muscovite–biotite schist from the central belt of the Mumba Psammite (Fig. 1) and from a similar part of the package as GSWA 184160. Both chloritoid and sericite are randomly oriented and appear to replace former peak metamorphic minerals (possibly garnet and sillimanite, respectively), indicating that this rock experienced high-grade metamorphic conditions prior to being subjected to an intense greenschist facies overprint. Monazite is widespread as 25–50 μm subidioblastic crystals that occur in both the matrix and as inclusions within randomly oriented chloritoid crystals (Fig. 17a–d). The monazite is variably replaced around its margins by a mixture of Fe-oxide and ?REE-minerals with some monazite grains being almost totally replaced (Fig. 17b).

Twelve variably altered grains were selected for analysis. Element mapping revealed no significant variations in lanthanum, thorium, or yttrium. Thirteen analyses of 12 grains are dispersed along concordia between 1960 Ma and 1840 Ma (Appendix 3, Fig. 17e,g). It is apparent that the least altered grains provide the oldest ages (compare grains D1 and G1 with grains F1 and H1; Fig. 17a–d), suggesting that significant dissolution and reprecipitation of monazite occurred during the greenschist facies alteration event. Analysis of the five least altered grains indicate $^{207}Pb/^{206}Pb$ dates that are indistinguishable at the 2σ level, yielding a concordant weighted mean date of 1947 ± 11 Ma (MSWD = 1.6; Fig. 17f). This result is consistent with those obtained from the other two samples (GSWA 164369 and 168713), which are interpreted to date the timing of monazite growth during high-grade metamorphism. The youngest $^{207}Pb/^{206}Pb$ date of c. 1840 Ma provides a maximum age constraint on the timing of the greenschist facies alteration event.

# Laser ablation Lu–Hf isotopes of zircon

The three samples of Quartpot Pelite analysed in this study contain two abundant detrital zircon age components of 2250–2175 Ma and 2080–2000 Ma. As there are no rocks of equivalent ages known in the Gascoyne Province, the sources of these sediments are unclear. Several zircon grains from each of these detrital modes were selected and analysed by laser ablation mass spectrometry to determine their Lu–Hf isotope ratios. These data provide critical information on the tectonomagmatic origin and evolution of this cryptic basement and, possibly, the tectonosedimentary environment within which the Quartpot Pelite was deposited.

The analyses were conducted by laser ablation multi-collector inductively coupled plasma mass spectrometry (LA-MC-ICPMS) at the Centre for Geochemical Evolution and Metallogeny of Continents (GEMOC), Macquarie University, during April 2009. A detailed account of the analytical procedures and the full table of the Lu–Hf isotopic results are presented in Appendix 4. The initial $^{176}Hf/^{177}Hf$ ratios were calculated using the decay constant for $^{176}Lu$ ($1.865 \times 10^{-11}$) proposed by Scherer et al. (2001), and the hafnium crustal model ages ($T^{C}_{DM}$) were calculated from the observed initial hafnium isotopic ratio (εHf(t)) and an average Precambrian granitic crust $^{176}Lu/^{177}Hf$ ratio of 0.015 (Griffin et al., 2002).

### GSWA 142910: retrogressed pelitic diatexite

Fourteen zircon grains were selected for analyses. Four of these yielded $^{207}Pb/^{206}Pb$ dates of 2295–2174 Ma, whereas the remaining ten grains form part of the 2080–2030 Ma population. A full table of results is presented in Appendix 4. The older 2295–2174 Ma group spans a range of isotopic compositions with intial $^{176}Hf/^{177}Hf$ values of 0.281085 – 0.281275 and εHf(t) values of -9.2 to -1.6, which correspond to crustal model ages ($T^{C}_{DM}$) between 3.42 Ga and 2.97 Ga (Appendix 4). The younger 2080–2030 Ma component has a range of isotopic compositions with initial $^{176}Hf/^{177}Hf$ ratios of 0.281287 – 0.281368 and εHf(t) values of -7.2 to -3.2 (Fig. 13d; Appendix 4), which correspond to crustal model ages ($T^{C}_{DM}$) between 3.12 and 2.91 Ga. Within this group there is a possible trend toward more evolved compositions (i.e. increasing negative εHf(t) values toward younger ages) with a total change in εHf(t) from 2080 to 2030 Ma of ~-2 units (Fig. 13d). Detrital zircon grains from both older and younger components were derived from a basement that formed during the Paleoproterozoic by the addition or mixing of older Archean crust with juvenile mantle-derived material.

### GSWA 142905: retrogressed pelitic diatexite

Fifteen zircons were selected for analysis, of which three have $^{207}Pb/^{206}Pb$ dates of 2226–2113 Ma, and the remaining 12 form part of the 2075–2000 Ma group. A full table of results is presented in Appendix 4. The oldest

**Figure 17. (facing page) In situ monazite age data from a chloritoid schist of the Mumba Psammite (GSWA 164333): a) SEM image showing subhedral monazite (mon) grain D1 as an incusion, along with quartz (qtz) grains, within a chloritoid (cld) porphyroblast. The position of the SHRIMP analytical pit and corresponding $^{207}Pb/^{206}Pb$ age is also shown; b) SEM image of highly altered monazite grain F1 within a chloritoid porphyroblast, and the position of the SHRIMP analytical pits and corresponding $^{207}Pb/^{206}Pb$ ages are also shown; c) SEM image of an euhedral monazite (Grain G1) within a matrix porphyroblast of muscovite (ms). Chloritoid porphyroblasts containing abundant quartz inclusions are also visible in the top right of the image. The position of the SHRIMP analytical pit and corresponding $^{207}Pb/^{206}Pb$ age is also shown; d) intensely altered monazite grain H1 and the obtained $^{207}Pb/^{206}Pb$ age; e) Tera–Wasserburg U–Pb plot for all monazite analyses; f) Tera–Wasserburg U–Pb plot for the oldest ve concordant monazite analyses; g) summary diagram showing the $^{207}Pb/^{206}Pb$ age distribution (each analyses is at the 2σ level) for every U–Pb analyses within each monazite grain. U–Pb age data for all SHRIMP analytical spots are tabulated in Appendix 3.**

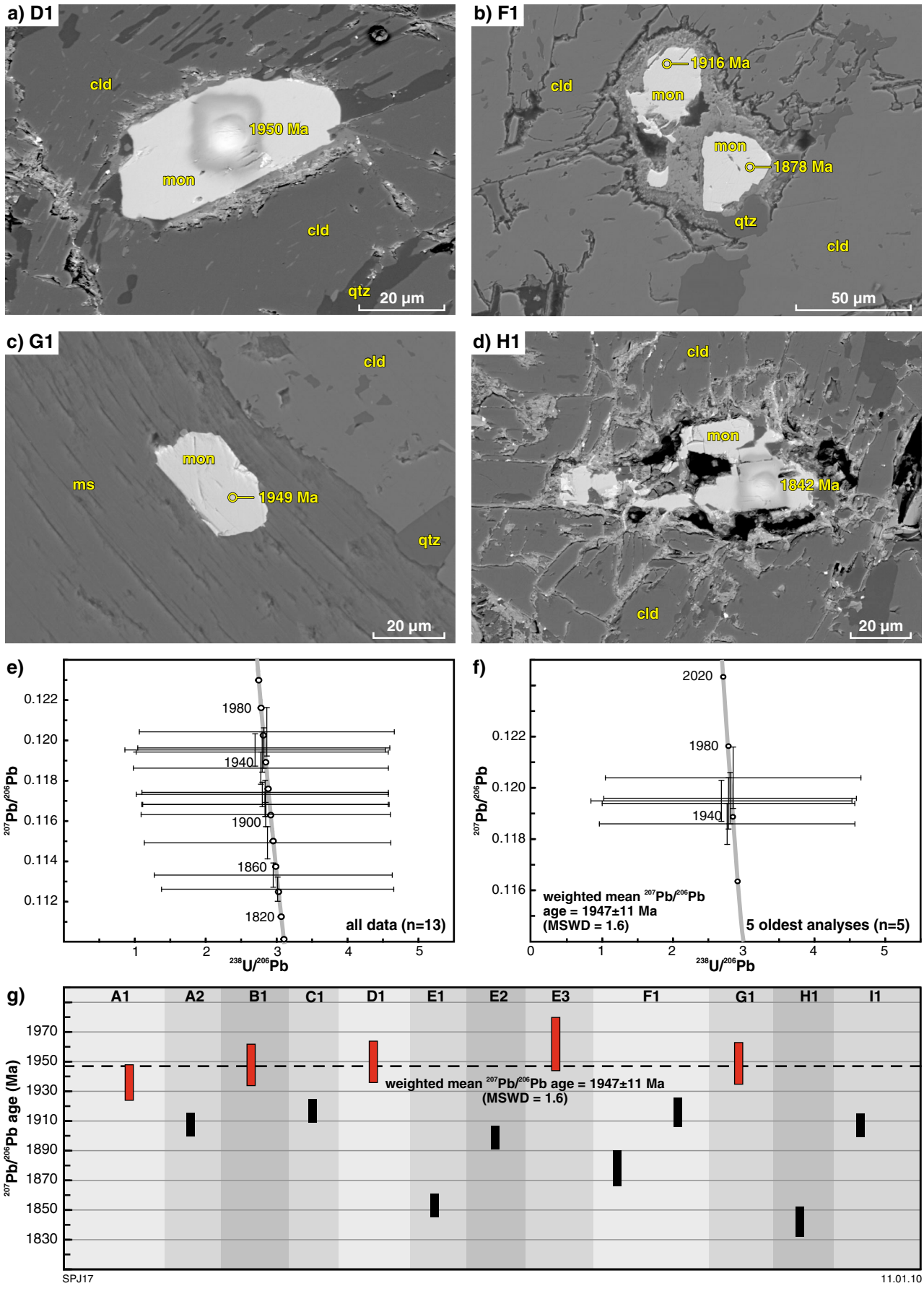
a) D1
cld
1950 Ma
mon
cld
qtz
20 µm
b) F1
1916 Ma
cld
mon
mon
1878 Ma
qtz
cld
50 µm
c) G1
cld
mon
ms
1949 Ma
qtz
20 µm
d) H1
cld
mon
1842 Ma
cld
20 µm
e)
0.122
0.120
0.118
0.116
0.114
0.112
207Pb/206Pb
1980
1940
1900
1860
1820
all data (n=13)
1
2
3
4
5
238U/206Pb
f)
2020
0.122
0.120
0.118
0.116
207Pb/206Pb
1980
1940
weighted mean 207Pb/206Pb
age = 1947±11 Ma
(MSWD = 1.6)
5 oldest analyses (n=5)
0
1
2
3
4
5
238U/206Pb
g)
A1
A2
B1
C1
D1
E1
E2
E3
F1
G1
H1
I1
1970
1950
1930
1910
1890
1870
1850
1830
207Pb/206Pb age (Ma)
weighted mean 207Pb/206Pb age = 1947±11 Ma
(MSWD = 1.6)
SPJ17
11.01.10

three grains yield a narrow range of intial $^{176}Hf/^{177}Hf$ ratios of 0.281162–0.281356 and εHf(t) values of -6.8 to -2.9, which corresponds to crustal model ages ($T^{C}_{DM}$) between 3.25 and 2.91 Ga (Appendix 4). The younger 2075–2000 Ma group has a range of isotopic compositions with intial $^{176}Hf/^{177}Hf$ raios of 0.281193 – 0.281393 and εHf(t) values of -10.3 to -2.4 (Fig. 13h; Appendix 4), which correspond to crustal model ages ($T^{C}_{DM}$) between 3.33 and 2.85 Ga. Similar to GSWA 142910, there is a possible trend toward more evolved compositions, with a total unit change in εHf(t) from 2075 Ma to 2000 Ma of -2.5 units (Fig. 13h). Detrital zircon grains from both older and younger populations were derived from a basement that formed during the Paleoproterozoic by the addition or mixing of older Archean crust with juvenile mantle-derived material.

#### *GSWA 168944: psammitic schist*

Of 13 zircons selected for analyses, three yielded $^{207}Pb/^{206}Pb$ dates in the 2253–2223 Ma range. Although the remaining ten analyses have individual dates that range from 2080 to 1985 Ma, they are interpreted to be part of a single, statistically coherent, age component (see previous section) at c. 2025 Ma; thus, the hafnium isotopic ratios for all grains have been calculated at this age (Fig. 13i). A full table of results is presented in Appendix 4. The oldest three grains yield a narrow range of intial $^{176}Hf/^{177}Hf$ ratios of 0.281137–0.281222 and εHf(t) values of -7.5 to -4.5, which correspond to crustal model ages ($T^{C}_{DM}$) between 3.31 and 3.12 Ga (Appendix 4). The younger population of 10 grains at c. 2025 Ma yield a moderate range of intial $^{176}Hf/^{177}Hf$ ratios of 0.281245 – 0.281382 and εHf(t) values of -8.9 to -4.0, which correspond to crustal model ages ($T^{C}_{DM}$) between 3.22 and 2.91 Ga (Fig. 13l; Appendix 4). Similar to samples 142910 and 142905, detrital zircon grains from both older and younger populations were derived from a basement that formed during the Paleoproterozoic by the addition or mixing of older Archean crust with juvenile mantle-derived material.

# Discussion

## Basin provenance

### Moogie Metamorphics

The Mumba Psammite is dominated by detrital zircons in the 2600–2300 Ma age range, but also contains zircons as old as c. 3200 Ma, and includes minor age components at c. 2750 Ma, c. 2680 Ma, 2520–2500 Ma, and c. 2450 Ma (Fig. 18). Apart from the pelitic diatexite sample GSWA 185942 from the Paradise Zone, which appears to be somewhat different to the other samples and will be considered separately, the youngest detrital zircons in all samples are between 2369 and 2240 Ma (Fig. 18; Table 1). If the older metamorphic monazite and zircon cores within GSWA 164369 grew in situ, then protoliths to the Mumba Psammite were deposited prior to metamorphism. This metamorphism is here constrained to between 2240 Ma and 2125 Ma (Table 1).

The younger detrital zircon age components in the Moogie Metamorphics correspond closely to the crystallization ages of the Halfway Gneiss protoliths (Sheppard et al., 2008a; Appendix 1), whereas the older components are similar in age to inherited zircon components within the Halfway Gneiss. This observation is supported (at the 95% confidence level) by the Kolmogorov–Smirnoff (K–S) test (Appendix 2), a nonparametric statistical method which determines if there is a significant difference or similarity between age populations, in this case between the detrital zircon age profiles of the Moogie Metamorphics and those of potential basement sources including the Halfway Gneiss, the Camel Hills Metamorphics, the Yilgarn Craton, and the Yarlarweelor Gneiss Complex (Table 2). Not only is there good internal consistency throughout the Mumba Psammite samples, but there is also good correlation with several units of the Halfway Gneiss (Table 2; Appendix 2). This internal consistency suggests that irrespective of composition (i.e. pelite, psammite, or quartzite) or location (i.e. northern, central, or southern belts), there is a similar source region for all samples. The unconformable relationships between the Mumba Psammite and the Halfway Gneiss observed on the southern part of YINNETHARRA (Sheppard et al., 2008b), and similarity of zircon populations, imply that the metasedimentary rocks may have been sourced from the underlying Halfway Gneiss. GSWA 184160, a psammite from the central belt, shows only weak correlation with the other Mumba Psammite samples, but does demonstrate a strong correlation with two Halfway Gneiss samples (GSWA 168950 and NP21), with $p$ values of 0.185 and 0.885, respectively (Table 2; Appendix 2).

Because of the destruction of sedimentary features during high-grade metamorphism and deformation, there is very little sedimentological evidence remaining to determine the facies or tectonic setting in which the Moogie Metamorphics were deposited. As a result, any discussion is based on broad, regional-scale inferences. The detrital zircon age spectra specifically demonstrate that they were sourced directly from the underlying basement and contain no evidence of any syn-depositional volcanic detritus, potentially eliminating fore-arc or accretionary wedge settings. The predominance of siliciclastic lithologies over carbonates and shelf-type sediments also suggests an intracontinental setting.

The age of deposition is broadly coeval with the Ophthalmian Orogeny (2215–2145 Ma; Rasmussen et al., 2005) — the collision or accretion of the Glenburgh Terrane with the Pilbara Craton — and these rocks may have been deposited in a foreland basin in response to uplift and erosion of northward-propagating thrust stacks on the southern Pilbara Craton margin (Fig. 19a; Blake and Barley, 1992). However, they lack any Ophthalmian-aged detritus, suggesting either that material was sourced from basement rocks far to the south of the orogenic front, or that only the low-grade parts of the thrust nappes (those that did not grow metamorphic zircon) were eroded into the basin (Fig. 19a).

Alternatively, since the polarity of subduction during the ocean closure phase of the Ophthalmian Orogeny is not known, subduction of oceanic crust may have

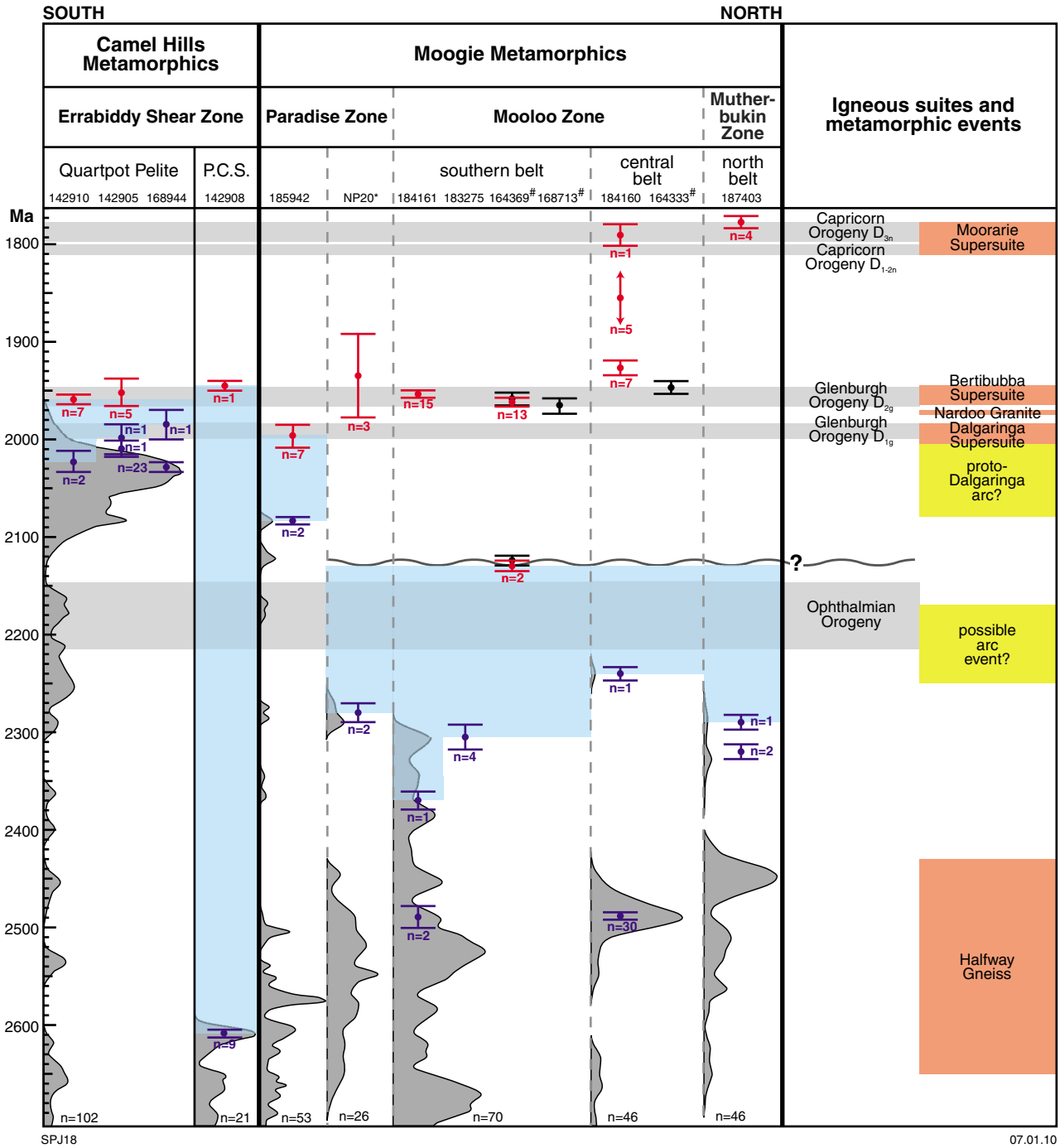


**Figure 18. Time–space plot for all samples dated in this study. Summary probability density distribution plots have been grouped for each formation, or in the case of the Mumba Psammite, on its location either within the southern, central, or northern belts (see main text). The dark blue error bars show the age of the youngest detrital zircon in each sample, the red error bars show the age of the metamorphic zircon dated from each sample, and the black error bars are the ages of the monazite from the samples. The blue transparent boxes show the age range of deposition for the precursor (meta)sediment as de ned by the youngest detrital zircon and the subsequent metamorphic overprint. The age of the known orogenic events are superimposed as grey bars and the age range of the known magmatic events are shown as orange (known) and yellow (inferred from this study) boxes. Abbreviations used: P.C.S. = Petter Calc-silicate; # = monazite.**

**Table 2. K–S test comparing the detrital zircon age modes within the Camel Hills and Moogie Metamorphics with those of potential basement terranes**

| | | | *Camel Hills Metamorphics* | | | | *Moogie Metamorphics* | | | | | |
|---|---|---|---|---|---|---|---|---|---|---|---|---|
| | | | *Quartpot Pelite* | | | *Petter Calc-silicate* | *Southern belt* | | *Central belt* | *Northern belt* | *Isolated* | |
| | | | *142910* | *142905* | *168944* | *142908* | *184161* | *183275* | *184160* | *187403* | *NP20** | *185942* |
| *Camel Hills Metamorphics* | *Quartpot Pelite* | *142910* | – | 0.017 | **0.156** | 0.000 | 0.000 | 0.000 | 0.000 | 0.000 | 0.000 | 0.000 |
| | | *142905* | 0.017 | – | **0.119** | 0.000 | 0.000 | 0.000 | 0.000 | 0.000 | 0.000 | 0.000 |
| | | *168944* | **0.156** | **0.119** | – | 0.000 | 0.000 | 0.000 | 0.000 | 0.000 | 0.000 | 0.000 |
| | *Petter Calc-silicate* | *142908* | 0.000 | 0.000 | 0.000 | – | 0.013 | 0.000 | 0.000 | 0.000 | 0.000 | 0.002 |
| *Moogie Metamorphics* | *Southern belt* | *184161* | 0.000 | 0.000 | 0.000 | 0.130 | – | 0.032 | 0.000 | 0.017 | **0.503** | **0.985** |
| | | *183275* | 0.000 | 0.000 | 0.000 | 0.000 | 0.032 | – | 0.034 | **0.241** | **0.150** | 0.000 |
| | *Central belt* | *184160* | 0.000 | 0.000 | 0.000 | 0.000 | 0.000 | 0.034 | - | 0.011 | 0.000 | 0.000 |
| | *Northern belt* | *187403* | 0.000 | 0.000 | 0.000 | 0.000 | 0.017 | **0.241** | 0.011 | – | 0.023 | 0.000 |
| | *Isolated* | *NP20** | 0.000 | 0.000 | 0.000 | 0.000 | **0.503** | **0.150** | 0.000 | 0.023 | - | **0.399** |
| | | *185942* | 0.000 | 0.000 | 0.000 | 0.002 | **0.985** | 0.000 | 0.000 | 0.000 | **0.399** | – |
| *Halfway Gneiss* | | *168950* | 0.000 | 0.000 | 0.000 | 0.000 | 0.001 | **0.468** | **0.185** | **0.557** | 0.005 | 0.000 |
| | | *164309* | 0.000 | 0.000 | 0.000 | 0.000 | 0.001 | 0.003 | 0.000 | 0.000 | 0.032 | 0.000 |
| | | *142988* | 0.000 | 0.000 | 0.000 | **0.381** | **0.117** | 0.000 | 0.000 | 0.000 | 0.003 | 0.007 |
| | | *NP21** | 0.000 | 0.000 | 0.000 | 0.000 | 0.001 | **0.136** | **0.885** | **0.176** | 0.003 | 0.000 |
| *Yilgarn Craton and Yarlarweelor Gneiss Complex* | | *142906* | 0.000 | 0.000 | 0.000 | **0.281** | 0.006 | 0.000 | 0.000 | 0.000 | 0.000 | 0.000 |
| | | *142897* | 0.000 | 0.000 | 0.000 | **0.179** | 0.008 | 0.000 | 0.000 | 0.000 | 0.000 | 0.000 |
| | | *139467* | 0.000 | 0.000 | 0.000 | 0.000 | 0.000 | 0.000 | 0.000 | 0.000 | 0.000 | 0.000 |
| | | *142853* | 0.000 | 0.000 | 0.000 | 0.004 | 0.000 | 0.000 | 0.000 | 0.000 | 0.000 | 0.000 |

**NOTE:** Numbers in bold text indicate statistically significant values

been to the south under the Glenburgh Terrane. In this case, the Moogie Metamorphics would have been deposited in a large extensional continental back-arc basin, or in a compressional retro-arc basin, both of which would have been a significant distance away from, and outside the influence of, the active magmatic arc (Fig. 19a).

Without knowing the subduction polarity leading up to the Ophthalmian Orogeny, little more can be speculated about the tectonosedimentary setting for the deposition of these sedimentary rocks; however, each of the two models would require critically different geometries and tectonic settings for the deposition of the Lower Wyloo Group of the Ashburton Basin (Fig. 19a). Regional structural–sedimentological work demonstrates that the lowermost units of the Ashburton basin, the Beasley River Quartzite and Cheela Springs Basalt, are in unconformable contact with the older Turee Creek and Hamersley Groups of the Hamersley Basin (Thorne and Seymour, 1991; Martin et al., 1998). Limited detrital zircon geochronology from the Beasley River Quartzite (GSWA 169084) indicates a source similar to the underlying Hamersley and Turee Creek Groups. These data indicate that the Lower Wyloo Group was deposited on the margin of, and sourced from, the Pilbara Craton and associated Hamersley Basin. This geometry favours the foreland basin model, because in the retro-arc model (Fig. 19a) the Lower Wyloo Group would have been deposited as a package of continental margin arc-related sediments, sourced from the northern margin of the Glenburgh Terrane, far from the influence of the Pilbara Craton (Fig. 19a). Unequivocal evidence in favour of one or other of the models could be found by recognizing and dating detrital components within any of the Moogie Metamorphic packages or their temporal equivalents further north, and therefore closer to the orogenic front.

The pelitic diatexite from Paradise Well (GSWA 185942) contains numerous zircons with dates between 2170 and 2080 Ma, which suggest a significantly younger depositional age than for the Mumba Psammite proposed above. The youngest detrital zircons (two grains) are dated at c. 2080 Ma and, along with a few grains dated at 2280–2170 Ma, appear to have some age populations in common with those of the Quartpot Pelite (Fig. 18). However, a statistical comparison (the K–S test) of the detrital modes (Table 2; Appendix 2) provides a strong correlation only with other samples of the Mumba Psammite. This sample also contains a few detrital metamorphic zircon grains and rims dated at c. 2125 Ma, which are identical in age to metamorphic zircon and monazite developed in situ within the Mumba Psammite (sample GSWA 164369). Considering these relationships, this metasedimentary rock is interpreted as a second-cycle deposit sourced from the erosion of the Mumba Psammite sometime after c. 2080 Ma, but before the growth of metamorphic zircon rims at c. 2000 Ma.

The youngest detrital zircons at c. 2080 Ma overlap in age with those of the bulk of detrital zircons from the Quartpot Pelite, suggesting that the unit may also have been partly sourced from the proto-Dalgaringa arc as part of a fore-arc or accretionary wedge-type deposit (Fig. 19b). However, unlike the Quartpot Pelite, this sample was metamorphosed during the $M_{1g}$ event, i.e. prior to the deposition of the Quartpot Pelite (Table 1). The paucity of 2095–1985 Ma detrital zircons in this sample suggests that source contributions from the arc were limited, or that this sample was deposited shortly after c. 2080 Ma. The younger depositional age and the fact that the Moogie Metamorphics themselves were a source for this sediment indicate that it cannot be part of the Moogie or Camel Hills Metamorphics.

## Camel Hills Metamorphics

All three samples from the Quartpot Pelite are dominated by detrital zircons in the range 2080–2000 Ma, with this group defined by >55% of the dated zircons (68 of 119 analyses). The samples also contain two distinct components at c. 2250 and 2175 Ma (Fig. 18) and a host of individual zircon analyses dating back to c. 2890 Ma (Fig. 18). The source of these metasedimentary rocks is unclear as there are no known dated rocks in the Glenburgh Terrane or Yilgarn Craton with ages of 2250–2005 Ma (Fig. 18). This observation is supported by the K–S test (Table 2; Appendix 2). Zircon crystallinity values indicate that the range of zircon ages, between 2095 and 1985 Ma in all three samples, is unlikely to reflect variable loss of radiogenic Pb from zircon structures during $M_{2g}$ metamorphism (Fig. 13b,f,j). Instead, significant age components from all three samples can be resolved at c. 2080, c. 2075, c. 2065, c. 2050, c. 2030, c. 2025, and c. 2000 Ma, reflecting derivation from a multicomponent age source. The hafnium isotopic signatures of these detrital zircons have a range of εHf(t) values between -10.3 and -2.4 indicating juvenile and evolved crust in the source region. These samples were deposited after c. 2000 Ma, but prior to the growth of metamorphic zircon rims recorded in samples GSWA 142910 and 142905 at 1959 Ma and 1952 Ma, respectively (i.e. during $D_{2g}$ tectonometamorphism; Fig. 18; Table 1).

The timing of deposition overlaps with the age of $D_{1g}$ deformation in the older portion (2005–1985 Ma) of the Dalgaringa Supersuite, suggesting that these metasedimentary rocks may have been sourced by the active erosion of these arc-related rocks during deformation; however, only three of 119 detrital grains dated in these metasedimentary rocks are of Dalgaringa Supersuite age. This suggests that either the Quartpot Pelite was sourced from a currently unexposed — or tectonically removed or eroded — part of a proto-Dalgaringa arc, or was sourced from a currently unknown, possibly exotic (to the Glenburgh Terrane) terrane that contained minor age components similar to those of the Dalgaringa Supersuite.

Minor, inherited zircon components with ages in the 2055–2020 Ma range are present within two dated Dalgaringa Supersuite metamonzogranites (GSWA 168949 and 168951), providing support for the proto-Dalgaringa arc concept. Furthermore, comparisons of the detrital zircon Lu–Hf isotopic compositions with the whole-rock Sm–Nd compositions of the Dalgaringa Supersuite show excellent correlation (Fig. 20a). The more evolved end members of the Dalgaringa Supersuite (felsic rocks

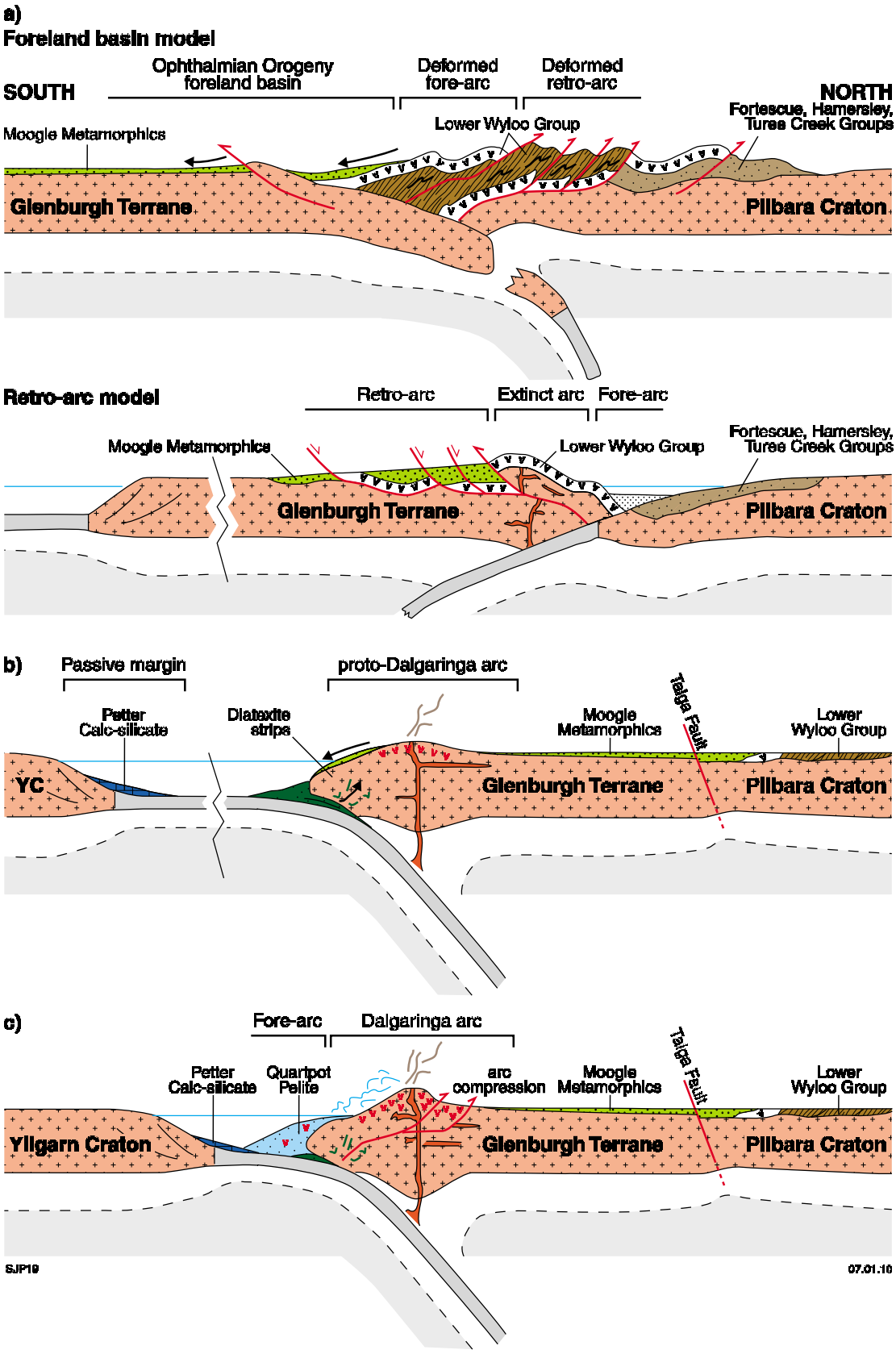


**Figure 19.** Schematic cross sections, showing possible tectonic settings for deposition of the various siliciclastic packages in the southern Gascoyne Province: a) 2240–2125 Ma provenance of the Moogie Metamorphics; b) 2080–2000 Ma provenance of the diatexite strips and Petter Calc-silicate; c) 2000–<1985 Ma ($D_{1g}$) provenance of the Quartpot Pelite. Note that cross sections are not intended to infer orthogonal collision or plate motions between two tectonic blocks or cratons. See main text for detailed discussion.

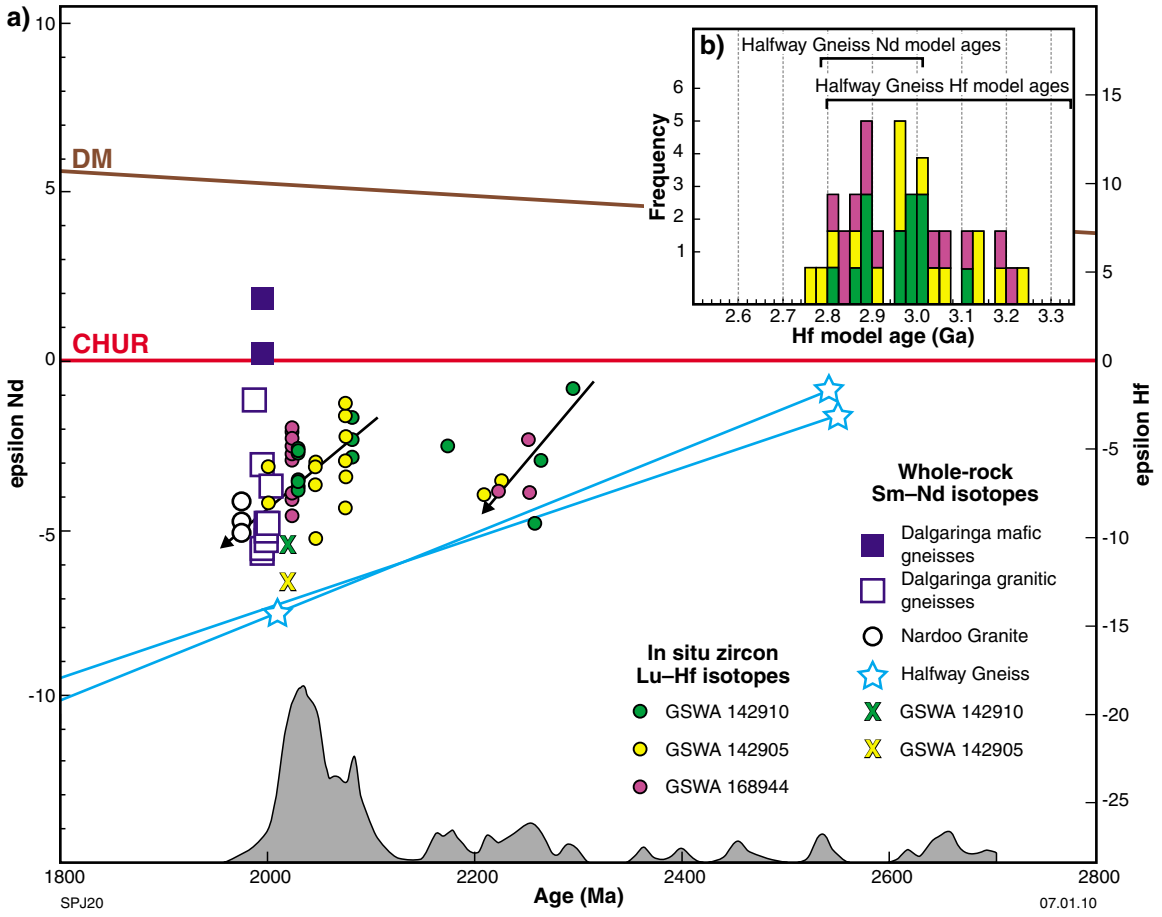


**Figure 20. In situ zircon Lu–Hf and whole-rock Sm–Nd isotopic composition (and evolution) of the Quartpot Pelite and Dalgaringa Supersuite. The Sm–Nd data are from Sheppard et al. (2004) and the in situ zircon Lu–Hf data are tabulated in full in Appendix 4: a) εNd and εHf plot, showing the isotopic evolution of detrital zircon from the Quartpot Pelite and whole rock equivalents, including those from the Dalgaringa Supersuite; b) histogram of the zircon hafnium model age from each of the three Quartpot Pelite samples. These ages are compared to the range of whole rock neodymium model ages (Sheppard et al., 2004) and magmatic/inherited zircon hafnium model ages (GSWA, unpublished data), available from the Halfway Gneiss.**

with intermediate to acid compositions) have moderately negative (in comparison with Chondritic Uniform Reservoir or CHUR) εNd(t) values (-6 to -1) that reflect mixing between juvenile mantle-derived arc magmas and non-radiogenic early Paleoproterozoic basement — the Halfway Gneiss — within a continental marginal arc setting (Sheppard et al., 2004). A similar relationship is observed in the zircon Lu–Hf isotopic data, which suggest formation in a simple two-component system, with mixing between mantle-derived juvenile ?arc material and a basement with similar isotopic compositions to those of the Halfway Gneiss (Fig. 20a). This association is also reflected by the similar depleted-mantle model ages for both the detrital zircons and the Halfway Gneiss (Fig. 20b). Given that mafic rocks commonly lack magmatic zircon, the more juvenile components to the system — as represented by the amphibolites and mafic gneisses in the Dalgaringa Supersuite (Fig. 20a) — will not be recorded in the detrital zircon record of the metasedimentary rocks. However, the whole-rock Sm–Nd isotopic values for two of the metasedimentary rocks (GSWA 142910 and 142905; GSWA, unpublished data) are relatively evolved, with εNd(t) values of -5.38 and -6.45, respectively. These values are at the lower end of the range defined by the zircon Lu–Hf data, indicating that there was probably very little input of juvenile mafic material into the sedimentary detritus, at least not enough to significantly influence the neodymium isotopic values.

The Lu–Hf and Sm–Nd isotopic systems demonstrate that the intermediate to acid parts of the Dalgaringa arc (including the proto-Dalgaringa arc) evolved progressively, a process that is commonly observed in Cordilleran-type continental margin arcs (e.g. DeCelles et al., 2009). Although the isotopic data are relatively limited, it is also interesting to note that a potentially similar magmatic–isotopic evolution is recorded by the 2250–2175 Ma zircons (Fig. 20a). Any intermediate to acid additions to the crust were dominated by a simple two-component system with mixing between mantle-derived juvenile ?arc material and a basement with isotopic compositions similar to the Halfway Gneiss (Fig. 20a, b). This group of older detrital zircons yields hafnium model ages that

span the entire range defined by the younger population; however, one zircon (GSWA 142910 analysis 12.1) has a hafnium model age (of 3.21 Ga; Fig. 20b; Appendix 4) that is older than that for the Halfway Gneiss (Fig. 20b). One sample of Halfway Gneiss (GSWA 142988), with a model age of c. 3.0 Ga (Sheppard et al., 2004), contains inherited zircon xenocrysts as old as c. 3.55 Ga, indicating that there must be much older components to, or at least basement that sourced, the Halfway Gneiss.

The distinct paucity of 2005–1985 Ma arc-related zircons in the Quartpot Pelite, and the current proximity of this package to exposed Dalgaringa Supersuite rocks, implies that there must have been extensive post-Glenburgh strike-slip movements between the two units. These movements may be evidenced by the presence of post-1800 Ma, shallow plunging lineations throughout the Errabiddy Shear Zone (Reddy and Occhipinti, 2004), transporting the Quartpot Pelite away from its proto-Dalgaringa arc source region.

The Petter Calc-silicate contains an entirely different detrital zircon population to the Quartpot Pelite (Fig. 18, Table 2). It contains only Archean detritus, with the youngest detrital zircon component at c. 2610 Ma, suggesting that the unit was either deposited in the late Archean, or it was deposited much later with detritus sourced entirely from Archean rocks. The sample contains two minor age components at 2660–2650 Ma and 2690 Ma, and also contains a few individual older zircon analyses between 3150 and 3030 Ma. A single metamorphic rim dated at c. 1945 Ma provides a younger age limit for its deposition, resulting in a rather large interval between 2610 and 1945 Ma.

A statistical comparison (the K–S test) of the age populations within the Petter Calc-silicate sample to those within potential basement sources, indicate that they are statistically similar at the 95% confidence level to two monzogranites (GSWA 142906 and 142897, with *p* values of 0.281 and 0.179 respectively; Table 2; Appendix 2) considered to be representative of the northern part of the Yilgarn Craton, and to a tonalitic gneiss of the Halfway Gneiss (GSWA 142988 with a *p* value of 0.381). Although there is a strong statistical correlation with the tonalitic gneiss, the lack of any detrital zircon grains younger than c. 2600 Ma in the Petter Calc-silicate sample potentially rules out the Halfway Gneiss as a source, as most of these basement rocks have much younger crystallization ages (2660–2430 Ma; Sheppard et al., 2008a; Fig. 18). As such, the sole presence of Archean detritus with age components between 2690–2650 Ma and c. >3000 Ma, suggests that the Petter Calc-silicate was derived entirely from the Yilgarn Craton, outside the influence of the Glenburgh Terrane and any volcanic-arc activity. The Petter Calc-silicate was possibly deposited as part of a passive margin along the northern edge of the craton prior to collision with the Glenburgh Terrane, although the exact timing of the unit's deposition remains unconstrained. Although the Petter Calc-silicate is currently tectonically interleaved with the Quartpot Pelite, its detrital zircon components clearly suggest that the two formations were deposited in different, widely separated basins, possibly at different times.

# Timing and signi cance of the Glenburgh Orogeny and subsequent tectonometamorphic events

## $D_{1g}$ metamorphism and deformation

The highest grade metamorphic assemblages associated with $M_{1g}$ metamorphism are preserved in strips of granulite facies pelitic diatexite and metamafic igneous rocks in the central part of the Paradise Zone (Fig. 2). These rocks are interleaved with foliated and gneissic granites of the Dalgaringa Supersuite. The exceedingly high ZnO and FeO content of the hercynitic and gahnitic spinels (3–21 wt% ZnO and 17–30 wt% FeO; GSWA, unpublished data), preclude the empirical calculation of the peak pressure–temperature (PT) conditions using either equilibrium thermodynamics or via pseudosections. However, the presence of corundum–spinel–almandine garnet in rocks of pelitic composition have been interpreted to record high-temperature and moderate- to high-pressure conditions in the range ~800–1000°C and 7–10 kbar (Schulters and Bohlen, 1988). Elsewhere in this zone, $M_{1g}$ metamorphism appears to have peaked only in the upper amphibolite facies with the regional scale development of gneissic fabrics and folds. In the granulite facies rocks, the discontinuous diatexite melt veins are aligned with these regional $S_{1g}$ gneissic fabrics, indicating that in both amphibolite and granulite facies rocks, peak metamorphism and deformation were synchronous. The timing of this metamorphism is recorded in the pelitic diatexite (GSWA 185942) by the growth of low Th/U, CL- and texturally-homogenous metamorphic zircon rims with an age of 1997 ± 10 Ma (Fig. 18).

The Dalgaringa Supersuite records a near-continual record of arc magmatism and accompanying deformation from 2005–1985 Ma (Occhipinti and Sheppard, 2001), suggesting that $D_{1g}$ was much longer lived than the apparent single event recorded in the diatexite. The age of metamorphism recorded in the diatexite represents the time that the metasedimentary rocks underwent melting with production of a near-anhydrous mineral assemblage. These anhydrous assemblages would have precluded the growth of any new metamorphic zircon during the subsequent prolonged $M_{1g}$ event. The moderate to high pressures implied by the diatexite, which formed at the same time as the Dalgaringa arc magmatism and deformation, suggest that $M_{1g}$ was related to arc construction in the middle crust.

## $D_{2g}$ metamorphism and deformation

Metamorphism and deformation associated with the $D_{2g}$ event are present throughout the entire Glenburgh Terrane, making this the first event common to all zones and siliciclastic packages, and suggesting that the juxtaposition of the terrane's units occurred at this time. In the Camel Hills and Moogie Metamorphics, $M_{2g}$ peaked in the upper amphibolite facies with the widespread production of anatectic melts in pelitic to semipelitic rocks. Although subsequent low-grade metamorphism and deformation

has obliterated the peak $M_{2g}$ metamorphic assemblages, the local preservation of original high-grade textures indicates that garnet and sillimanite were widespread porphyroblastic phases. The production of originally near-horizontal gneissic fabrics and foliations in all of the siliciclastic packages, together with the interleaving of lithologies along the Errabiddy Shear Zone, exemplifies the role of horizontal shortening (i.e. thrusting) in the region. In typical pelitic compositions, garnet and sillimanite are stable over a wide range of pressures (5–9 kbar) at temperatures above the wet solidus (during partial melting at >650°C; Rigby, 2009), and as such, metamorphism may have proceeded at moderately steep geothermal gradients without the widespread production of kyanite, of which there is not a single occurrence in the entire Gascoyne Province.

During the $D_{2g}$ event, new metamorphic zircon grew as thin rims around older detrital grains, without the resetting or variable loss of radiogenic lead from the detrital zircon components. This suggests that peak metamorphic conditions may not have greatly exceeded those needed to initiate melting under hydrous conditions (i.e. 650–700°C; Spear, 1993). In contrast, existing monazite appears to have suffered variable degrees of recrystallization and dissolution, and reprecipitation (e.g. GSWA 164369), along with new monazite growth (GSWA 168713 and 164333). Monazite growth or recrystallization occurred at the same time as that of metamorphic zircon, between 1965 Ma and 1950 Ma (Fig. 18).

## Younger orogenic events

Extensive low-grade overprinting of Glenburgh Orogeny fabrics and metamorphic mineral assemblages occurred during the 1820–1770 Ma Capricorn Orogeny (Fig. 2), and is documented in both zircon and monazite from the central and northern belts of the Moogie Metamorphics (Fig. 18). In the central belt (Mooloo Zone), monazite recrystallization (e.g. GSWA 164333) was accompanied by variable lead loss during dissolution and reprecipitation (Fig. 17). New zircon growth occurred as low- to moderate-Th/U rims around older cores at c. 1930 Ma, c. 1860 Ma, and c. 1790 Ma (GSWA 184160). The two older rim ages are anomalous as they lie between the known age constraints for both the Glenburgh and Capricorn Orogenies. Examination of the analytical pits with respect to the internal zircon structures suggests that the ages do not represent mixtures between core and rim domains. However, the oldest generation of rims at c. 1930 Ma are interpreted to have undergone some lead loss during the younger event(s), suggesting that they originally grew during the $D_{2g}$ event at 1965–1950 Ma. The middle group of analyses at c. 1860 Ma are equally difficult to explain, but it is evident that these rims have the same textural context as those dated at c. 1930 Ma, and nowhere do the c. 1860 Ma rims overgrow c. 1930 Ma rims (i.e. there are no core–mantle–rim textures). Furthermore, some of these analyses are from parts of grains that show some relict 'ghost' zoning, implying that this population is an artefact of variable resetting and recrystallization, and loss of radiogenic lead from older rims and detrital grains, rather than from the neocrystallization of zircon. This is reflected by the large $2\sigma$ error associated with the age (± 22 Ma), and by the variation within the group which cannot be explained by analytical uncertainties alone (MSWD of 2.3). The single concordant rim dated at c. 1790 Ma may represent the true age of the metamorphic or low-grade hydrothermal overprint as it is similar in age to four rims in sample GSWA 187403. If these detrital cores and rims had lost variable radiogenic lead during the 1965–1950 Ma and c. 1790 Ma events, shifting all the dates to younger ages, this may explain why there was no significant correlation between the detrital zircon populations in this sample with the rest of the Moogie Metamorphics (Table 2; Appendix 2).

In sample GSWA 187403 from the northern belt (Mutherbukin Zone), new metamorphic zircons with high uranium and very low Th/U ratios grew as rims around older cores at c. 1775 Ma. Combined with the age data obtained from sample GSWA 184160, low-grade metamorphism in the Mutherbukin Zone and northern part of the Mooloo Zone is broadly coincident with the latter stages ($D_{3n}$) of the Capricorn Orogeny as defined further south (Sheppard and Swager, 1999; Sheppard and Occhipinti, 2000; Occhipinti and Sheppard, 2001). The relatively simple structural, metamorphic, and geochronological evolution of the rocks in the northern Mooloo Zone and Mutherbukin Zone suggests that they did not experience the $D_{1n}$–$D_{2n}$ events that are prevalent further south. The age of metamorphism is contemporaneous with the intrusion of the main parts of the Minnie Creek batholith (Sheppard et al., in prep. a) in the adjacent Limejuice Zone. Dissolution and reprecipitation of monazite, and the neocrystallization and recrystallization of zircon in these rocks may have been facilitated by the regional-scale fluxing of hydrothermal fluids from the batholith.

# Tectonic evolution of the southwestern Capricorn Orogen

## >2.1 Ga

Igneous protoliths of the Halfway Gneiss crystallized between 2660 Ma and 2430 Ma, forming basement to the Glenburgh Terrane. A population of 2250–2175 Ma detrital zircons with slightly evolved Lu–Hf isotopic signatures from the Quartpot Pelite provides evidence for a period of intermediate to acid magmatic activity at this time. It is not clear whether this ?arc-related magmatism took place along the southern margin of the Glenburgh Terrane or as an outboard arc terrane with a continental basement similar in isotopic composition to the Halfway Gneiss. The sychronicity of arc magmatic activity with the 2215–2145 Ma Ophthalmian Orogeny (Rasmussen et al., 2005) indicates that the southern margin of the Glenburgh Terrane faced an oceanic realm — albeit with one or more arc terranes — throughout the duration of the orogeny. Collision and suturing of the Glenburgh Terrane with the Pilbara Craton took place along the northern margin of the terrane.

The precursors to the oldest supracrustal unit, the Moogie Metamorphics, were deposited sometime between 2240 Ma and 2125 Ma (Table 1; Fig. 18), and were

sourced directly from the underlying Halfway Gneiss basement. Deposition occurred either in a foreland basin setting or within a continental margin arc-related back-arc or retro-arc setting (Fig. 19a). The presence of both metamorphic zircon and monazite within sample GSWA 164369 suggests that parts of this siliciclastic basin, and presumably the underlying basement, were metamorphosed at c. 2125 Ma to metamorphic grades that were high enough to allow new zircon and monazite growth (Fig. 18). However, the lack of any distinct early (i.e. pre-$D_{2g}$) fabrics in both the Moogie Metamorphics and Halfway Gneiss suggest that any shear-dominated deformation and accompanied penetrative fabrics were only developed locally in discrete shear zones. The driver of this orogenic activity is unknown but the presence of arc-related magmatism prior to this event suggests the arc entered a compressional phase (e.g., DeCelles et al., 2009). Alternatively, if the 2250–2175 Ma arc magmatism took place in an outboard arc, then this event may record the accretion of this terrane or microcontinental fragment to the southern margin of the Glenburgh Terrane. By the end of the Ophthalmian Orogeny at c. 2145 Ma (Rasmussen et al., 2005), it is interpreted that the Glenburgh Terrane had collided with, or accreted to, the Pilbara Craton along a suture coincident with the Talga Fault (Blake and Barley 1992; Occhipinti et al., 2004; Selway, 2008; Selway et al., 2009).

## 2.10 – 1.96 Ga

The presence of numerous detrital zircon populations between 2080 Ma and 2000 Ma, with slightly evolved Lu–Hf isotopic compositions, suggests that continental margin arc magmatic activity was initiated (or reinitiated) along the southern margin of the Glenburgh Terrane shortly after the c. 2125 Ma metamorphic event (Fig. 18). Magmatism is attributed to an older, currently unexposed part of the Dalgaringa arc, the proto-Dalgaringa arc. Final closure of the oceanic tract between the Yilgarn and Pilbara–Glenburgh Cratons began sometime between 2125 Ma and 2080 Ma, with the initiation (reinitiation) of northward-directed subduction and arc magmatism below the Pilbara–Glenburgh Craton (Fig. 19b). Regional uplift of the Glenburgh Terrane, associated with the development of the continental arc, led to erosion of both the Moogie Metamorphics and the Halfway Gneiss basement in the subaerial regions of the fore-arc. These sediments would have been deposited along with variable proportions of synvolcanic detritus into the accretionary wedge. Some parts of the accretionary wedge were intercalated as thin strips with the mid-crustal parts of the arc and metamorphosed to high grade, presumably during a period of hinge zone advancement (i.e. GSWA 185942; Fig. 19b).

The currently exposed parts of the Dalgaringa Supersuite indicate that from c. 2005 Ma to c. 1985 Ma the arc was mainly under compression, although there may have been a significant strike-slip component, with repeated cycles of arc magmatism accompanied by deformation ($D_{1g}$; Fig. 19c). DeCelles et al. (2009) have suggested that 75–80% of continental margin arc magmatism takes place during high-flux episodes (HFEs) — some 3 to 4 times the rate of magmatism in primitive island arcs — and that these episodes coincide with, or are driven by, compressional cycles in the arc orogenic system. During the compressional cycle, rapid underthrusting and thickening of the arc lead not only to isostatic uplift, but to an increased contribution of the older unradiogenic basement to primitive arc magmas. This results in an isotopic 'pull down', i.e. magmatic rocks with increasingly evolved isotopic compositions, a trend observed in the evolution of the Lu–Hf and Sm–Nd isotopic systems of the proto-Dalgaringa arc between 2080 Ma and 1985 Ma (Fig. 20). Uplift and erosion during this compressional phase was responsible for the deposition of the Quartpot Pelite (Fig. 19c). However, the lack of abundant 2005–1985 Ma aged zircon detritus suggests that these sediments were sourced mainly from older (2080–2000 Ma) parts of the arc that are no longer exposed. Further detrital zircon dating may reveal parts of the Quartpot Pelite dominated by 2005–1985 Ma components. Deformation and regional arc compression ($D_{1g}$) appear to have ceased before the intrusion of the Nardoo Granite at 1979–1974 Ma — the youngest dated meta-igneous rock in the Dalgaringa Supersuite — as this arc-related intrusion contains only $D_{2g}$ fabrics.

## 1.96 – 1.94 Ga

The ages of metamorphic zircon and monazite (Table 1; Fig. 18) indicate that closure of the oceanic tract, the juxtaposition and interleaving of lithologies from both sides of the ocean, and the collision between the Pilbara–Glenburgh and Yilgarn Cratons occurred at 1965–1950 Ma. Unfortunately, the precision of the SIMS analyses on the metamorphic zircon and monazite components are not sufficient to allow any potential subdivision of this event (Fig. 18). The uniform development of subhorizontal $S_{2g}$ fabrics and medium- to high-grade $M_{2g}$ assemblages across the region (except in the Paradise Zone where $M_{2g}$ peaked in the lower amphibolite facies with the production of subvertical fabrics and folds) suggest that the $D_{2g}$ event was mainly compressional in nature. The ubiquitous presence of (now pseudomorphed and retrogressed) garnet and sillimanite porphyroblasts, along with locally preserved diatexite leucosomes, indicate that regional bulk shortening was accompanied by moderate to high geothermal gradients, leading to the extensive regional-scale anatexis of pelitic and semipelitic lithologies.

The regional migration and crystallization of these syntectonic melts as variably deformed sheets and dykes of the Bertibubba Supersuite, located across the Yarlarweelor Gneiss Complex, the Errabiddy Shear Zone, and the Glenburgh Terrane, are coincident with the duration of the $D_{2g}$ event (between 1965 Ma and 1950 Ma; Fig. 18). The youngest age obtained on the Bertibubba Supersuite at c. 1945 Ma (GSWA 142929) is from an undeformed dyke that cuts the $S_{2g}$ fabric in the Nardoo Granite (Occhipinti and Sheppard, 2001). This age indicates that $D_{2g}$ deformation, juxtaposition, and final suturing to form the West Australian Craton was complete by this time.

## <1.94 Ga

Extensive low-grade overprinting of Glenburgh Orogeny fabrics and metamorphic mineral assemblages occurred

throughout the region during the 1820–1770 Ma Capricorn Orogeny. The timing of this event is poorly constrained by direct dating methods because the relatively low grade of metamorphism is generally not conducive to new metamorphic zircon or monazite growth. Nevertheless, two samples from the central and northern belts of the Moogie Metamorphics (GSWA 184160 and 187403; the northern Mooloo Zone and Mutherbukin Zone, respectively) do show some evidence for new zircon growth and complete zircon recrystallization at 1790–1775 Ma (Fig. 18). The main expression of the Capricorn Orogeny in the northern Mooloo Zone and Mutherbukin Zone is contemporaneous with latter stages ($D_{3n}$) of Capricorn orogenesis in the Yarlarweelor Gneiss Complex. This indicates that metamorphism and deformation occurred at different times in different parts of the orogen, possibly in response to different tectonic drivers. Medium-grade metamorphism in the Yarlarweelor Gneiss Complex occurred during the intrusion of discrete, widely distributed granitic sheets, stocks, and plugs (Fig. 1; Sheppard et al., in prep. a) but granite magmatism may have been a response to deformation and metamorphism. Conversely, low-grade tectonometamorphism in the northern Mooloo Zone and Mutherbukin Zone, and medium- to high-grade metamorphism in the Limejuice Zone (Sheppard et al., in prep. a) appear to have been the result of granite magmatism, as these occurrences were synchronous with the intrusion of the bulk of the Minnie Creek batholith (Sheppard et al., in prep. a).

Although the significance of the Capricorn Orogeny with respect to regional- and global-scale plate tectonics is unknown, this event was not the product of continent–continent collision, as the suturing of the Pilbara–Glenburgh and Yilgarn Cratons to form the West Australian Craton occurred during the Glenburgh Orogeny (Sheppard et al., in prep. a.). The geochemistry of the Moorarie Supersuite is consistent with an intraplate setting for magmatism, presumably during some form of intracontinental reworking (Sheppard et al., in prep. a). Subsequent tectonometamorphism during the Meso- and Neoproterozoic, low- to medium-grade events only recorded by xenotime and monazite (e.g. Sheppard et al., 2007; Johnson et al., 2009), occurred within discrete tectonic corridors. These intraplate events are responsible for the broad reorganization of older crustal elements including potential large-scale strike-slip movements on the Errabiddy Shear Zone.

# Conclusions

The pre-collisional siliciclastic basins of the western Capricorn Orogen were deposited in a wide variety of tectonic settings. Each siliciclastic package preserves a unique part of the tectonic history of the region up to, and including, collision of the Pilbara–Glenburgh and Yilgarn Cratons during the Glenburgh Orogeny. SIMS (SHRIMP) dating of detrital zircon components in these packages has provided critical information on their likely source regions, and on the timing of deposition. The growth of new zircon during high-grade metamorphism has provided direct constraints on the timing and duration of metamorphism associated with the Glenburgh Orogeny.

The oldest siliciclastic package is the Moogie Metamorphics, a series of pelitic to psammitic schists with minor quartzite. This package was derived almost entirely from the underlying Halfway Gneiss that makes up part of the Glenburgh Terrane basement. The sediments were deposited sometime between 2240 Ma and 2125 Ma, during the Ophthalmian Orogeny. They were probably deposited in an intracontinental basin, either as a foreland basin or as an extensional back-arc or retro-arc deposit. Some parts may have been subject to a medium-grade metamorphic or hydrothermal event at c. 2125 Ma.

Discontinuous strips of pelitic diatexite within the Paradise Zone were deposited in the fore-arc regions of the proto-Dalgaringa arc between 2080 Ma and 2000 Ma. The sediments were incorporated into the mid to lower crustal portions of the arc, and metamorphosed to granulite facies during the $D_{1g}$ event of the Glenburgh Orogeny, dated in the diatexite by the growth of new metamorphic zircon at c. 1995 Ma. Gneissic granites of the Dalgaringa Supersuite also record this high-grade $D_{1g}$ event, but unlike the diatexite, indicate that it was a prolonged event lasting from 2005 Ma to 1985 Ma.

The Camel Hills Metamorphics comprises two siliciclastic formations, the Quartpot Pelite and the Petter Calc-silicate. The Quartpot Pelite is a series of pelitic to semipelitic schists and gneisses with minor intercalated quartzites. These sediments were derived from an older, currently unexposed part of the proto-Dalgaringa arc during $D_{1g}$ deformation (2005–1985 Ma). The Petter Calc-silicate is mainly a series of calcareous gneisses that were deposited as part of a passive margin sequence along the Yilgarn Craton margin sometime after c. 2610 Ma, but before $D_{2g}$ deformation at 1965–1950 Ma.

$D_{1g}$ metamorphism is only recorded in the Dalgaringa Supersuite, and has been directly dated from metamorphic zircon rims extracted from a granulite facies pelitic diatexite at c. 1995 Ma. However, field relationships suggest that $D_{1g}$ was a protracted event spanning the 2005–1985 Ma period. High-grade metamorphism and deformation associated with the $D_{2g}$ event of the Glenburgh Orogeny occurred throughout the entire region, resulting in the widespread migmatization of pelitic and semipelitic lithologies and the production of near-horizontal gneissic fabrics and foliations. This event is dated directly from both recrystallized and newly grown metamorphic monazite, and low- to very low-Th/U metamorphic zircon overgrowths at 1965–1950 Ma. The regional migration and crystallization of these extensive diatexite melts, as variably deformed sheets and dykes, spanned the entire time period for $D_{2g}$ deformation. These meta-igneous units, known as the Bertibubba Supersuite, intruded across the region from the Glenburgh Terrane to the Yilgarn Craton, and form the first common magmatic element to terranes that were originally on either side of Glenburgh–Yilgarn oceanic tract. Therefore, $D_{2g}$ deformation during the Glenburgh Orogeny was the result of collision assembling the West Australian Craton from a combined Pilbara Craton – Glenburgh Terrane and the Yilgarn Craton — the suture coinciding with the Errabiddy Shear Zone. Subsequent low-grade metamorphism and

deformation during the 1820–1770 Ma Capricorn Orogeny was responsible for the overprinting and retrogression of high-grade fabrics and mineral assemblages associated with the collision.

# References


Ashworth, JR (editor) 1985, Migmatites: Blackie Academic & Professional, Glasgow, UK, 302p.

Blake, TS and Barley, ME 1992, Tectonic evolution of the Late Archaean to Early Proterozoic Mount Bruce megasequence set, Western Australia: Tectonics, v. 11, p. 1415–1425.

Bodorkos, S and Wingate, MTD 2007, The contribution of geochronology to GSWA's mapping programs: current perspectives and future directions, *in* GSWA 2007 extended abstracts: promoting the prospectivity of Western Australia: Geological Survey of Western Australia, Record 2007/2, p. 10–11.

Cawood, PA and Tyler, IM 2004, Assembling and reactivating the Proterozoic Capricorn Orogen: lithotectonic elements, orogenies, and significance: Precambrian Research, v. 128, p. 201–218.

Corfu, F, Hanchar, JM, Hoskin, PWO and Kinny, PD 2003, Atlas of zircon textures, *in* Zircon *edited by* JM Hanchar and PWO Hoskin: Mineralogical Society of America, Reviews in Mineralogy and Geochemistry 53, p. 469–500.

Daniels, JL 1975, Gascoyne Province, *in* Geology of Western Australia: Geological Survey of Western Australia, Memoir 2, p. 107–114.

DeCelles, PG, Ducea, MN, Kapp, P and Zandt, G 2009, Cyclicity in Cordilleran orogenic systems: Nature Geoscience, v. 2, p. 251–257.

Gee, RD 1979, Structure and tectonic style of the Western Australian Shield: Tectonophysics, v. 58, p. 327–369.

Geological Survey of Western Australia 2009, Compilation of geochronology data, June 2009 update: Geological Survey of Western Australia.

Griffin, WL, Wang, X, Jackson, SE, Pearson, NJ, O'Reilly, SY, Xu, X and Zhou, X 2002, Zircon chemistry and magma genesis, SE China: in-situ analysis of Hf isotopes, Pingtan and Tonglu igneous complexes: Lithos, v. 61, p. 237–269.

Johnson, SP, Sheppard, S, Rasmussen, B, Muhling, JR, Fletcher, IR, Wingate, MTD, Kirkland, CL and Pirajno, F 2009, Meso- to Neoproterozoic reworking in the Gascoyne Complex and what it means for mineral exploration, *in* GSWA 2009 extended abstracts: promoting the prospectivity of Western Australia: Geological Survey of Western Australia, Record 2009/2, p. 23–25.

Kinny, PD, Nutman, AP and Occhipinti, SA 2004, Reconnaissance dating of events recorded in the southern part of the Capricorn Orogen: Precambrian Research, v. 128, p. 279–294.

Ludwig, KR 2001, Isoplot/Ex v. 3.0: Berkely Geochronology Centre, Berkely, California.

Martin, DMcB, Li, ZX, Nemchin, AA and Powell, CMcA 1998, A pre-2.2 Ga age for giant hematite ores of the Hamersley Province, Australia: Economic Geology, v. 93, p. 1084–1090.

Martin, DMcB and Thorne, AM 2004, Tectonic setting and basin evolution of the Bangemall Supergroup in the northwestern Capricorn Orogen: Precambrian Research, v. 128, p. 385–409.

Martin, DMcB, Sircombe, KN, Thorne, AM, Cawood, PA and Nemchin, AA 2008, Provenance history of the Bangemall Supergroup and implications for the Mesoproterozoic paleogeography of the West Australian Craton: Precambrian Research, v. 166, p. 93–110.

Menhert, WD 1968, Migmatites and the Origin of Granitic Rocks (1st edition): Elsevier, Amsterdam, The Netherlands, 405p.

Möller, A, O'Brien, PJ, Kennedy, A and Kröner, A 2002, Polyphase zircon in ultrahigh-temperature granulites (Rogaland, SW Norway): constraints for Pb diffusion in zircon: Journal of Metamorphic Geology, v. 20, p. 727–740.

Muhling, JR 1988, The nature of Proterozoic reworking of early Archaean gneisses, Mukalo Creek Area, southern Gascoyne Province, Western Australia: Precambrian Research, v. 40–41 (The Early to Middle Proterozoic of Australia), p. 341–362.

Murakami, T, Chakoumakos, BC, Ewing, RC, Lumpkin, GR and Weber, WJ 1991, Alpha-decay event damage in zircon: American Mineralogist, v. 76, p. 1510–1532.

Occhipinti, SA 2004, Tectonic evolution of the southern Capricorn Orogen, Western Australia: Curtin University of Technology, Perth, Western Australia, PhD thesis (unpublished), 220p.

Occhipinti, SA 2007, Neoproterozoic reworking in the Paleoproterozoic Capricorn Orogen: evidence from 40Ar/39Ar ages: Geological Survey of Western Australia, Record 2007/10, 41p.

Occhipinti, SA and Sheppard, S 2001, Geology of the Glenburgh 1:100 000 sheet: Geological Survey of Western Australia, 1:100 000 Geological Series Explanatory Notes, 37p.

Occhipinti, SA, Sheppard, S, Nelson, DR, Myers, JS and Tyler, IM 1998, Syntectonic granite in the southern margin of the Palaeoproterozoic Capricorn Orogen, Western Australia: Australian Journal of Earth Sciences, v. 45, p. 509–512.

Occhipinti, SA, Sheppard, S, Myers, JS, Tyler, IM and Nelson, DR 2001, Archaean and Palaeoproterozoic geology of the Narryer Terrane (Yilgarn Craton) and southern Gascoyne Complex (Capricorn Orogen), Western Australia — a field guide: Geological Survey of Western Australia, Record 2001/8, 70p.

Occhipinti, SA, Sheppard, S, Passchier, C, Tyler, IM and Nelson, DR 2004, Palaeoproterozoic crustal accretion and collision in the southern Capricorn Orogen: the Glenburgh Orogeny: Precambrian Research, v. 128, p. 237–255.

Occhipinti, SA, Sheppard, S, Cutten, HN and Thorne, AM 2009, Errabiddy, WA Sheet 2347 (2nd edition): Geological Survey of Western Australia, 1:100 000 geological series.

Press, WH, Flannery, BP, Teukolsky, SA and Vetterling, WT 1986, Numerical recipes, the art of scientific computing (1st edition): Cambridge University Press, Cambridge, UK, 818p.

Ramsey, JG and Huber, MI 1987, The techniques of modern structural geology (Volume 2: folds and fractures): Academic Press, London, UK, 392p.

Rasmussen, B, Fletcher, IR and Sheppard, S 2005, Isotopic dating of the migration of a low-grade metamorphic front during orogenesis: Geology, v. 33, p, 773–776.

Reddy, SM and Occhipinti, SA 2004, High-strain zone deformation in the southern Capricorn Orogen, Western Australia: kinematics and age constraints: Precambrian Research, v. 128, p. 295–314.

Rigby, MJ 2009, Conflicting *P–T* paths within the Central Zone of the Limpopo Belt: A consequence of different thermobarometric methods?: Journal of African Earth Sciences, v. 54, p. 111–126.

Sambridge, MS and Compston, W 1994, Mixture modelling of multi-component data sets with application to ion-probe zircon ages: Earth and Planetary Science Letters, v. 128, pp. 373–390.

Schaltegger, U, Fanning, CM, Günther, D, Maurin, JC, Schulmann, K and Gebauer, D 1999, Growth, annealing and recrystallization of zircon and preservation of monazite in high-grade metamorphism: conventional and in-situ U–Pb isotopes, cathodoluminescence and microchemical evidence: Contributions to Mineralogy and Petrology, v. 134, p. 186–201.

Scherer, E, Münker, C and Mezger, K 2001, Calibration of the lutetium–hafnium clock: Science v. 293, p. 683–687.

Schulters, JC and Bohlen, SR 1988, The stability of hercynite and hercynite–gahnite spinels in corundum- or quartz-bearing assemblages: Journal of Petrology, v. 30, p. 1017–1031.

Selway, K 2008, Magnetotelluric investigation into the electrical structure of the Capricorn Orogen, Western Australia: Geological Survey of Western Australia, Record 2007/16, 39p.

Selway, K, Sheppard, S, Thorne, AM, Johnson, SP and Groenewald, PB 2009, Identifying the lithospheric structure of a Precambrian orogen using magnetotellurics: the Capricorn Orogen, Western Australia: Precambrian Research, v. 168, p. 185–196.

Sheppard, S, Bodorkos, S, Johnson, SP, Wingate, MTD and Kirkland, CL in prep. a, The Paleoproterozoic Capricorn Orogeny: a product of intracontinental reworking not continent–continent collision: Geological Survey of Western Australia, Record.

Sheppard, S, Farrell, TR, Martin, DMcB, Thorne, AM and Bagas, L 2008c, Mount Phillips, WA Sheet 2149 (2nd edition): Geological Survey of Western Australia, 1:100 000 geological series.

Sheppard, S, Johnson, SP, Groenewald, PB, Bodorkos, S, Rasmussen, B, Fletcher, IR, Muhling, JR and Selway, K 2008a, Recent advances in our understanding of the Gascoyne Complex, *in* GSWA 2008 extended abstracts: promoting the prospectivity of Western Australia: Geological Survey of Western Australia, Record 2008/2, p. 1–3.

Sheppard, S, Johnson, SP, Groenewald, PB and Farrell, TR 2008b, Yinnetharra, WA Sheet 2148: Geological Survey of Western Australia, 1:100 000 geological series.

Sheppard, S, Johnson, SP, Kirkland, CL, Wingate, MTD and Pirajno, F in prep. b, Explanatory notes for the Gascoyne Province: Geological Survey of Western Australia, Record.

Sheppard, S and Occhipinti, SA 2000, Geology of the Errabiddy and Landor 1:100 000 sheets: Geological Survey of Western Australia, 1:100 000 Geological Series Explanatory Notes, 37p.

Sheppard, S, Occhipinti, SA and Nelson, DR 2005, Intracontinental reworking in the Capricorn Orogen, Western Australia: the 1680–1620 Ma Mangaroon Orogeny: Australian Journal of Earth Sciences, v. 52, p. 443-460.

Sheppard, S, Occhipinti, SA and Tyler, IM 2003, The relationship between tectonism and composition of granitoid magmas, Yarlarweelor Gneiss Complex, Western Australia: Lithos, v. 66, p. 133–154.

Sheppard, S, Occhipinti, SA and Tyler, IM 2004, A 2005–1970 Ma Andean-type batholith in the southern Gascoyne Complex, Western Australia: Precambrian Research, v. 128 Assembling the Palaeoproterozoic Capricorn Orogen, p. 257–277.

Sheppard, S, Rasmussen, B, Muhling, JR, Farrell, TR and Fletcher, IR 2007, Grenvillian-aged orogenesis in the Palaeoproterozoic Gascoyne Complex, Western Australia: 1030–950 Ma reworking of the Proterozoic Capricorn Orogen: Journal of Metamorphic Geology, v. 25, p. 477–494.

Sheppard, S and Swager, CP 1999, Geology of the Marquis 1:100 000 sheet: Geological Survey of Western Australia, 1:100 000 Geological Series Explanatory Notes, 21p.

Sircombe, KN 2003, Age of the Mt Boggola volcanic succession and further geochronological constraint on the Ashburton Basin, Western Australia: Australian Journal of Earth Sciences, v. 50, p. 967–974.

Spear, FS 1993, Metamorphic phase equilibria and pressure–temperature–time paths: Mineralogical Society of America, Monograph, 799p.

Thorne, AM and Seymour, DB 1991, Geology of the Ashburton Basin, Western Australia: Geological Survey of Western Australia, Bulletin 139, 141p.

Trendall, AF 1975, Precambrian: introduction, *in* Geology of Western Australia: Geological Survey of Western Australia, Memoir 2, p. 25–32.

Tyler, IM and Thorne, AM 1990, The northern margin of the Capricorn Orogen, Western Australia — an example of an early Proterozoic collision zone: Journal of Structural Geology, v. 12, p. 685–701.

Williams, SJ 1986, Geology of the Gascoyne Province, Western Australia: Geological Survey of Western Australia, Report 15, 85p.

Appendix 1

# SHRIMP analytical methods and results

## Analytical methods

Zircons were extracted from their host rocks by standard crushing and heavy mineral techniques. After mounting in epoxy, the samples were polished in half, exposing their cores, and imaged under both transmitted and reflected light. All samples* were imaged at Curtin University of Technology using a cathodoluminescence (CL) detector attached to a Phillips XL30 scanning electron microscope with an accelerating voltage of 12 kV. These images were used to identify the various growth stages of the crystal and permit accurate placement of the ion beam within discrete zones. After imaging, the mounts were coated in a thin layer of gold to provide conductivity during the ion probe analyses. The mount was loaded into the sample lock 24 hours prior to analysis and pumped to high vacuum to allow outgassing, thereby minimizing hydride interference during the analysis. Detailed operating procedures, including the results of standards, are given for each sample in the Geochronology Records listed below. The U–Pb age data for all samples was processed (or reprocessed for samples analysed prior to 2003) using recent updates to the SQUID and Isoplot add-ins for Microsoft Excel by Ludwig (2001a,b).

## GSWA sample references

For ease of reading, full references to the individual Geochronology Records for dated samples have not been included in the main text. These references, which can be used for external publication, are listed below.

Also included in this appendix is unpublished data from the recent reanalysis of two of these GSWA samples (Table 1.1). Further information on the methods and conditions of these analyses can be found in Occhipinti (2004).

### Dated samples in this study

**GSWA 142905**
Nelson, DR 1998, 142905: paragneiss, Lucys Bore; Geochronology Record 330: Geological Survey of Western Australia, 4p.

**GSWA 142908**
Nelson, DR 1999, 142908: paragneiss, Erong Springs; Geochronology Record 333: Geological Survey of Western Australia, 4p.

**GSWA 142910**
Nelson, DR 1999, 142910: paragneiss, Pannikan Bore; Geochronology Record 335: Geological Survey of Western Australia, 4p.

**GSWA 168944**
Nelson, DR 2001, 168944: quartz–plagioclase–biotite–muscovite metasandstone, Paperbark Well: Geochronology Record 197; Geological Survey of Western Australia, 4p.

**GSWA 183275**
Kirkland, CL, Wingate, MTD, Bodorkos, S, Sheppard, S and Johnson, SP 2009, 183275: psammitic schist, Mount Dalgety; Geochronology Record 836: Geological Survey of Western Australia, 4p.

**GSWA 184160**
Wingate, MTD, Kirkland, CL, Bodorkos, S and Sheppard, S 2010, 184160: psammitic schist, Weedarrah Homestead; Geochronology Record 863: Geological Survey of Western Australia, 5p.

**GSWA 184161**
Kirkland, CL, Wingate, MTD, Bodorkos, S and Sheppard, S 2009 184161: pelitic migmatite, Mount Dalgety; Geochronology Record 835: Geological Survey of Western Australia, 4p.

**GSWA 187403**
Wingate, MTD, Kirkland, CL, Bodorkos, S, Groenewald, PB and Sheppard, S 2010, 187403: quartzite, Robinson Bore; Geochronology Record 862: Geological Survey of Western Australia, 5p.

**GSWA 185942**
Wingate, MTD, Kirkland, CL, Johnson, SP and Sheppard, S 2010, 185942: pelitic diatexite, Paradise Well; Geochronology Record 861: Geological Survey of Western Australia, 5p.

### Other dated samples mentioned in main text

#### *Yilgarn Craton and Yarlarweelor Gneiss Complex*

**GSWA 139467**
Nelson, DR 2000, 139467: pegmatite-banded monzogranitic gneiss, Black Duck Bore; Geochronology Record 428: Geological Survey of Western Australia, 4p.

**GSWA 142853**
Nelson, DR 1998, 142853: granite gneiss, Jubilee Well rockhole; Geochronology Record 369: Geological Survey of Western Australia, 4p.

**GSWA 142897**
Nelson, DR 1998, 142897: schlieric monzogranite, Jillawarra Bore; Geochronology Record 359: Geological Survey of Western Australia, 4p.

* Initially, the Camel Hills Metamorphic samples (GSWA 142905, 142908, 142910, and 168944) were dated without the aid of CL or BSE images. However, these mounts were recently imaged using CL to better interpret the U–Pb data.

**Table 1.1. SHRIMP U–Pb data for detrital zircons analysed by Occhipinti (2004)**

| *Grain spot* | *Domain* | *U (ppm)* | *Th (ppm)* | *Th/U* | *f204 (%)* | $^{238}U/^{206}Pb^*$ | (±1σ) | $^{207}Pb^*/^{206}Pb^*$ | (±1σ) | $^{238}U^*/^{206}Pb^*$ age (Ma) | (±1σ) | $^{207}Pb^*/^{206}Pb^*$ age (Ma) | (±1σ) | *Discordance (%)* |
|---|---|---|---|---|---|---|---|---|---|---|---|---|---|---|
| **GSWA 142910** | | | | | | | | | | | | | | |
| S1.1 | rim | 733 | 9 | 0.01 | 0.080 | 2.825 | 0.047 | 0.11980 | 0.00029 | 1954 | 28 | 1953 | 4 | 0.0 |
| S1.2 | core | 280 | 218 | 0.78 | 0.060 | 2.698 | 0.046 | 0.12560 | 0.00048 | 2033 | 30 | 2037 | 7 | 0.3 |
| S2.1 | rim | 975 | 14 | 0.01 | 1.220 | 2.845 | 0.048 | 0.12960 | 0.00083 | 1942 | 28 | 2093 | 11 | 7.3 |
| S2.2 | core | 229 | 203 | 0.89 | 1.650 | 2.197 | 0.038 | 0.18020 | 0.00062 | 2418 | 35 | 2655 | 6 | 8.9 |
| S3.1 | core | 539 | 119 | 0.22 | 2.440 | 2.723 | 0.046 | 0.14630 | 0.00158 | 2011 | 29 | 2303 | 18 | 12.7 |
| S3.2 | rim | 785 | 10 | 0.01 | 0.060 | 2.822 | 0.048 | 0.12010 | 0.00029 | 1956 | 29 | 1958 | 4 | 0.2 |
| S3.3 | rim | 789 | 14 | 0.02 | 0.430 | 2.849 | 0.047 | 0.12330 | 0.00029 | 1939 | 28 | 2005 | 4 | 3.3 |
| S4.1 | rim | 1161 | 29 | 0.02 | 0.090 | 2.701 | 0.045 | 0.12620 | 0.00189 | 2031 | 29 | 2046 | 26 | 0.8 |
| S4.2 | core | 545 | 88 | 0.16 | 0.030 | 2.330 | 0.039 | 0.14480 | 0.00042 | 2302 | 32 | 2285 | 5 | -0.7 |
| S5.1 | rim | 705 | 10 | 0.01 | 0.070 | 2.848 | 0.047 | 0.11980 | 0.00030 | 1940 | 28 | 1953 | 4 | 0.7 |
| S5.2 | core | 335 | 268 | 0.80 | 0.440 | 2.692 | 0.048 | 0.12840 | 0.00045 | 2037 | 31 | 2076 | 6 | 2.0 |
| S6.1 | rim | 1910 | 298 | 0.16 | 0.240 | 2.689 | 0.045 | 0.12880 | 0.00019 | 2038 | 29 | 2082 | 3 | 2.1 |
| S6.2 | core | 372 | 302 | 0.81 | 5.110 | 3.062 | 0.053 | 0.17270 | 0.00120 | 1822 | 28 | 2584 | 12 | 29.5 |
| S8.1 | rim | 751 | 30 | 0.04 | 2.360 | 2.909 | 0.055 | 0.13400 | 0.00278 | 1905 | 31 | 2151 | 36 | 11.5 |
| S9.1 | rim | 634 | 250 | 0.39 | 1.670 | 2.825 | 0.048 | 0.13960 | 0.00068 | 1954 | 29 | 2222 | 8 | 12.1 |
| S10.1 | rim | 882 | 11 | 0.01 | 0.030 | 2.854 | 0.048 | 0.11960 | 0.00032 | 1937 | 28 | 1950 | 5 | 0.8 |
| S10.2 | core | 401 | 152 | 0.38 | 0.460 | 2.836 | 0.048 | 0.12750 | 0.00042 | 1947 | 29 | 2064 | 6 | 5.7 |
| S11.1 | rim | 956 | 81 | 0.08 | 0.080 | 2.848 | 0.047 | 0.12120 | 0.00027 | 1940 | 28 | 1974 | 4 | 1.8 |
| S12.1 | core | 485 | 110 | 0.23 | 1.420 | 2.612 | 0.045 | 0.15910 | 0.00235 | 2089 | 31 | 2446 | 25 | 14.6 |
| S13.1 | core | 331 | 234 | 0.71 | 0.510 | 2.203 | 0.037 | 0.16790 | 0.00074 | 2413 | 34 | 2537 | 7 | 4.9 |
| S13.2 | core | 286 | 118 | 0.41 | 1.510 | 2.558 | 0.044 | 0.19380 | 0.00067 | 2128 | 31 | 2775 | 6 | 23.4 |
| S14.1 | core | 626 | 168 | 0.27 | 0.470 | 2.600 | 0.044 | 0.13870 | 0.00038 | 2098 | 30 | 2211 | 5 | 5.2 |
| S15.1 | core | 85 | 20 | 0.24 | 0.250 | 2.184 | 0.050 | 0.16110 | 0.00124 | 2430 | 47 | 2467 | 13 | 1.5 |
| **GSWA 168944** | | | | | | | | | | | | | | |
| S1r | rim | 918 | 118 | 0.13 | 0.38 | 2.729 | 0.045 | 0.12550 | 0.00072 | 2012 | 29 | 2036 | 10 | 1.2 |
| S2r | rim | 430 | 82 | 0.19 | 0.94 | 2.243 | 0.038 | 0.15300 | 0.00215 | 2377 | 34 | 2380 | 24 | 0.2 |
| S3c | core | 504 | 522 | 1.04 | 1.23 | 2.732 | 0.049 | 0.12400 | 0.00216 | 2011 | 31 | 2014 | 31 | 0.2 |
| S4c | core | 294 | 256 | 0.87 | 0.15 | 2.752 | 0.047 | 0.12430 | 0.00058 | 1998 | 29 | 2018 | 8 | 1.0 |
| S5c | core | 377 | 536 | 1.42 | 0.09 | 2.855 | 0.048 | 0.12440 | 0.00060 | 1936 | 28 | 2020 | 9 | 4.2 |
| S6r | rim | 254 | 137 | 0.54 | 6.69 | 1.949 | 0.033 | 0.17380 | 0.01125 | 2670 | 37 | 2594 | 108 | -2.9 |
| S7c | core | 86 | 44 | 0.51 | 0.12 | 2.587 | 0.048 | 0.12440 | 0.00093 | 2107 | 33 | 2020 | 13 | -4.3 |
| S8c | core | 90 | 48 | 0.53 | 23.81 | 1.766 | 0.032 | 0.17160 | 0.03686 | 2893 | 42 | 2573 | 359 | -12.4 |

**NOTE:** *f*204 (%) is fraction of common $^{206}Pb$ in total measured $^{206}Pb$, as estimated using measured $^{204}Pb/^{206}Pb$
Pb* = radiogenic Pb
Discordance (%) = 100*(1-[($^{238}U/^{206}Pb$ date)-($^{207}Pb/^{206}Pb$ date)]/($^{207}Pb/^{206}Pb$ date))

**GSWA 142906**
Nelson, DR 1998, 142906: coarse porphyritic monzogranite, Beedarry Bore; Geochronology Record 331: Geological Survey of Western Australia, 4p.

### *Halfway Gneiss*

**GSWA 142988**
Nelson, DR 2000, 142988: biotite tonalite, Dunnawah Bore; Geochronology Record 291: Geological Survey of Western Australia, 4p.

**GSWA 164309**
Nelson, DR 2000, 164309: foliated porphyritic biotite granodiorite, Middle Well; Geochronology Record 217: Geological Survey of Western Australia, 4p.

**GSWA 168950**
Nelson, DR 2001, 168950: pegmatite-banded biotite tonalite gneiss, Yanderra Well; Geochronology Record 188: Geological Survey of Western Australia, 4p.

### *Dalgaringa Supersuite*

**GSWA 142923**
Nelson, DR 1999, 142923: foliated biotite monzogranite, Glenburgh Homestead; Geochronology Record 343: Geological Survey of Western Australia, 4p.

**GSWA 142933**
Nelson, DR 1999, 142933: biotite–hypersthene–clinopyroxene–andesine mafic granulite, Meerawana Bore; Geochronology Record 320: Geological Survey of Western Australia, 4p.

**GSWA 168949**
Nelson, DR 2001, 168949: porphyritic biotite–muscovite monzogranite, Killoran Bore; Geochronology Record 187: Geological Survey of Western Australia, 4p.

**GSWA 168951**
Nelson, DR 2001, 168951: foliated biotite–muscovite monzogranite, Salt Well; Geochronology Record 189: Geological Survey of Western Australia, 4p.

### *Bertibubba Supersuite*

**GSWA 142929**
Nelson, DR 1999, 142929: biotite trondhjemite dyke, Nardoo Bore; Geochronology Record 316: Geological Survey of Western Australia, 4p.

**GSWA 142850**
Nelson, DR 1999, 142850: foliated monzogranite, Nanular Bore; Geochronology Record 366: Geological Survey of Western Australia, 4p.

**GSWA 142909**
Nelson, DR 1999, 142909: biotite trondhjemite, Quartpot Bore; Geochronology Record 334: Geological Survey of Western Australia, 4p.

### *Ashburton Basin*

**GSWA 169084**
Nelson, DR 2004, 169084: ferruginous sandstone, Miringee Well; Geochronology Record 43: Geological Survey of Western Australia, 5p.

## Other references

Ludwig, KR 2001a, SQUID 2.22: A user's manual: Berkeley Geochronology Center, Special Publication 2, 16p.

Ludwig, KR 2001b, Users manual for Isoplot/Ex v. 3.0: A geochronological toolkit for Microsoft Excel: Berkeley Geochronology Center, Special Publication 1a, 56p.

Occhipinti, SA 2004, Tectonic evolution of the southern Capricorn Orogen, Western Australia: Curtin University of Technology, Perth, Western Australia, PhD thesis (unpublished), 220p.

**Appendix 2**

# Zircon crystallinity and detrital zircon statistical analyses

## Zircon crystallinity

The alpha-radiation dosage a crystal has been subjected to can be calculated based on age, uranium and thorium concentration, Avogadro's number, and the decay rates of $^{238}U$, $^{235}U$, and $^{232}Th$ (Murakami et al., 1991). Furthermore, this is related to the crystal density. Murakami et al. (1991) defined grains with alpha events $<3 \times 10^{-15}$ as crystalline, $>3 \times 10^{-15}$ to $<8 \times 10^{-15}$ as intermediate, and $>8 \times 10^{-15}$ as metamict. Results are tabulated in Table 2.1.

## K–S test

In detrital zircon studies, comparisons of age spectra are generally based on visual observation, either as histograms, probability distribution diagrams, or combined figures; however, issues of bin size and the difficulty of looking across numerous plots presents a significant challenge. For comparison across multiple samples a better solution is to quantify the strength of similarity, hence removing the subjective nature of the visual assessment. Detrital zircon populations have been mathematically described in the past (e.g. Gehrels, 2000), and a range of statistical techniques are available to quantify the similarity between samples (Sircombe, 2000; Sircombe and Hazelton, 2004), including methods using both the empirical distribution and a Kernel density estimation. In this study we use an empirical method — the Kolmogorov–Smirnov (K–S) test (Press et al., 1986) — to compare the age distribution of various detrital zircon populations. A powerful tool used to elucidate subtle relationships in detrital populations (Berry et al., 2001; Kirkland et al., 2008), the K–S test is a non parametric statistical method, which mathematically compares distributions and determines if there is a significant difference between populations. It tests the null hypothesis that the distributions come from the same parent population. To apply the K–S test, the grain-age data are first recast as a cumulative function, that is, the number of observations with a given age or less. Then the observed difference (D) is found, defined as the maximum probability difference between cumulative density curves. If this observed difference is greater than the critical value, the null hypothesis is rejected and the two samples most likely did not come from the same population. Critical values of D are found in Massey (1951). Probability values may also be calculated where the value $(1-p)$ represents the probability that the two samples have different distributions. We reject the hypothesis that two samples come from the same source when the probability $(p)$ drops below 0.05, indicating that we have 95% confidence that the samples are different. High values, close to 1.0, indicate very similar age spectra.

For the purposes of this study, the detrital zircon populations of the Camel Hills and Moogie Metamorphics were compared with the ages of magmatic and inherited zircons extracted from the potential basement sources including the Halfway Gneiss, the northern Yilgarn Craton and the Yarlarweelor Gneiss Complex. The results are listed in Table 2 (main text). Here, all four currently dated and published samples of the Halfway Gneiss were used as a comparison. Two samples from the northern Yilgarn Craton (GSWA 142906 and 142897), and a reworked example from the Errabiddy Shear Zone (GSWA 139467) were selected for their proximity to the Gascoyne Province and because they contained a large number of inherited zircons with well-defined age components. A single sample from the Yarlarweelor Gneiss Complex (GSWA 142853) was also chosen, again due to its proximity to the Gascoyne Province and the large number of inherited zircons. Other samples yielded similar results, but correlations were not so well defined due to the lower numbers of inherited zircons.

## References

Berry, RF, Jenner, GA, Meffre, S and Tubrett, MN 2001, A North American provenance for Neoproterozoic to Cambrian sandstones in Tasmania?: Earth and Planetary Science Letters, v. 192, p. 207–222.

Gehrels, GE 2000, Introduction to detrital zircon studies of Paleozoic and Triassic strata in western Nevada and northern California, *in* Paleozoic and Triassic Paleogeography and Tectonics of Western Nevada and Northern California *edited by* MJ Soreghan and GE Gehrels: Geological Society of America, Special Paper 347, p. 1–17.

Kirkland, CL, Strachan, RA and Prave, T 2008, Detrital zircon signature of the Moine Supergroup, Scotland: Contrasts and comparisons with other Neoproterozoic successions within the circum–North Atlantic region: Precambrian Research, v. 163, p. 332–350.

Massey Jr, FJ 1951, The Kolmogorov–Smirnov test of goodness of fit: Journal of the American Statistical Association, v. 46, p. 68–78.

Murakami, T, Chakoumakos, BC, Ewing, RC, Lumpkin, GR and Weber, WJ 1991, Alpha-decay event damage in zircon: American Mineralogist, v. 76, p. 1510–1532.

Press, WH, Flannery, BP, Teukolsky, SA and Vetterling, WT 1986, Numerical Recipes, the Art of Scientific Computing: Cambridge University Press, Cambridge, 818p.

Sircombe, KN 2000, Quantitative comparison of large sets of geochronological data using multivariate analysis: a provenance study example from Australia: Geochimica et Cosmochimica Acta, v. 64, p. 1593–1616.

Sircombe, KN and Hazelton, ML 2004, Comparison of detrital zircon age distributions by kernel functional estimation: Sedimentary Geology, v. 171, p. 91–111.

**Table 2.1. Calculated density values for detrital zircon from samples of the Quartpot Pelite**

| *Sample* | *Analysis no.* | *U (ppm)* | *Th (ppm)* | *f204 (%)* | *$^{238}U/^{206}Pb$* | *(±1σ)* | *$^{207}Pb/^{206}Pb$* | *(±1σ)* | *$^{207}Pb/^{206}Pb$ age (Ma)* | *(±1σ)* | *Discordance (%)* | *Metamict stage* | *Density (g/cm³)* |
|---|---|---|---|---|---|---|---|---|---|---|---|---|---|
| 142910 | s3.3* | 789 | 14 | 0.43 | 2.849 | 0.047 | 0.12330 | 0.00029 | 2005 | 4 | 3 | II: intermediate | 4.22 |
| | 7.1 | 500 | 179 | 0.06 | 2.686 | 0.052 | 0.12431 | 0.00048 | 2019 | 7 | -1 | II: intermediate | 4.37 |
| | 17.1 | 550 | 217 | 0.05 | 2.763 | 0.083 | 0.12432 | 0.00046 | 2019 | 7 | 1 | II: intermediate | 4.33 |
| | 21.1 | 297 | 171 | 0.29 | 2.756 | 0.083 | 0.12467 | 0.00071 | 2024 | 10 | 1 | I: crystalline | 4.54 |
| | 26.1 | 312 | 248 | 0.21 | 2.844 | 0.086 | 0.12470 | 0.00074 | 2025 | 10 | 4 | I: crystalline | 4.51 |
| | 24.1 | 212 | 173 | 0.09 | 2.750 | 0.083 | 0.12543 | 0.00080 | 2035 | 11 | 2 | I: crystalline | 4.60 |
| | 8.1 | 323 | 372 | 0.50 | 2.731 | 0.053 | 0.12550 | 0.00077 | 2036 | 11 | 1 | II: intermediate | 4.48 |
| | s1.2* | 280 | 218 | 0.06 | 2.698 | 0.046 | 0.12560 | 0.00048 | 2037 | 7 | 0 | I: crystalline | 4.54 |
| | 7.2 | 230 | 128 | 0.32 | 2.808 | 0.084 | 0.12570 | 0.00080 | 2039 | 11 | 4 | I: crystalline | 4.60 |
| | 1.1 | 297 | 162 | 0.00 | 2.756 | 0.053 | 0.12608 | 0.00058 | 2044 | 8 | 2 | I: crystalline | 4.53 |
| | s4.1* | 1161 | 29 | 0.09 | 2.701 | 0.0445 | 0.12620 | 0.00189 | 2046 | 26 | 1 | III: highly metamict | 4.08 |
| | 3.1 | 361 | 161 | 0.10 | 2.805 | 0.054 | 0.12631 | 0.00060 | 2047 | 8 | 4 | II: intermediate | 4.48 |
| | s10.2* | 401 | 152 | 0.46 | 2.836 | 0.048 | 0.12750 | 0.00042 | 2064 | 6 | 6 | II: intermediate | 4.45 |
| | 22.1 | 729 | 29 | 0.05 | 2.685 | 0.081 | 0.12759 | 0.00035 | 2065 | 5 | 1 | II: intermediate | 4.23 |
| | s5.2* | 335 | 268 | 0.44 | 2.692 | 0.0478 | 0.12840 | 0.00045 | 2076 | 6 | 2 | II: intermediate | 4.48 |
| | 18.1 | 548 | 206 | 0.40 | 2.782 | 0.084 | 0.12873 | 0.00057 | 2081 | 8 | 5 | II: intermediate | 4.32 |
| | 9.1 | 474 | 35 | 0.06 | 2.729 | 0.082 | 0.12879 | 0.00052 | 2082 | 7 | 3 | II: intermediate | 4.40 |
| | s6.1* | 1910 | 298 | 0.24 | 2.689 | 0.045 | 0.12880 | 0.00019 | 2082 | 3 | 2 | III: highly metamict | 4.01 |
| | 14.1 | 356 | 177 | 0.79 | 2.733 | 0.082 | 0.12972 | 0.00087 | 2094 | 12 | 4 | II: intermediate | 4.47 |
| 142905 | 8.1 | 222 | 159 | 0.34 | 2.710 | 0.027 | 0.12287 | 0.00096 | 1998 | 14 | -1 | I: crystalline | 4.60 |
| | 25.1 | 136 | 104 | 0.28 | 2.694 | 0.028 | 0.12383 | 0.00127 | 2012 | 18 | -1 | I: crystalline | 4.67 |
| | 11.1 | 512 | 455 | 0.04 | 2.784 | 0.026 | 0.12591 | 0.00052 | 2042 | 7 | 3 | II: intermediate | 4.32 |
| | 17.1 | 116 | 153 | 0.30 | 2.690 | 0.028 | 0.12617 | 0.00136 | 2045 | 19 | 0 | I: crystalline | 4.68 |
| | 9.1 | 618 | 80 | 0.05 | 2.630 | 0.025 | 0.12619 | 0.00046 | 2046 | 6 | -2 | II: intermediate | 4.30 |
| | 10.1 | 316 | 258 | 0.08 | 2.746 | 0.027 | 0.12629 | 0.00071 | 2047 | 10 | 2 | II: intermediate | 4.50 |
| | 23.1 | 250 | 135 | 0.15 | 2.686 | 0.027 | 0.12628 | 0.00080 | 2047 | 11 | 0 | I: crystalline | 4.58 |
| | 5.1 | 1085 | 271 | 0.05 | 2.725 | 0.026 | 0.12633 | 0.00036 | 2048 | 5 | 2 | III: highly metamict | 4.08 |
| | 26.1 | 492 | 128 | 0.13 | 2.734 | 0.026 | 0.12643 | 0.00058 | 2049 | 8 | 2 | II: intermediate | 4.38 |
| | 7.1 | 201 | 236 | 0.14 | 2.676 | 0.027 | 0.12698 | 0.00095 | 2057 | 13 | 1 | I: crystalline | 4.60 |
| | 6.1 | 154 | 378 | 0.24 | 2.680 | 0.028 | 0.12752 | 0.00112 | 2064 | 16 | 1 | I: crystalline | 4.62 |
| | 16.1 | 725 | 77 | 0.18 | 2.701 | 0.026 | 0.12767 | 0.00049 | 2066 | 7 | 2 | II: intermediate | 4.23 |
| | 4.1 | 113 | 84 | 0.41 | 2.746 | 0.029 | 0.12800 | 0.00143 | 2071 | 20 | 3 | I: crystalline | 4.69 |
| | 1.1 | 92 | 90 | 0.14 | 2.687 | 0.030 | 0.12812 | 0.00146 | 2072 | 20 | 2 | I: crystalline | 4.70 |
| | 20.1 | 414 | 135 | 0.96 | 2.723 | 0.027 | 0.12857 | 0.00090 | 2079 | 12 | 3 | II: intermediate | 4.43 |
| | 21.1 | 236 | 49 | 1.66 | 2.659 | 0.027 | 0.12878 | 0.00146 | 2081 | 20 | 1 | I: crystalline | 4.60 |
| | 15.1 | 454 | 140 | 0.14 | 2.636 | 0.026 | 0.12912 | 0.00059 | 2086 | 8 | 1 | II: intermediate | 4.40 |
| | 3.1 | 178 | 153 | 0.34 | 2.588 | 0.026 | 0.12964 | 0.00108 | 2093 | 15 | -1 | I: crystalline | 4.63 |
| 168944 | 25.1 | 188 | 107 | 0.13 | 2.757 | 0.033 | 0.12198 | 0.00095 | 1985 | 14 | -1 | I: crystalline | 4.64 |
| | 31.1 | 300 | 147 | 0.01 | 2.706 | 0.031 | 0.12384 | 0.00064 | 2012 | 9 | -1 | I: crystalline | 4.54 |
| | s3c* | 504 | 522 | 1.23 | 2.732 | 0.049 | 0.12400 | 0.00216 | 2014 | 31 | 1 | II: intermediate | 4.32 |
| | 16.1 | 158 | 138 | 0.08 | 2.709 | 0.032 | 0.12410 | 0.00096 | 2016 | 14 | -1 | I: crystalline | 4.65 |
| | 23.1 | 138 | 72 | 0.11 | 2.664 | 0.033 | 0.12413 | 0.00120 | 2016 | 17 | -2 | I: crystalline | 4.68 |

**Table 2.1.** (continued)**e**

| *Sample* | *Analysis no.* | *U (ppm)* | *Th (ppm)* | *f204 (%)* | *$^{238}U/^{206}Pb$* | *(±1σ)* | *$^{207}Pb/^{206}Pb$* | *(±1σ)* | *$^{207}Pb/^{206}Pb$ age (Ma)* | *(±1σ)* | *Discordance (%)* | *Metamict stage* | *Density (g/cm³)* |
|---|---|---|---|---|---|---|---|---|---|---|---|---|---|
| | 5.1 | 293 | 263 | 0.04 | 2.753 | 0.033 | 0.12419 | 0.00070 | 2017 | 10 | 1 | I: crystalline | 4.53 |
| | 19.1 | 394 | 192 | 0.08 | 2.757 | 0.032 | 0.12415 | 0.00059 | 2017 | 8 | 1 | II: intermediate | 4.45 |
| | s4c* | 294 | 256 | 0.15 | 2.752 | 0.0467 | 0.12430 | 0.00058 | 2018 | 8 | 1 | I: crystalline | 4.53 |
| | 4.1 | 298 | 263 | 0.00 | 2.732 | 0.032 | 0.12441 | 0.00063 | 2020 | 9 | 1 | I: crystalline | 4.52 |
| | s5c* | 377 | 536 | 0.09 | 2.855 | 0.048 | 0.12440 | 0.00060 | 2020 | 9 | 4 | II: intermediate | 4.41 |
| | s7c* | 86 | 44 | 0.12 | 2.587 | 0.048 | 0.12440 | 0.00093 | 2020 | 13 | -4 | I: crystalline | 4.71 |
| | 9.1 | 738 | 736 | 0.38 | 2.712 | 0.031 | 0.12487 | 0.00052 | 2027 | 7 | 0 | II: intermediate | 4.17 |
| | 17.1 | 346 | 184 | 0.02 | 2.747 | 0.032 | 0.12489 | 0.00067 | 2027 | 10 | 1 | II: intermediate | 4.49 |
| | 10.1 | 216 | 155 | 0.08 | 2.703 | 0.032 | 0.12513 | 0.00081 | 2031 | 11 | 0 | I: crystalline | 4.60 |
| | 1.1 | 382 | 111 | 0.54 | 2.634 | 0.031 | 0.12520 | 0.00081 | 2032 | 12 | -2 | II: intermediate | 4.47 |
| | 7.1 | 1608 | 767 | 0.03 | 2.785 | 0.032 | 0.12523 | 0.00028 | 2032 | 4 | 3 | III: highly metamict | 4.02 |
| | 8.1 | 344 | 213 | 0.19 | 2.731 | 0.032 | 0.12523 | 0.00071 | 2032 | 10 | 1 | II: intermediate | 4.49 |
| | 13.1 | 308 | 149 | 0.00 | 2.656 | 0.031 | 0.12520 | 0.00062 | 2032 | 9 | -1 | I: crystalline | 4.53 |
| | 14.1 | 165 | 134 | 1.10 | 2.674 | 0.032 | 0.12523 | 0.00153 | 2032 | 22 | -1 | I: crystalline | 4.65 |
| | S1r* | 918 | 118 | 0.38 | 2.729 | 0.045 | 0.12550 | 0.00072 | 2036 | 10 | 2 | II: intermediate | 4.14 |
| | 3.1 | 160 | 122 | 0.09 | 2.692 | 0.033 | 0.12578 | 0.00107 | 2040 | 15 | 0 | I: crystalline | 4.65 |
| | 28.1 | 315 | 207 | 0.01 | 2.688 | 0.031 | 0.12577 | 0.00070 | 2040 | 10 | 0 | I: crystalline | 4.51 |
| | 30.1 | 216 | 100 | 0.03 | 2.739 | 0.032 | 0.12629 | 0.00092 | 2047 | 13 | 2 | I: crystalline | 4.61 |
| | 22.1 | 95 | 93 | -0.05 | 2.757 | 0.035 | 0.12669 | 0.00190 | 2053 | 26 | 3 | I: crystalline | 4.70 |
| | 15.1 | 256 | 176 | 0.02 | 2.685 | 0.032 | 0.12829 | 0.00069 | 2075 | 9 | 2 | I: crystalline | 4.56 |

**NOTES:** Analysis numbers beginning with 's' are from Occhipinti (2004); r = rim, c = core. Other data referenced in Appendix 1
*f*204 is fraction of common $^{206}Pb$ in total measured $^{206}Pb$, as estimated using measured $^{204}Pb/^{206}Pb$
Density values are calculated according to Murakami et al. (1991)

**Appendix 3**

# In situ SHRIMP monazite and zircon geochronology

## Sample identi cation and characterization

Thick (~30 μm) polished sections were made of three pelitic schist samples (GSWA 164333, 164369, and 168713). These sections were examined by optical microscope and a Jeol JSM 6400 scanning electron microscope (SEM) equipped with an Oxford LINK energy dispersive X-ray spectrometer (EDS), located in the Centre for Microscopy, Characterisation and Analysis (CMCA) at the University of Western Australia (UWA). Element mapping of monazite from two samples (GSWA 164369, 168713) was carried out by electron microprobe in order to identify compositional zoning. X-ray element maps for thorium, yttrium, and lanthanum were collected and processed using an automated Jeol JSM6400 SEM fitted with three wavelength dispersive crystal spectrometers. Operating conditions were 20 kV accelerating voltage and 100 nA beam current. Synthetic phosphates and glasses, and natural minerals, were used as standards. Counting times were 50 ms per pixel.

## In situ SHRIMP U–Pb dating

Monazite and zircon crystals that were sufficiently large (>15 μm) for dating by sensitive high resolution ion microprobe (SHRIMP) were drilled from polished thin sections as ~3 mm discs and cast in 25 mm diameter epoxy mounts. In situ U–Th–Pb isotopic analyses were carried out using the SHRIMP II ion microprobe at the John de Laeter Centre of Mass Spectrometry at Curtin University of Technology. Analytical procedures followed established methodologies for monazite (Kinny, 1997; Foster et al., 2000; Rasmussen et al., 2001) using a ~0.25 nA $O_2^-$ ion beams focussed onto ≤10 μm spots. Monazite standards were set in separate mounts that were gold-coated with the sample mounts. The $^{207}Pb/^{206}Pb$ reference standard, required due to the use of the retardation lens, was GSC 2908 (provided by R. Stern, Geoscience Australia). The Pb/U calibration was based on MAD-1 (514 Ma; Foster et al., 2000). Monazite data were processed using Krill software (written by P. Kinny, Curtin University of Technology). Corrections for matrix effects in Pb/U (from uranium and thorium) relied on data from GSC 2908, QMa 28-1 and PD-95 and were carried out separately on spreadsheet templates.

For zircon, chips of the CZ3 zircon U/Pb standard (564 Ma; Pidgeon et al., 1994; Nelson, 1994) were cast in the same mount as the zircon-bearing discs. Zircon analyses followed established procedures. A 30 μm Köhler aperture was used to achieve a primary beam current of ~0.3 nA in a <10 μm diameter spot. Data were reduced using Squid-1 and Isoplot/Ex software (Ludwig, 2001a,b). SHRIMP data are listed in Tables 3.1–4.

## References


Foster, G, Kinny, P, Vance, D, Prince, C and Harris, N 2000, The significance of monazite U–Th–Pb age data in metamorphic assemblages: a combined study of monazite and garnet chronometry: Earth and Planetary Science Letters, v. 181, p. 327–340.

Kinny, PD 1997, Users guide to U–Th–Pb dating of titanate, perovskite, monazite and baddeleyite using the WA SHRIMP: Curtin University of Technology, Perth.

Ludwig, KR 2001a, SQUID 2.22: A user's manual: Berkeley Geochronology Center, Special Publication 2, 16p.

Ludwig, KR 2001b, Users manual for Isoplot/Ex rev. 3.0: A geochronological toolkit for Microsoft Excel: Berkeley Geochronology Center, Special Publication 1a, 56p.

Nelson, DR 1997, Compilation of SHRIMP U–Pb zircon geochronology data, 1996: Geological Survey of Western Australia, Record 1997/2, 189 p.

Pidgeon, RT, Furfaro, D, Kennedy, AK, Nemchin, AA and van Bronswik, W 1994, Calibration of zircon standards for the Curtin SHRIMP II: United States Geological Survey; Eighth International Conference on Geochronology, Cosmochronology, and Isotope Geology, Berkeley, USA, Abstracts; Circular, no. 1107, p. 251.

Rasmussen, B, Fletcher, IR and McNaughton, NJ 2001, Dating low-grade metamorphic events by SHRIMP U–Pb analysis of monazite in shales: Geology, v. 29, p. 963–966.

Stacey, JS and Kramers, JD 1975, Approximation of terrestrial lead isotope evolution by a two-stage model: Earth and Planetary Science Letters, v. 26, p. 207–221.

**Table 3.1. In situ SHRIMP U–Pb data for monazite in GSWA 164333**

| *Analysis* | *U (ppm)* | *Th (ppm)* | *Th/U* | *f204 (%)* | $^{207}Pb^*/^{206}Pb^*$ | *(±1σ)* | $^{206}Pb^*/^{238}U$ | *(±1σ)* | $^{207}Pb^*/^{235}U$ | *(±1σ)* | $^{208}Pb^*/^{232}Th$ | *(±1σ)* | *Disc. (%)* | $^{07}Pb^*/^{206}Pb^*$ *age (Ma)* | *(±1σ)* |
|---|---|---|---|---|---|---|---|---|---|---|---|---|---|---|---|
| *All data, in grain sequence* | | | | | | | | | | | | | | | |
| 0706A.1–1 | 16957 | 58584 | 3.5 | 0.015 | 0.1186 | 0.0004 | 0.3606 | 0.0090 | 5.898 | 0.151 | 0.1066 | 0.0025 | -3 | 1936 | 6 |
| 0706A.2–1 | 12977 | 51696 | 4.0 | 0.011 | 0.1168 | 0.0003 | 0.3531 | 0.0087 | 5.685 | 0.142 | 0.1057 | 0.0025 | -2 | 1908 | 4 |
| 0706B.1–1 | 7771 | 66372 | 8.5 | 0.031 | 0.1194 | 0.0005 | 0.3582 | 0.0089 | 5.898 | 0.151 | 0.1089 | 0.0026 | -1 | 1948 | 7 |
| 0706C.1–1 | 10899 | 41512 | 3.8 | 0.010 | 0.1174 | 0.0003 | 0.3530 | 0.0087 | 5.713 | 0.142 | 0.1093 | 0.0025 | -2 | 1917 | 4 |
| 0706D.1–1 | 3552 | 66120 | 18.6 | 0.016 | 0.1196 | 0.0005 | 0.3553 | 0.0089 | 5.859 | 0.152 | 0.1082 | 0.0025 | 0 | 1950 | 7 |
| 0706E.1–1 | 12346 | 53786 | 4.4 | 0.009 | 0.1133 | 0.0003 | 0.3391 | 0.0084 | 5.297 | 0.133 | 0.0997 | 0.0023 | -2 | 1853 | 4 |
| 0706E.2–1 | 14045 | 58487 | 4.2 | 0.025 | 0.1163 | 0.0003 | 0.3519 | 0.0088 | 5.641 | 0.142 | 0.1019 | 0.0024 | -2 | 1899 | 4 |
| 0706E.3–1 | 3402 | 53834 | 15.8 | 0.055 | 0.1204 | 0.0006 | 0.3500 | 0.0090 | 5.810 | 0.155 | 0.1092 | 0.0025 | 1 | 1962 | 9 |
| 0706F.1–1 | 10375 | 51353 | 4.9 | 0.058 | 0.1149 | 0.0004 | 0.3487 | 0.0087 | 5.523 | 0.140 | 0.1036 | 0.0024 | -3 | 1878 | 6 |
| 0706F.1–2 | 13253 | 52020 | 3.9 | 0.004 | 0.1173 | 0.0003 | 0.3580 | 0.0089 | 5.790 | 0.146 | 0.1056 | 0.0025 | -3 | 1916 | 5 |
| 0706G.1–1 | 3416 | 35779 | 10.5 | 0.019 | 0.1195 | 0.0004 | 0.3714 | 0.0092 | 6.121 | 0.156 | 0.1107 | 0.0026 | -4 | 1949 | 7 |
| 0706H.1–1 | 11921 | 54525 | 4.6 | 0.022 | 0.1126 | 0.0003 | 0.3322 | 0.0082 | 5.156 | 0.130 | 0.0977 | 0.0023 | 0 | 1842 | 5 |
| 0706I.1–1 | 11040 | 60756 | 5.5 | 0.044 | 0.1168 | 0.0003 | 0.3516 | 0.0087 | 5.660 | 0.142 | 0.0992 | 0.0023 | -2 | 1907 | 4 |

**NOTES:** Analysis labels are in the format nnnnA.p–q, where nnnn is the mount number, A is the sample disc on that mount, p is grain number, and q is the analysis sequence for the grain
*f*204 indicates the fraction of common $^{206}Pb$ in total measured $^{206}Pb$ estimated using measured $^{204}Pb/^{206}Pb$ and the Pb isotopic composition of Broken Hill galena. All Pb isotope data and $^{207}Pb/^{206}Pb$ ages have been corrected for common Pb
Disc. lists apparent discordance, calculated as $100*[1-(^{206}Pb/^{238}U\ age)/(^{207}Pb/^{206}Pb\ age)]$
Uncertainties do not include possible contributions from intermount effects or unidentified matrix effects on Pb/U and Pb/Th
Concurrent Pb/U and Pb/Th data for MAD-1 have 1σ scatter of 2.5% and 2.3%, respectively (n = 11)

**Table 3.2. In situ SHRIMP U–Pb data for monazite in GSWA 164369**

| *Analysis* | *U (ppm)* | *Th (ppm)* | *Th/U* | *f204 (%)* | $^{207}Pb^*/^{206}Pb^*$ | *(±1σ)* | $^{206}Pb^*/^{238}U$ | *(±1σ)* | $^{207}Pb^*/^{235}U$ | *(±1σ)* | $^{208}Pb^*/^{232}Th$ | *(±1σ)* | *Disc. (%)* | $^{07}Pb^*/^{206}Pb^*$ *age (Ma)* | *(±1σ)* |
|---|---|---|---|---|---|---|---|---|---|---|---|---|---|---|---|
| *Main group, in grain sequence* | | | | | | | | | | | | | | | |
| 0672A.1–1 | 1740 | 47143 | 27 | 0.054 | 0.1211 | 0.0006 | 0.3553 | 0.0045 | 5.933 | 0.086 | 0.1034 | 0.0022 | 1 | 1972 | 8 |
| 0672A.1–2 | 2241 | 47941 | 21 | 0.054 | 0.1235 | 0.0005 | 0.3674 | 0.0046 | 6.255 | 0.087 | 0.1055 | 0.0022 | -1 | 2007 | 7 |
| 0672A.1–3 | 4300 | 51074 | 12 | 0.009 | 0.1293 | 0.0004 | 0.3824 | 0.0047 | 6.817 | 0.092 | 0.1100 | 0.0023 | 0 | 2089 | 6 |
| 0672A.1–8 | 3486 | 45054 | 13 | 0.030 | 0.1287 | 0.0004 | 0.3947 | 0.0037 | 7.004 | 0.076 | 0.1102 | 0.0027 | -3 | 2080 | 6 |
| 0672A.1–9 | 4044 | 51439 | 13 | 0.043 | 0.1221 | 0.0003 | 0.3749 | 0.0034 | 6.311 | 0.066 | 0.1092 | 0.0027 | -3 | 1987 | 5 |
| 0672A.1–10 | 883 | 43698 | 49 | 0.017 | 0.1189 | 0.0005 | 0.3527 | 0.0038 | 5.781 | 0.073 | 0.1022 | 0.0025 | 0 | 1939 | 8 |
| 0672A.1–11 | 2169 | 46546 | 21 | 0.029 | 0.1224 | 0.0004 | 0.3678 | 0.0035 | 6.207 | 0.068 | 0.1060 | 0.0026 | -1 | 1991 | 6 |
| 0672A.1–12 | 3387 | 46622 | 14 | 0.018 | 0.1287 | 0.0004 | 0.3926 | 0.0037 | 6.968 | 0.074 | 0.1123 | 0.0027 | -3 | 2081 | 5 |
| 0672A.1–13 | 5349 | 44868 | 8 | 0.032 | 0.1307 | 0.0004 | 0.4028 | 0.0037 | 7.261 | 0.076 | 0.1143 | 0.0028 | -4 | 2108 | 5 |
| 0672D.1–2 | 2040 | 48720 | 24 | 0.143 | 0.1306 | 0.0007 | 0.3768 | 0.0049 | 6.788 | 0.101 | 0.1106 | 0.0023 | 2 | 2107 | 9 |
| 0672D.1–3 | 2233 | 44319 | 20 | 0.101 | 0.1319 | 0.0006 | 0.3790 | 0.0048 | 6.893 | 0.099 | 0.1120 | 0.0024 | 2 | 2123 | 8 |
| 0672D.1–4 | 3528 | 74657 | 21 | 0.048 | 0.1324 | 0.0005 | 0.3857 | 0.0049 | 7.043 | 0.099 | 0.1131 | 0.0024 | 1 | 2130 | 7 |
| 0672D.1–5 | 3924 | 64660 | 16 | 0.093 | 0.1319 | 0.0004 | 0.3999 | 0.0038 | 7.272 | 0.078 | 0.1142 | 0.0028 | -2 | 2123 | 5 |
| 0672D.1–6 | 3190 | 55771 | 17 | 0.087 | 0.1313 | 0.0004 | 0.3994 | 0.0039 | 7.229 | 0.080 | 0.1129 | 0.0028 | -2 | 2115 | 5 |
| 0672D.1–7 | 2808 | 69437 | 25 | 0.104 | 0.1321 | 0.0004 | 0.4069 | 0.0039 | 7.414 | 0.080 | 0.1175 | 0.0029 | -3 | 2127 | 5 |
| 0672D.1–8 | 2189 | 49159 | 22 | 0.111 | 0.1330 | 0.0004 | 0.3958 | 0.0038 | 7.257 | 0.079 | 0.1136 | 0.0028 | -1 | 2138 | 5 |
| 0672D.3–1 | 2480 | 27077 | 11 | 0.012 | 0.1236 | 0.0006 | 0.3562 | 0.0047 | 6.071 | 0.092 | 0.1057 | 0.0022 | 2 | 2009 | 9 |
| 0672D.3–1b | *2308* | *23539* | *10* | 0.007 | 0.1213 | 0.0004 | *0.3471* | *0.0043* | *5.806* | *0.079* | *0.1039* | *0.0022* | *3* | 1976 | 6 |
| 0672G.1–1 | 3364 | 54022 | 16 | 0.014 | 0.1299 | 0.0005 | 0.3856 | 0.0050 | 6.907 | 0.098 | 0.1076 | 0.0023 | 0 | 2097 | 6 |
| 0672G.1–2 | 2567 | 51057 | 20 | 0.037 | 0.1226 | 0.0004 | 0.3646 | 0.0046 | 6.162 | 0.086 | 0.1055 | 0.0022 | 0 | 1994 | 6 |
| 0672G.1–3 | 2867 | 57074 | 20 | 0.029 | 0.1232 | 0.0004 | 0.3649 | 0.0047 | 6.200 | 0.087 | 0.1054 | 0.0022 | 0 | 2003 | 6 |
| 0672G.1–4 | 3324 | 55619 | 17 | 0.022 | 0.1238 | 0.0006 | 0.3724 | 0.0048 | 6.357 | 0.093 | 0.1060 | 0.0022 | -1 | 2012 | 8 |
| 0672G.1–5 | 5939 | 48303 | 8 | 0.045 | 0.1311 | 0.0004 | 0.3891 | 0.0048 | 7.034 | 0.095 | 0.1133 | 0.0024 | 0 | 2113 | 5 |
| 0672G.1–5b | *5622* | *30918* | *5* | 0.052 | 0.1311 | 0.0004 | *0.3774* | *0.0046* | *6.820* | *0.090* | *0.1161* | *0.0024* | *2* | 2112 | 5 |
| 0672G.1–6 | 497 | 57896 | 116 | 0.090 | 0.1204 | 0.0008 | 0.3547 | 0.0052 | 5.889 | 0.100 | 0.1033 | 0.0022 | 0 | 1962 | 12 |
| 0672G.1–7 | 547 | 50611 | 93 | 0.000 | 0.1197 | 0.0006 | 0.3553 | 0.0042 | 5.866 | 0.081 | 0.1022 | 0.0025 | 0 | 1952 | 9 |
| 0672G.1–8 | 617 | 50960 | 83 | 0.075 | 0.1201 | 0.0006 | 0.3527 | 0.0041 | 5.840 | 0.080 | 0.1043 | 0.0025 | 1 | 1958 | 9 |
| 0672G.1–10 | 798 | 45673 | 57 | 0.032 | 0.1209 | 0.0005 | 0.3525 | 0.0039 | 5.875 | 0.074 | 0.1025 | 0.0025 | 1 | 1969 | 8 |
| 0672G.1–11 | 2072 | 47534 | 23 | 0.020 | 0.1234 | 0.0004 | 0.3711 | 0.0036 | 6.314 | 0.070 | 0.1064 | 0.0026 | -1 | 2006 | 6 |
| 0672G.1–12 | 1984 | 41078 | 21 | 0.008 | 0.1226 | 0.0004 | 0.3671 | 0.0036 | 6.206 | 0.069 | 0.1051 | 0.0026 | -1 | 1995 | 6 |
| 0672G.1–13 | 2049 | 53406 | 26 | 0.003 | 0.1198 | 0.0004 | 0.3554 | 0.0034 | 5.873 | 0.065 | 0.1020 | 0.0025 | 0 | 1954 | 6 |
| 0672G.1–14 | 986 | 49055 | 50 | 0.045 | 0.1196 | 0.0005 | 0.3528 | 0.0038 | 5.818 | 0.073 | 0.0976 | 0.0024 | 0 | 1950 | 8 |
| 0672G.1–16 | 1230 | 46959 | 38 | 0.060 | 0.1207 | 0.0005 | 0.3542 | 0.0037 | 5.893 | 0.071 | 0.1020 | 0.0025 | 1 | 1966 | 7 |
| *>5% discordant* | | | | | | | | | | | | | | | |
| 0672D.2–1 | 3696 | 59704 | 16 | 0.097 | 0.1314 | 0.0010 | 0.3627 | 0.0054 | 6.570 | 0.119 | 0.1092 | 0.0024 | 6 | 2116 | 14 |
| 0672G.1–15 | 648 | 45872 | 71 | 0.000 | 0.1183 | 0.0006 | 0.3195 | 0.0039 | 5.213 | 0.072 | 0.0986 | 0.0024 | 7 | 1931 | 8 |
| 0672D.2–1b | 2367 | 47035 | 20 | 0.092 | 0.1303 | 0.0005 | 0.3467 | 0.0044 | 6.229 | 0.088 | 0.1123 | 0.0024 | 9 | 2102 | 7 |
| *Higher common Pb* | | | | | | | | | | | | | | | |
| 0672G.1–9 | 473 | 49785 | 105 | 0.316 | 0.1178 | 0.0008 | 0.3413 | 0.0044 | 5.544 | 0.088 | 0.0895 | 0.0022 | 2 | 1923 | 13 |
| *Unstable ion emission* | | | | | | | | | | | | | | | |
| 0672D.1–1 | 1481 | 61052 | 41 | 0.099 | 0.1217 | 0.0016 | 0.3439 | 0.0071 | 5.770 | 0.151 | 0.0992 | 0.0021 | 4 | 1981 | 24 |

**NOTES:** Concurrent Pb/U data for MAD–1 have 1σ scatter of 1.4% (n = 11) and 1.3% (n = 6) for the two analytical sessions. The respective values for the independent Pb/Th calibration were 2.12% and 2.45%
Analysis label 'b' indicates a repeat analysis on a spot. Element abundance and ratio data are not independently calibrated
Other footnotes as in Table 3.1

**Table 3.3. In situ SHRIMP U–Pb data for monazite in GSWA 168713**

| *Analysis* | *U (ppm)* | *Th (ppm)* | *Th/U* | *f204 (%)* | $^{207}Pb^*/^{206}Pb^*$ | *(±1σ)* | $^{206}Pb^*/^{238}U$ | *(±1σ)* | $^{207}Pb^*/^{235}U$ | *(±1σ)* | $^{208}Pb^*/^{232}Th$ | *(±1σ)* | *Disc. (%)* | $^{07}Pb^*/^{206}Pb^*$ *age (Ma)* | *(±1σ)* |
|---|---|---|---|---|---|---|---|---|---|---|---|---|---|---|---|
| *Main group, in grain sequence* | | | | | | | | | | | | | | | |
| 0672I.1–1 | 9201 | 35384 | 4 | 0.024 | 0.1212 | 0.0003 | 0.3607 | 0.0044 | 6.028 | 0.080 | 0.1047 | 0.0022 | -1 | 1974 | 5 |
| 0672I.1–2 | 11523 | 39251 | 3 | 0.020 | 0.1209 | 0.0003 | 0.3544 | 0.0043 | 5.910 | 0.077 | 0.0995 | 0.0021 | 1 | 1970 | 5 |
| 0672I.1–3 | 11380 | 38295 | 3 | 0.016 | 0.1210 | 0.0003 | 0.3549 | 0.0043 | 5.921 | 0.078 | 0.1021 | 0.0022 | 1 | 1971 | 5 |
| 0672I.1–4 | 11243 | 43235 | 4 | 0.029 | 0.1212 | 0.0004 | 0.3621 | 0.0044 | 6.051 | 0.080 | 0.1016 | 0.0022 | -1 | 1974 | 5 |
| 0672I.1–5 | 11346 | 27147 | 2 | 0.007 | 0.1204 | 0.0003 | 0.3720 | 0.0045 | 6.176 | 0.081 | 0.1039 | 0.0022 | -4 | 1962 | 5 |
| 0672K.1–1 | 4158 | 48047 | 12 | 0.033 | 0.1207 | 0.0005 | 0.3534 | 0.0044 | 5.882 | 0.082 | 0.1006 | 0.0021 | 1 | 1967 | 7 |
| 0672K.1–2 | 2992 | 43121 | 14 | 0.037 | 0.1197 | 0.0004 | 0.3590 | 0.0044 | 5.924 | 0.081 | 0.1059 | 0.0022 | -1 | 1951 | 6 |
| 0672K.2–1 | 3452 | 45156 | 13 | 0.032 | 0.1198 | 0.0004 | 0.3575 | 0.0044 | 5.905 | 0.080 | 0.1033 | 0.0022 | -1 | 1953 | 6 |
| 0672K.2–2 | 2024 | 52687 | 26 | 0.028 | 0.1202 | 0.0005 | 0.3432 | 0.0044 | 5.686 | 0.082 | 0.1035 | 0.0022 | 3 | 1959 | 8 |
| *Extremely high common Pb* | | | | | | | | | | | | | | | |
| 0672F.1–3 | 2649 | 11329 | 4 | 47.513 | 0.0933 | 0.0220 | 0.0649 | 0.0017 | 0.836 | 0.198 | 0.0358 | 0.0012 | 83 | 1495 | 447 |
| 0672F.1–2 | 7330 | 18777 | 3 | 48.364 | 0.0873 | 0.0170 | 0.0619 | 0.0013 | 0.745 | 0.146 | 0.0554 | 0.0017 | 82 | 1366 | 375 |

**NOTES:** Concurrent Pb/U and Pb/Th data for MAD–1 have 1σ scatter of 1.4% and 2.1%, respectively (n = 11)
Other footnotes as in Table 3.1

**Table 3.4. In situ SHRIMP U–Pb data for zircon in GSWA 164369**

| *Analysis* | *U (ppm)* | *Th (ppm)* | *Th/U* | *f204 (%)* | $^{207}Pb*/^{206}Pb*$ | *(±1σ)* | $^{206}Pb*/^{238}U$ | *(±1σ)* | $^{207}Pb*/^{235}U$ | *(±1σ)* | $^{208}Pb*/^{232}Th$ | *(±1σ)* | *Disc. (%)* | $^{07}Pb*/^{206}Pb*$ *age (Ma)* | *(±1σ)* |
|---|---|---|---|---|---|---|---|---|---|---|---|---|---|---|---|
| *Main group, in grain sequence* | | | | | | | | | | | | | | | |
| 0677D.1–1 | 587 | 15 | 0.03 | 0.012 | 0.1236 | 0.0007 | 0.3782 | 0.0056 | 6.446 | 0.103 | 0.0857 | 0.0041 | -3 | 2009 | 10 |
| 0677D.1–2 | 800 | 167 | 0.22 | 0.044 | 0.1266 | 0.0006 | 0.3523 | 0.0051 | 6.149 | 0.093 | 0.0085 | 0.0007 | 5 | 2051 | 8 |
| 0677D.2–1 | 752 | 53 | 0.07 | 0.040 | 0.1264 | 0.0008 | 0.3652 | 0.0053 | 6.366 | 0.102 | 0.0418 | 0.0020 | 2 | 2049 | 12 |
| 0677G.1–1 | 495 | 38 | 0.08 | –0.003 | 0.1207 | 0.0011 | 0.3507 | 0.0054 | 5.836 | 0.105 | 0.0865 | 0.0027 | 1 | 1966 | 17 |
| 0677G.1–2 | 368 | 9 | 0.02 | 0.034 | 0.1216 | 0.0008 | 0.3534 | 0.0062 | 5.926 | 0.112 | 0.0941 | 0.0055 | 1 | 1980 | 12 |
| 0677G.1–3 | 942 | 9 | 0.01 | 0.003 | 0.1323 | 0.0005 | 0.3689 | 0.0052 | 6.727 | 0.099 | 0.1088 | 0.0056 | 5 | 2128 | 7 |
| 0677G.1–4 | 277 | 16 | 0.06 | 0.243 | 0.1182 | 0.0012 | 0.3436 | 0.0058 | 5.601 | 0.110 | 0.0687 | 0.0101 | 1 | 1930 | 18 |
| 0677G.2–1 | 340 | 28 | 0.08 | 0.103 | 0.1199 | 0.0010 | 0.3548 | 0.0060 | 5.867 | 0.111 | 0.0959 | 0.0046 | 0 | 1955 | 15 |
| 0677G.2–2 | 395 | 16 | 0.04 | 0.091 | 0.1206 | 0.0008 | 0.3433 | 0.0054 | 5.710 | 0.098 | 0.0437 | 0.0027 | 3 | 1966 | 12 |
| 0677G.2–3 | 314 | 12 | 0.04 | 0.175 | 0.1185 | 0.0010 | 0.3340 | 0.0055 | 5.457 | 0.101 | 0.0871 | 0.0085 | 4 | 1933 | 15 |
| 0677H.1–1 | 728 | 16 | 0.02 | 0.062 | 0.1245 | 0.0006 | 0.3510 | 0.0051 | 6.025 | 0.092 | 0.0488 | 0.0051 | 4 | 2022 | 9 |
| 0677H.1–2 | 710 | 8 | 0.01 | 0.086 | 0.1266 | 0.0006 | 0.3685 | 0.0053 | 6.430 | 0.098 | 0.0601 | 0.0193 | 1 | 2051 | 9 |
| 0677H.1–3 | 386 | 26 | 0.07 | 0.029 | 0.1202 | 0.0009 | 0.3434 | 0.0055 | 5.692 | 0.101 | 0.0817 | 0.0030 | 3 | 1959 | 14 |
| 0677H.2–1 | 574 | 38 | 0.07 | 0.065 | 0.1199 | 0.0007 | 0.3587 | 0.0054 | 5.927 | 0.096 | 0.0925 | 0.0034 | -1 | 1954 | 10 |
| 0677H.3–1 | 396 | 25 | 0.07 | 0.019 | 0.1197 | 0.0010 | 0.3529 | 0.0069 | 5.823 | 0.124 | 0.1005 | 0.0037 | 0 | 1952 | 15 |
| 0677I.1–2 | 319 | 32 | 0.10 | 0.069 | 0.1155 | 0.0009 | 0.3373 | 0.0056 | 5.372 | 0.099 | 0.0383 | 0.0059 | 1 | 1888 | 14 |
| 0677I.1–3 | 292 | 18 | 0.06 | 0.198 | 0.1156 | 0.0016 | 0.3518 | 0.0060 | 5.606 | 0.122 | 0.0791 | 0.0169 | -3 | 1889 | 25 |
| 0677I.1–4 | 331 | 31 | 0.10 | 0.198 | 0.1137 | 0.0013 | 0.3258 | 0.0054 | 5.106 | 0.103 | 0.0737 | 0.0062 | 2 | 1859 | 20 |
| *Discordant or high common Pb* | | | | | | | | | | | | | | | |
| 0677G.2–4 | 241 | 42 | 0.18 | 0.106 | 0.1203 | 0.0011 | 0.3294 | 0.0056 | 5.4650 | 0.1046 | 0.0177 | 0.0020 | 6 | 1961 | 16 |
| 0677H.2–2 | 386 | 57 | 0.15 | 0.016 | 0.1211 | 0.0009 | 0.3222 | 0.0052 | 5.3789 | 0.0942 | 0.0567 | 0.0018 | 9 | 1972 | 13 |
| 0677D.2–2 | 881 | 276 | 0.32 | 0.011 | 0.1319 | 0.0006 | 0.3424 | 0.0049 | 6.2284 | 0.0920 | 0.0087 | 0.0004 | 11 | 2124 | 7 |
| 0677H.1–4 | 840 | 60 | 0.07 | 0.108 | 0.1282 | 0.0008 | 0.3236 | 0.0046 | 5.7199 | 0.0887 | 0.0400 | 0.0036 | 13 | 2073 | 11 |
| 0677H.3–2 | 369 | 19 | 0.05 | 0.736 | 0.1241 | 0.0018 | 0.2912 | 0.0047 | 4.9822 | 0.1088 | 0.2195 | 0.0227 | 18 | 2016 | 26 |
| 0677I.1–1 | 268 | 27 | 0.10 | 1.059 | 0.1174 | 0.0037 | 0.3298 | 0.0058 | 5.3366 | 0.1947 | 0.0931 | 0.0231 | 4 | 1916 | 57 |

**NOTES:** Concurrent Pb/U data for CZ3 ($n$ = 16 of 19) have 1σ scatter (in excess of precision) of 1.3%
Common Pb composition was estimated from the Stacey–Kramers (1975) model at the approximate age of the sample
Other footnotes as in Table 3.1

**Appendix 4**

# In situ LA-MC-ICPMS zircon Lu–Hf analyses

## Analytical methods

Hafnium isotope analyses were conducted in situ using a New Wave/Merchantek LUV213 laser-ablation microprobe, attached to a Nu Plasma multi-collector inductively coupled plasma mass spectrometer (LA-MC-ICPMS). The analyses employed a beam diameter of ~55 μm and a 5 Hz repetition rate. Typical ablation times were 100–120 seconds, resulting in pits 40–60 μm deep. The ablated sample was transported from the laser-ablation cell, via a mixing chamber, to the ICP-MS torch by a helium carrier gas.

Interference of $^{176}$Lu on $^{176}$Hf is corrected by measuring the intensity of the interference-free $^{175}$Lu isotope, and by using $^{176}$Lu/$^{175}$Lu = 1/40.02669 (DeBievre and Taylor, 1993) to calculate $^{176}$Lu/$^{177}$Hf. Similarly, the interference of $^{176}$Yb on $^{176}$Hf has been corrected by measuring the interference-free $^{172}$Yb isotope, and using $^{176}$Yb/$^{172}$Yb to calculate $^{176}$Yb/$^{177}$Hf. The appropriate value of $^{176}$Yb/$^{172}$Yb was determined by spiking the JMC475 hafnium standard with ytterbium, and finding the value of $^{176}$Yb/$^{172}$Yb (0.58669) required to yield the value of $^{176}$Hf/$^{177}$Hf obtained on the pure hafnium solution. Analyses of standard zircons (Griffin et al., 2000, 2004) illustrate the precision and accuracy obtainable on the $^{176}$Hf/$^{177}$Hf ratio, despite corrections to $^{176}$Hf. The typical 2σ precision of the $^{176}$Hf/$^{177}$Hf ratios is +0.00002, equivalent to +0.7 εHf unit. The accuracy and precision of this method are discussed in more detail by Griffin et al. (2000, 2004), and detailed discussions regarding the overlap corrections for $^{176}$Lu and $^{176}$Yb are provided by Griffin et al. (2006, 2007).

Zircon grains from the Mud Tank carbonatite locality were analysed, together with the samples, as an independent control on reproducibility and instrument stability (one Mud Tank analysis for every 10 unknown analyses). Most of the data and the mean $^{176}$Hf/$^{177}$Hf value (0.282527 ± 0.000028; n = 10) are within 2 standard deviations of the recommended value (0.282522 ± 0.000042 (2σ); Griffin et al., 2007). A single analysis of the 91500 zircon standard analysed during this study indicated $^{176}$Hf/$^{177}$Hf = 0.282304 ± 0.000042 (2σ), which is well within the range of values reported by Griffin et al. (2006).

Calculation of $\varepsilon_{Hf}$ values employed the chondritic values of Scherer et al. (2001). Calculation of model ages ($T_{DM}$) based on a depleted-mantle source used a model with ($^{176}$Hf/$^{177}$Hf)$_i$ = 0.279718 at 4.56 Ga and $^{176}$Lu/$^{177}$Hf = 0.0384; this produces a present-day value of $^{176}$Hf/$^{177}$Hf of 0.28325, similar to that of average mid-ocean ridge basalt (MORB; Griffin et al., 2000, 2004). $T_{DM}$ ages, which are calculated using the measured $^{176}$Lu/$^{177}$Hf of the zircon, can only give a minimum age for the source material of the magma from which the zircon crystallized. Therefore, for each zircon, a 'crustal' model age ($T^C_{DM}$) was calculated, which assumes that its parental magma was produced from a volume of average Precambrian continental crust with a $^{176}$Lu/$^{177}$Hf ratio of 0.015 (Griffin et al., 2002).

## References

DeBievre, P and Taylor, PDP 1993, Table of the isotopic composition of the elements: International Journal of Mass Spectrometry and Ion Processes, v. 123, p. 149.

Griffin, WL, Pearson, NJ, Belousova, EA, Jackson, SE, O'Reilly, SY, van Achterberg, E and Shee, SR 2000, The Hf isotope composition of cratonic mantle: LAM-MC-ICPMS analysis of zircon megacrysts in kimberlites: Geochimica et Cosmochimica Acta, v. 64, p. 133–147.

Griffin, WL, Wang, X, Jackson, SE, Pearson, NJ, O'Reilly, SY, Xu, X and Zhou, X 2002, Zircon chemistry and magma genesis, SE China: in-situ analysis of Hf isotopes, Pingtan and Tonglu igneous complexes: Lithos, v. 61, p. 237–269.

Griffin, WL, Belousova, EA, Shee, SR, Pearson, NJ and O'Reilly, SY 2004, Archean crustal evolution in the northern Yilgarn Craton: U–Pb and Hf-isotope evidence from detrital zircons: Precambrian Research, v. 127, p. 19–41.

Griffin, WL, Pearson, NJ, Belousova, EA and Saeed, A 2006, Comment: Hf-isotope heterogeneity in standard zircon 91500: Chemical Geology, v. 233, p. 358–363.

Griffin, WL, Pearson, NJ, Belousova, EA and Saeed, A 2007, Reply to 'Comment to short-communication 'Comment: Hf-isotope heterogeneity in zircon 91500' by WL Griffin, NJ Pearson, EA Belousova, A Saeed (Chemical Geology 233 (2006) p. 358–363)' by F Corfu: Chemical Geology, v. 244, p. 354–356.

Jackson, SE, Pearson, NJ, Griffin, WL and Belousova, EA 2004, The application of laser ablation-inductively coupled plasma-mass spectrometry to in-situ U–Pb zircon geochronology: Chemical Geology, v. 211, p. 47–69.

Scherer, E, Münker, C and Mezger, K 2001, Calibration of the lutetium-hafnium clock: Science, v. 293, p. 683–687.

**Table 4.1. In situ Lu–Hf data for detrital zircons from samples of Quartpot Pelite**

| *Sample no.* | *Analysis no.* | *$^{207}Pb/^{206}Pb$ date* | *$^{176}Hf/^{177}Hf$ measured* | *(±1σ)* | *$^{176}Lu/^{177}Hf$ measured* | *$^{176}Yb/^{177}Hf$ measured* | *$^{176}Hf/^{177}Hf$ initial* | *epsilon Hf* | *(±1σ)* | *$T_{DM}$ (crustal)* |
|---|---|---|---|---|---|---|---|---|---|---|
| 142910 | 1.1 | 2030 | 0.281372 | 0.000011 | 0.000537 | 0.025152 | 0.281351 | -5.0 | 0.39 | 2.98 |
| | 3.1 | 2030 | 0.281325 | 0.000009 | 0.000981 | 0.057148 | 0.281287 | -7.2 | 0.31 | 3.12 |
| | 7.1 | 2030 | 0.281319 | 0.000009 | 0.000545 | 0.023699 | 0.281298 | -6.9 | 0.30 | 3.10 |
| | 8.1 | 2030 | 0.281351 | 0.000009 | 0.001306 | 0.059355 | 0.281301 | -6.8 | 0.33 | 3.09 |
| | 9.1 | 2080 | 0.281373 | 0.000013 | 0.000130 | 0.007275 | 0.281368 | -3.2 | 0.46 | 2.91 |
| | 11.2 | 2295 | 0.281296 | 0.000013 | 0.000470 | 0.019792 | 0.281275 | -1.6 | 0.46 | 2.97 |
| | 12.1 | 2258 | 0.281146 | 0.000013 | 0.001414 | 0.083878 | 0.281085 | -9.2 | 0.46 | 3.42 |
| | 14.1 | 2080 | 0.281346 | 0.000012 | 0.000362 | 0.017368 | 0.281332 | -4.5 | 0.42 | 2.99 |
| | 16.1 | 2264 | 0.281190 | 0.000015 | 0.000201 | 0.011353 | 0.281181 | -5.6 | 0.53 | 3.20 |
| | 17.1 | 2030 | 0.281320 | 0.000008 | 0.000768 | 0.036920 | 0.281290 | -7.1 | 0.27 | 3.12 |
| | 18.1 | 2080 | 0.281342 | 0.000009 | 0.000956 | 0.047300 | 0.281304 | -5.5 | 0.33 | 3.05 |
| | 21.1 | 2030 | 0.281386 | 0.000006 | 0.000937 | 0.045541 | 0.281350 | -5.0 | 0.21 | 2.98 |
| | 23.1 | 2174 | 0.281287 | 0.000009 | 0.000594 | 0.031362 | 0.281262 | -4.8 | 0.32 | 3.08 |
| | 24.1 | 2030 | 0.281385 | 0.000013 | 0.001806 | 0.083329 | 0.281315 | -6.2 | 0.46 | 3.06 |
| 142905 | 1.1 | 2075 | 0.281327 | 0.000012 | 0.000632 | 0.030552 | 0.281302 | -5.7 | 0.42 | 3.06 |
| | 3.1 | 2075 | 0.281403 | 0.000011 | 0.000746 | 0.038065 | 0.281374 | -3.1 | 0.39 | 2.90 |
| | 4.1 | 2075 | 0.281431 | 0.000017 | 0.000959 | 0.039548 | 0.281393 | -2.4 | 0.60 | 2.85 |
| | 6.1 | 2075 | 0.281253 | 0.000011 | 0.000680 | 0.028165 | 0.281226 | -8.4 | 0.39 | 3.23 |
| | 8.1 | 2000 | 0.281315 | 0.000011 | 0.000838 | 0.043124 | 0.281283 | -8.1 | 0.39 | 3.15 |
| | 9.1 | 2045 | 0.281324 | 0.000010 | 0.001158 | 0.060410 | 0.281279 | -7.2 | 0.35 | 3.13 |
| | 11.1 | 2045 | 0.281357 | 0.000011 | 0.001104 | 0.055425 | 0.281314 | -5.9 | 0.39 | 3.05 |
| | 14.1 | 2113 | 0.281374 | 0.000011 | 0.000435 | 0.020829 | 0.281356 | -2.9 | 0.39 | 2.91 |
| | 16.1 | 2075 | 0.281371 | 0.000008 | 0.000747 | 0.037853 | 0.281342 | -4.3 | 0.28 | 2.97 |
| | 18.1 | 2209 | 0.281175 | 0.000009 | 0.000307 | 0.017985 | 0.281162 | -7.6 | 0.30 | 3.28 |
| | 21.1 | 2075 | 0.281317 | 0.000010 | 0.001030 | 0.057329 | 0.281276 | -6.6 | 0.34 | 3.12 |
| | 23.1 | 2045 | 0.281215 | 0.000011 | 0.000576 | 0.025916 | 0.281193 | -10.3 | 0.39 | 3.33 |
| | 24.1 | 2226 | 0.281202 | 0.000007 | 0.000677 | 0.032869 | 0.281173 | -6.8 | 0.24 | 3.25 |
| | 25.1 | 2000 | 0.281352 | 0.000010 | 0.000275 | 0.013990 | 0.281342 | -6.0 | 0.35 | 3.02 |
| | 26.1 | 2045 | 0.281349 | 0.000015 | 0.001068 | 0.058020 | 0.281307 | -6.2 | 0.53 | 3.07 |
| 168944 | 10.1 | 2025 | 0.281307 | 0.000008 | 0.000791 | 0.037533 | 0.281277 | -7.7 | 0.29 | 3.15 |
| | 13.1 | 2025 | 0.281380 | 0.000009 | 0.001024 | 0.034793 | 0.281341 | -5.5 | 0.32 | 3.01 |
| | 15.1 | 2025 | 0.281302 | 0.000012 | 0.000588 | 0.031704 | 0.281279 | -7.6 | 0.42 | 3.14 |
| | 16.1 | 2025 | 0.281409 | 0.000010 | 0.000700 | 0.029614 | 0.281382 | -4.0 | 0.35 | 2.91 |
| | 18.1 | 2223 | 0.281172 | 0.000007 | 0.000311 | 0.014859 | 0.281159 | -7.4 | 0.26 | 3.28 |
| | 19.1 | 2025 | 0.281385 | 0.000011 | 0.000982 | 0.043839 | 0.281347 | -5.2 | 0.39 | 2.99 |
| | 24.1 | 2025 | 0.281377 | 0.000009 | 0.000502 | 0.021959 | 0.281358 | -4.9 | 0.31 | 2.97 |
| | 25.1 | 2025 | 0.281393 | 0.000011 | 0.000451 | 0.019932 | 0.281376 | -4.2 | 0.39 | 2.93 |
| | 26.1 | 2252 | 0.281251 | 0.000008 | 0.000680 | 0.032214 | 0.281222 | -4.5 | 0.29 | 3.12 |
| | 28.1 | 2025 | 0.281283 | 0.000012 | 0.000986 | 0.047109 | 0.281245 | -8.9 | 0.42 | 3.22 |
| | 29.1 | 2253 | 0.281191 | 0.000011 | 0.001249 | 0.059907 | 0.281137 | -7.5 | 0.39 | 3.31 |
| | 30.1 | 2025 | 0.281379 | 0.000008 | 0.000862 | 0.036000 | 0.281346 | -5.3 | 0.27 | 3.00 |
| | 31.1 | 2025 | 0.281417 | 0.000009 | 0.001062 | 0.047989 | 0.281376 | -4.2 | 0.30 | 2.93 |

This Record is published in digital format (PDF) and is available online at <www.dmp.wa.gov.au/GSWApublications>.
Laser-printed copies can be ordered from the Information Centre for the cost of printing and binding.

Further details of geological products produced by the Geological Survey of Western Australia can be obtained by contacting:

Information Centre
Department of Mines and Petroleum
100 Plain Street
EAST PERTH WESTERN AUSTRALIA 6004
Phone: (08) 9222 3459 Fax: (08) 9222 3444
www.dmp.wa.gov.au/ebookshop